

MIXING AROUND A SHALLOW SEAMOUNT

by

© Todd Douglas Mudge

B.Sc., Memorial University of Newfoundland, 1991

A Thesis Submitted in Partial Fulfillment of the

Requirements for the Degree of

MASTER OF SCIENCE

in the

SCHOOL OF EARTH AND OCEAN SCIENCES

We accept this thesis as conforming

to the required standard

[REDACTED]
Dr. R. Lueck, Co-Supervisor (School of Earth and Ocean Sciences)

[REDACTED]
Dr. C. Garrett, Co-Supervisor (School of Earth and Ocean Sciences)

[REDACTED]
Dr. A. Weaver, Departmental Member (School of Earth and Ocean Sciences)

[REDACTED]
Dr. W. Crawford, Additional Member (Institute of Ocean Sciences)

[REDACTED]
Dr. N. Djilali, External Examiner (Mechanical Engineering)

© TODD DOUGLAS MUDGE, 1994

UNIVERSITY OF VICTORIA

All right reserved. Thesis may not be reproduced in whole or in part, by photocopy or other means, without the permission of the author.

Abstract

Microstructure measurements were taken as part of a multi-disciplinary study of a shallow seamount in the North Pacific. Cobb Seamount, approximately 500 km west of Washington state, rises from the abyssal sea-floor at 3000 m to within 27 m of the surface. The waters around Cobb contain high concentrations of planktonic and fish communities whose presence is believed to be the result of interactions between physical processes and phytoplankton.

The microstructure measurements at Cobb were unique because they were the first to include observations within the bottom boundary layer (bbl) of a seamount. Within the bbl, the diurnal tide and internal waves dominate the mean flow around the seamount. Bottom mixing and bottom mixed layer thickness are intermittent; with periods ranging from a few hours to 24 hours. The effective vertical eddy diffusivity within the bbl of the seamount is $2\text{--}10 \times 10^{-4} \text{ m}^2 \text{ s}^{-1}$. Hence, the mixing within the bbl of Cobb can be as great as the mixing occurring in 1000 km^2 of the open ocean.

Internal tides that are generated and internal waves that are reflected by the bottom produce enhanced and persistent turbulence within 8 km of the flank of Cobb. Most of the turbulence is generated by semi-diurnal internal tidal waves originating from the rim of the seamount. The average vertical diffusivity 3 km from the flank was $> 10^{-3} \text{ m}^2 \text{ s}^{-1}$, more than 2 orders of magnitude larger than what is observed in the open ocean. The mixing that occurs at Cobb is equivalent to the mixing that occurs in $10,000\text{--}100,000 \text{ km}^2$ of the open ocean. If all seamounts are as efficient mixers as Cobb, then they could produce 1–10 times more mixing in the deep Pacific Ocean than occurs within the ocean's interior.

Internal wave driven motions over the seamount obscure the bending of isopycnals

by the geostrophic-mean flow. Previous claims of isopycnal doming over and around Cobb were made without accounting for this effect. Therefore, the existence of doming over Cobb is still an open question.

Microstructure measurements made with airfoil shear probes contain anomalous signals that are mostly caused by particle hits. I have determined that these particles are on the order of 0.3 mm and greater. The particles are primarily biological in origin, but may be either living or dead. It may be possible to use these anomalous signals to determine relative and perhaps absolute particle concentrations.



Dr. R. Lueck, Co-Supervisor (School of Earth and Ocean Sciences)



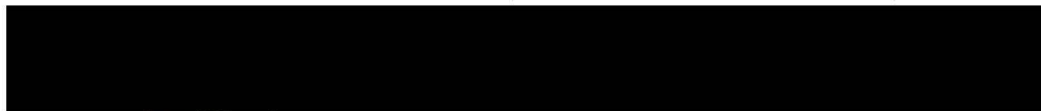
Dr. C. Garrett, Co-Supervisor (School of Earth and Ocean Sciences)



Dr. A. Weaver, Departmental Member (School of Earth and Ocean Sciences)



Dr. W. Crawford, Additional Member (Institute of Ocean Sciences)



Dr. N. Djilali, External Examiner (Mechanical Engineering)

Table of Contents

Abstract	ii
List of Tables	vii
List of Figures	viii
Acknowledgments	xv
1 Introduction	1
2 Background: Theory and Equipment	6
2.1 Mean Flows and Seamounts	6
2.2 Turbulence and Mixing	10
2.3 Measuring Turbulent Dissipation	11
2.4 The Bottom Boundary Layer	13
2.5 Internal Waves	16
2.6 Large Scale Mixing	20
3 Equipment and Data Processing	23
3.1 Measurement Positions	23
3.2 FLY II Profiler	26
3.3 Digital Signal Processing of FLY II Data	28
3.3.1 Pressure and Fall Speed	29
3.3.2 Low Resolution Temperature and Temperature Gradient	30
3.3.3 Conductivity and Salinity	30
3.4 Enhanced Temperature	33

3.5	ϵ as Determined by Microstructure Shear	36
3.5.1	Removal of Anomalous Signals in Microstructure Shear	36
3.5.2	Spectral Estimates of ϵ	39
3.6	Length Scales and Decay Time of Turbulence	43
4	Background Observations	47
4.1	Mean Circulation	47
4.2	Internal Waves	49
4.3	Biological Implications of Cobb Seamount	52
4.4	CTD Results	53
5	Transects	56
5.1	Isopycnal Surfaces	56
5.2	Dissipation Rate Transects	59
5.3	Diffusivity Transects	64
5.4	Mixing Transect	68
5.5	Discussion	69
6	Time Series	74
6.1	Isopycnal Surfaces	74
6.2	Dissipation Rate Time Series	76
6.3	Diffusivity Time Series	79
6.4	Discussion	82
7	Bottom Boundary Layer Observations	84
7.1	Log Layer	86
7.2	Stratification Capped Turbulence	88
7.3	Stratification with Uncapped Turbulence	92
7.4	Capped Dissipation in BML	92

<i>Table of Contents</i>	vi
7.5 Bottom Mixing Efficiency	96
7.6 Bottom Mixed Layer Thickness Models	97
7.7 Discussion	99
8 Counting Spikes	101
8.1 Measurements	101
8.2 Source of Spikes	108
8.3 Discussion	110
9 Thorpe Scales	112
10 Conclusions	117
Bibliography	121

List of Tables

3.1	Characteristics of each successful series.	24
3.2	Signals recorded on the fast and slow channels.	28
4.3	Fluctuation kinetic energies of currents with periods less than 20 hours for the 1992 cruise (Freeland <i>pers. comm.</i>). The values are in $\text{cm}^2 \text{s}^{-2}$.	49
7.4	Number of profiles where FLY II landed on the bottom.	85
7.5	Number of profiles of each BBL type.	90

List of Figures

1.1	Cobb Seamount's position relative to the west coast of North America. (Codiga <i>pers. comm.</i>)	2
1.2	Bathymetry of Cobb Seamount with contours at every 100 m and the shallowest contour at 100 m.	3
3.3	Positions of series 3 profiles. Solid line contours begin at 100 m and continue at 100 m intervals; dashed line contours begin at 150 m and continue at 100 m intervals.	25
3.4	Positions of series 4 profiles. Solid line contours begin at 100 m and continue at 100 m intervals; dashed line contours begin at 150 m and continue at 100 m intervals.	25
3.5	Positions of series 5 (+) and 6 (o) profiles. The contour lines are at every 100 m where the minimum contour is 100 m.	26
3.6	The FLY II free-falling microstructure profiler. This is the same configuration as used during the June 1992 cruise with the exception of the brush, which was replaced with increased flotation (adapted from Dewey 1987).	27
3.7	Profiles of salinity after various levels of temperature correction. The labeled profiles had: (0) no correction, (1) a lag of 24 units, (2) a lag of 24 units and the Butterworth filter, and (3) a lag of 24 units, the Butterworth filter, and thermal inertia correction.	32

3.8	Spectra of 30 s of quiescent data; pre-emphasized digital signal (upper solid curve) and its quantization noise spectrum (upper dashed line); enhanced digital signal (lower solid curve) and its quantization noise spectrum (sloping dashed line).	34
3.9	A 50 m segment of temperature off the seamount from transect 1. This section is turbulent and had a mean vertical gradient of less than $1 \text{ m}^{\circ}\text{C m}^{-1}$. The solid horizontal line indicates the size of a bit prior to pre-emphasis.	35
3.10	Vertically integrated microstructure shear.	37
3.11	Power density spectrum of microstructure shear. From 0–40 Hz the spectrum is dominated by turbulence. From 40–70 Hz the spectrum is dominated by three large spikes that are due to body vibrations. Above 70 Hz the spectrum is dominated by white noise due primarily to quantization. The dissipation rate for the data is $1.4 \times 10^{-7} \text{ W kg}^{-1}$	38
3.12	Thorpe displacement for a region of strong turbulence and no intrusions.	44
3.13	Thorpe scale for the same profile as Fig. 3.12, as determined by a 20 m running average.	45
4.14	Along isobath flow on the flat top of Cobb, 3 m above the bottom. The filled curve is for flow to the SE. The series began June 23, 1992 at 14:59.	50
4.15	Cross isobath flow on the flat top of Cobb, 3 m above the bottom. The filled curve is for flow upslope. The series began June 23, 1992 at 14:59.	51
4.16	A time series of vertical temperature gradient, as determined from the bottom two current meters of M1, that is normalized by the far field temperature gradient. The filled curve is for gradients larger than the norm. The time series is from June 28–29, 1992.	52

4.17	Salinity (dots), temperature (decreasing with depth), and density (increasing with depth) for one profile from the eastern flank of the seamount. All parameters are averaged into 1 m bins.	53
4.18	The far field buoyancy frequency, N , as determined from an average of the last 20 profiles from the first transect and a 20 m running average.	54
4.19	The e-folding time, τ_e , as determined from the N in Fig. 4.18.	54
5.20	Constant σ_T surfaces for the first transect. The ticks on the upper x-axis indicate profile positions. The isopycnals are set 0.1 kg m^{-3} apart, with isopycnals of 25 and 26 kg m^{-3} marked. The bottom depth is indicated by the solid line at the left of the plot.	57
5.21	Constant σ_T surfaces for the second transect. The ticks on the upper x-axis indicates profile positions. The isopycnals are set 0.1 kg m^{-3} apart, with isopycnals of 25 and 26 kg m^{-3} marked.	57
5.22	$\log_{10} \epsilon$ for transect 1. Contours for $\epsilon = 10^{-6}, 10^{-7}$ and $10^{-8} \text{ W kg}^{-1}$ are plotted. ϵ has been averaged into 10 m bins. The solid line that begins at the rim and extends to $\approx 10 \text{ km}$ from the pinnacle is the ray path for a semi-diurnal internal wave derived by Kevin Lamb (<i>pers. comm.</i>), assuming no mean current.	60
5.23	$\log_{10} \epsilon$ for transect 2. Contours for $\epsilon = 10^{-6}, 10^{-7}$ and $10^{-8} \text{ W kg}^{-1}$ are plotted. ϵ has been averaged into 10 m bins.	61
5.24	$\log_{10} K_v$ for transect 1. Contours for $K_v = 10^{-1}, 10^{-2}, 10^{-3}, 10^{-4}$ and $10^{-5} \text{ m}^2 \text{ s}^{-1}$ are plotted. K_v has been averaged into 10 m bins.	65
5.25	$\log_{10} K_v$ for transect 2. Contours for $K_v = 10^{-2}, 10^{-3}, 10^{-4}$ and $10^{-5} \text{ m}^2 \text{ s}^{-1}$ are plotted. K_v has been averaged into 10 m bins.	66
5.26	Depth averaged K_v for transect 1.	67

- 5.27 Area of open ocean equivalent to the observed mixing in transect 1. The solid line includes all profiles in its mass flux summation, while the dotted line has had the profile with the largest density flux removed when determining the mass flux. 70
- 5.28 The northeast Pacific of the region surrounding Cobb Seamount. Contours are at 500 m intervals beginning at 500 m and ending at 4000 m. Cobb Seamount is centered in the two boxes plotted. The boxes have an area of 10,000 and 100,000 km². 71
- 6.29 Constant σ_T surfaces for the 19 hour time series. The ticks on the upper x-axis indicate profile times. The isopycnals are set 0.1 kg m⁻³ apart, with isopycnals of 25 and 26 kg m⁻³ marked. 75
- 6.30 Constant σ_T surfaces for the CTD time series. The ticks on the upper x-axis indicates profile times. The isopycnals are set 0.1 kg m⁻³ apart, with isopycnals of 25 and 26 kg m⁻³ marked. The solid line at the bottom gives the depth of the water column. 75
- 6.31 $\log_{10} \epsilon$ for the 19 hour time series. Contours for $\epsilon = 10^{-6}, 10^{-7}$ and 10^{-8} W kg⁻¹ are plotted. ϵ has been averaged into 10 m bins. 77
- 6.32 $\log_{10} \epsilon$ for the CTD time series. Contours for $\epsilon = 10^{-6}, 10^{-7}$ and 10^{-8} W kg⁻¹ are plotted. ϵ has been averaged into 10 m bins. 80
- 6.33 $\log_{10} K_v$ for the 19 hour time series. Contours for $K_v = 10^{-2}, 10^{-3}, 10^{-4}$ and 10^{-5} m² s⁻¹ are plotted. K_v has been averaged into 10 m bins. 81
- 6.34 $\log_{10} K_v$ for the CTD time series. Contours for $K_v = 10^{-3}, 10^{-4}$ and 10^{-5} m² s⁻¹ are plotted. K_v has been averaged into 10 m bins. 83

7.35	The shallowest bottom boundary layer profiled during the first transect. The diagrams from bottom to top are of high resolution temperature, microstructure shear, high resolution dissipation rate (solid line) with the theoretical dissipation for log layer (dashed and dotted line) and friction velocity. The thickness of the bml (*) and the turbulent bbl (o) are given, along with the water depth at the top of the diagrams.	87
7.36	The unsmoothed version of high resolution dissipation from figure 7.35. Only the bottom 20 m has been plotted. The dotted diagonal lines all reduce as $1/z$.	88
7.37	A bottom boundary layer over the flat top from the second transect. The diagrams from bottom to top are of high resolution temperature, microstructure shear, high resolution dissipation rate and friction velocity. The thickness of the bml (*) and the turbulent bbl (o) are given, along with the water depth at the top of the diagrams.	89
7.38	The unsmoothed version of high resolution dissipation from figure 7.37. Only the bottom 20 m has been plotted. The dotted diagonal lines all reduce as $1/z$.	90
7.39	Thorpe displacement of the temperature profile in figure 7.37.	91
7.40	The deepest bottom boundary layer profiled during the second transect. The diagrams from bottom to top are of high resolution temperature, microstructure shear, high resolution dissipation rate and friction velocity. The thickness of the bml (*) and the turbulent bbl (o) are given, along with the water depth at the top of the diagrams.	93
7.41	The unsmoothed version of high resolution dissipation from figure 7.40. Only the bottom 20 m has been plotted. The dotted diagonal lines all reduce as $1/z$.	94
7.42	Thorpe displacement of the temperature profile in figure 7.40.	94

- 7.43 The bottom boundary layer from a shallower profile of the second transect. The diagrams from bottom to top are of high resolution temperature, microstructure shear, high resolution dissipation rate and friction velocity. The thickness of the bml (*) and the turbulent bbl (o) are given, along with the water depth at the top of the diagrams. 95
- 7.44 The unsmoothed version of high resolution dissipation from figure 7.41. Only the bottom 20 m has been plotted. The dotted diagonal lines all reduce as $1/z$ 96
- 7.45 Modeled versus measured bottom mixed layer thicknesses. The model thickness is $h_{tl} = 2^{1/4}u_*/(fN)^{1/2}$. The points are plotted by series; + for the 19 hour time series, o for the CTD time series, * for transect 1, and \times for transect 2. 98
- 8.46 A section of shear signal from a single profile in the 19 hour time series. The upper curve is the original shear signal before the spikes are removed. The bottom curve is a plot of the signal after despiking, intentionally staggered down 100 counts. 102
- 8.47 Ensemble averages of spikes for each series. The solid lines are the averages while the dashed lines are the averages plus 2 sample standard deviations. The dashed-dotted lines are 95% confidence limits assuming the spikes follow a Poisson distribution. 103
- 8.48 Suspended particulate matter (right curve) and the ensemble average of number of spikes (left curve) for the CTD time series. 104
- 8.49 Spike profiles for the first transect. Contours from 5 to 20 spikes, at intervals of 5 spikes have been plotted. 105
- 8.50 Spike profiles for the second transect. Contours from 5 to 25 spikes, at intervals of 5 spikes have been plotted. 106

8.51 Spike profiles for the 19 hour time series. Contours from 5 to 30 spikes, at intervals of 5 spikes have been plotted. 107

9.52 A profile near the rim of the seamount during the first transect. The top-left diagram is a profile of the Thorpe displacement. The top-right diagram contains profiles of the Ozmidov scale (solid line) and Thorpe scale (dashed line). The bottom diagram is the Thorpe scale against the Ozmidov scale. There are two diagonal lines, the solid line is for $l_0 = 0.8l_T$ and the dotted line is for $l_0 = 0.89l_T$ 114

9.53 A profile in the far-field during the first transect. The top-left diagram is a profile of the Thorpe displacement. The top-right diagram contains profiles of the Ozmidov scale (solid line) and Thorpe scale (dashed line). The bottom diagram is the Thorpe scale against the Ozmidov scale. There are two diagonal lines, the solid line is for $l_0 = 0.8l_T$ and the dotted line is for $l_0 = 0.19l_T$ 116

Acknowledgments

The research for this thesis has been the result of assistance and guidance I have received from many people. I wish to thank my supervisory committee, Rolf Lueck, Chris Garrett, Andrew Weaver and Bill Crawford for their knowledge and skillful direction. I especially thank Rolf and Chris for their financial aid and encouragement.

This research would have been completely impossible without the gracious loan of Bill's FLY II microstructure instrument. This loan proved very generous indeed; during two of the first four profiles the retrieval line of FLY II became entangled with the bottom. The first time it took over 1/2 hour to free the instrument and the second time it took over 2 hours. Without the quick and professional action of the officers and crew of the *CSS Tully* the instrument would have been lost permanently.

A number of researchers have kindly shared their data with me. Dan Codiga and Charlie Eriksen have an ftp site with bathymetry of Cobb Seamount. John Dower and Howard Freeland provided the CTD data and current meter data sets from the 1992 cruise. Howard also produced one of the plots in this thesis. Kevin Lamb modeled the ray of internal tides for the conditions at Cobb.

For creating the data logging software I thank Anne Gargett, George Chase and Chris MacKay. I also wish to thank Hide Yamazaki and Jim Bishop for many helpful discussions about particulate matter. For those friends and family who have put up with me and helped me along the road to finishing this thesis, thanks.

Chapter 1

Introduction

Seamounts are regions of significant biological and physical interactions. Topographical features, especially shallow seamounts, are sources of high biomass and primary productivity due to interactions between physical processes and planktonic communities. The interaction of seamounts and mean currents generates gyres over or around the seamount. These gyres, if geostrophically balanced, will lift or depress isopycnals. Frictional forces near the bottom produce Ekman flows that can push water up or down slope. Frictional forces also produce shear of the mean flow from which turbulence results. Tidal forcing occurs over topography, generating trapped and internal waves, turbulence and a myriad of complex flows. Internal waves that are generated and reflected affect the structure of the bottom boundary layer by thinning and thickening the bottom mixed layer. Internal waves are transmitted into the ocean interior and break, generating turbulence and mixing near seamounts. There is a complex interplay of mean and tidal flows with internal waves around seamounts.

In this thesis I have tried to answer some questions about the interplay of these physical processes and to take special notice of how they affect mixing near a seamount. Data were collected as part of a multi-disciplinary study of Cobb Seamount, which is situated about 500 km west of the Washington state coast at $46^{\circ} 45' N$ and $130^{\circ} 50' W$ (Fig. 1.1). It is a shallow seamount which rises from the abyssal sea floor at about 3000 m to a minimum depth of 27 m (Fig. 1.2). It is flat topped and has a rim between 200 and 300 m.

The Lueck group, of which I was apart, joined the study at Cobb in July 1992, after one cruise to Cobb on each of the two previous summers. This joint three year

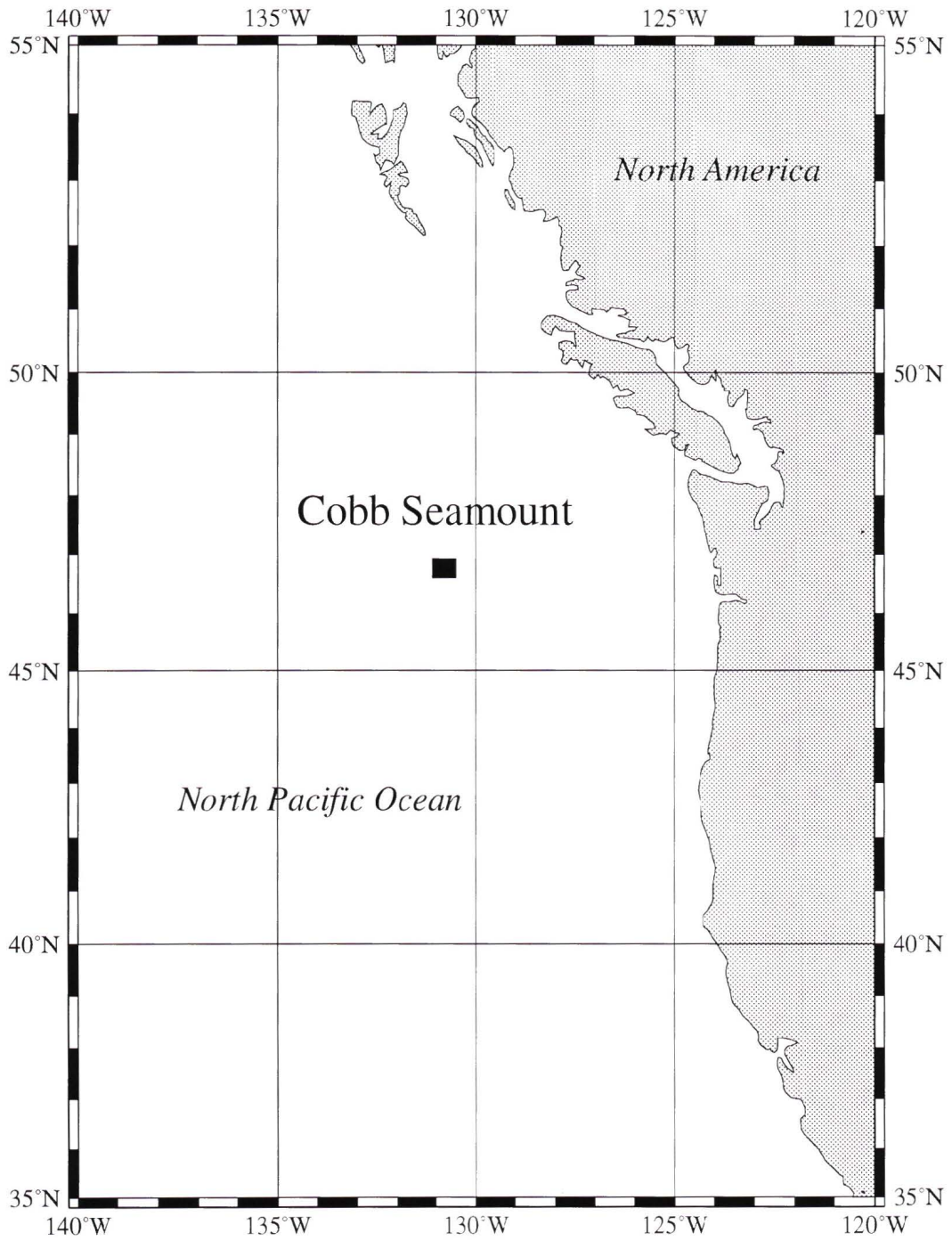


Figure 1.1: Cobb Seamount's position relative to the west coast of North America. (Codiga *pers. comm.*)

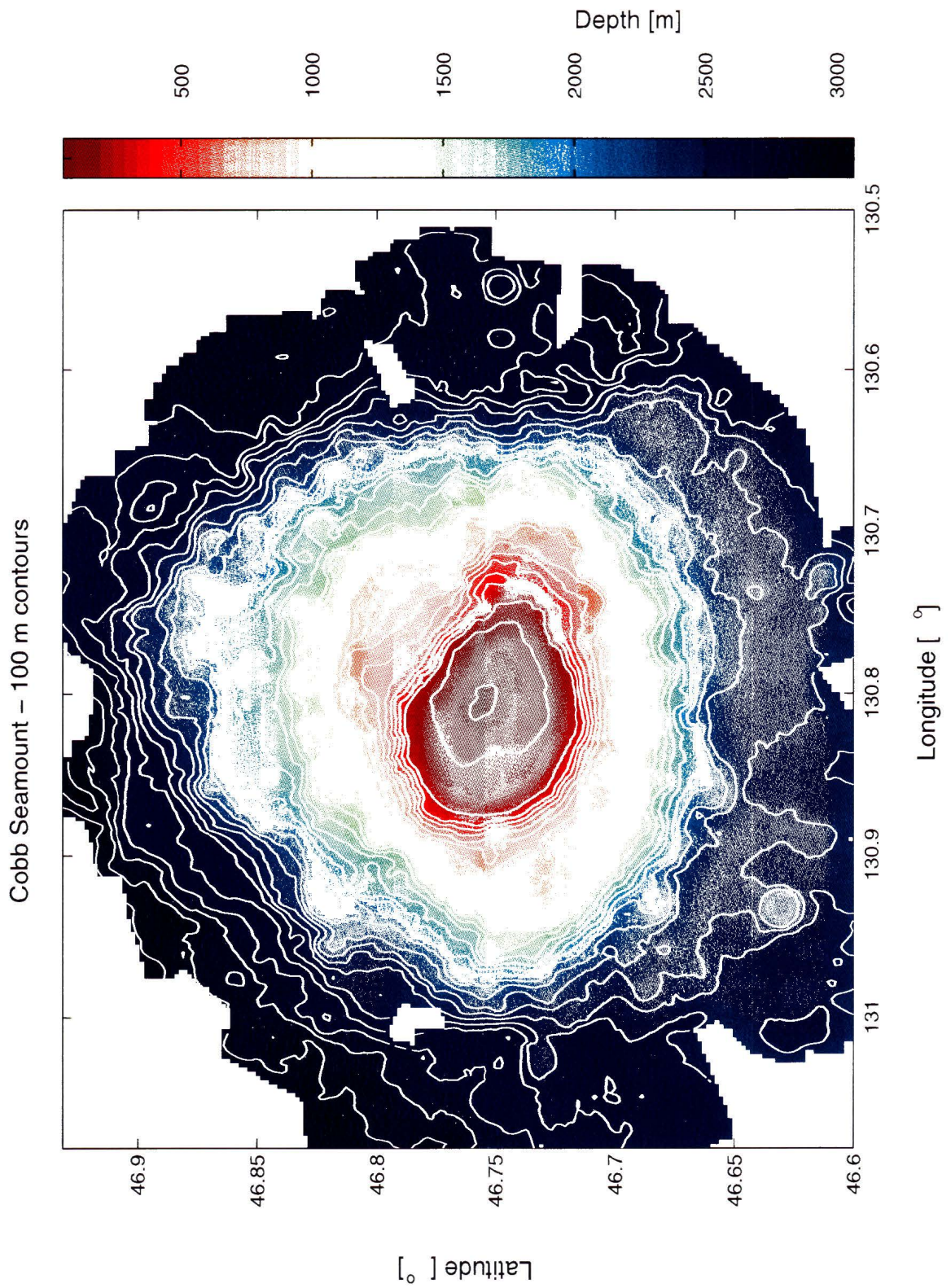


Figure 1.2: Bathymetry of Cobb Seamount with contours at every 100 m and the shallowest contour at 100 m.

study has been dubbed the Cobb Seamount Experiment or CSEX. The experiment set out to study both physical and biological characteristics at Cobb. There were observations of phytoplankton, fish larvae and other biological characteristics (Dower *et al.* 1992; Dower 1994). Surveys with CTDs (Conductivity, Temperature, Depth instruments), moored and ship mounted ADCPs (Acoustic Doppler Current Profiler), moored current meters (Freeland 1994), and a free fall microstructure profiler were completed. Our work included the moored ADCP and the free falling microstructure profiler FLY II (Fig. 3.6). The ADCP provided little useful information, but FLY II showed some surprising and dramatic boundary layer structure and near bottom mixing. For the cruise, FLY II was equipped with a guard that protected the sensors and allowed the instrument to land on the bottom. This allowed the nose mounted sensors to profile the entire water column to within 15 cm of the bottom. Above 10 m depth, the data may be biased by surface waves and the ship's wake.

The next three chapters give an overview of theory, equipment and background results at Cobb. In chapter 2, I present some pertinent theory and discuss the physical interaction of a mean flow with the abrupt topography of a seamount. Some important ideas of turbulence and turbulent mixing also are discussed along with the development of equipment for measuring turbulence. Bottom boundary flows and structure are investigated; internal wave dynamics and turbulent mixing, especially reflection and generation effects, are discussed; and the effect of mixing at the seamount on the large scale mixing of the entire ocean is delved into as well. Chapter 3 is a discussion of FLY II and data processing techniques. Standard CTD processing techniques are presented, as well as a rarely used technique of signal enhancement. A comprehensive approach to estimating dissipation rate is also presented. Chapter 4 has a brief discussion of background observations at seamounts, particularly at Cobb. Of great interest are the measurements of mean currents and internal waves at Cobb.

Chapters 5–8 present the measurements carried out by FLY II during the 1992

cruise. Transects of the seamount by the microstructure instrument are presented in chapter 5. The effect of mean flows versus that of internal waves on isopycnal positions is investigated. The region and source of enhanced turbulence and mixing around Cobb is shown. Most significantly, I estimate the amount of mixing occurring at seamounts and find that they may produce a significant portion of the mixing occurring in the deep Pacific. Two time series with the microstructure instrument are presented in chapter 6. The time dependence of turbulence and mixing is studied to determine if turbulent processes around Cobb are periodic. The series also provide some information to the spatial characteristic of enhanced turbulence at Cobb. In chapter 7, I present some results from the profiles within the bottom boundary layer of the seamount. A method of determining relative plankton concentrations with a microstructure instrument is presented in chapter 8.

A brief discussion of Thorpe and Ozmidov scaling is completed in chapter 9. The last chapter is a brief conclusion of the important physical characteristics of Cobb. Previous claims of isopycnal doming over Cobb are put in doubt. Bottom boundary layer characteristics are found to be highly periodic, with significant changes over the period range of an hour to a day. Near bottom mixing, probably generated by internal waves, is the dominant mixing around Cobb. It exists over a large enough area where it is so greatly enhanced over open-ocean mixing that it may contribute significantly to mixing of the ocean on a much larger scale.

Chapter 2

Background: Theory and Equipment

2.1 Mean Flows and Seamounts

Observations over seamounts have shown the presence of an anti-cyclonic flow field. Some show only a deflection of the mean flow (Roden 1984; Roden and Taft 1985). Others indicate the presence of anti-cyclonic Taylor caps with closed streamlines (Owens and Hogg 1980; Davies *et al.* 1990; Freeland 1994) over topography. These gyres are not in the form of a column that goes from the bottom to the surface; rather, due to stratification, the horizontal scale of the gyres decrease with height above the bottom, forming what is called a Taylor cone or cap.

To gain some insight into the flow field around Cobb I first take the case of no stratification, and an inviscid, incompressible fluid. I have used an f -plane approximation, which is reasonable for Cobb Seamount given that it is only 30 km wide at its base. The flow around the seamount is taken to be geostrophically balanced. This is a plausible assumption where the nonlinear terms in the momentum equations are small relative to the Coriolis term or, equivalently, the Rossby number

$$Ro = \frac{U}{fD} \ll 1, \quad (2.1)$$

where U is the horizontal velocity scale, f is the planetary vorticity and D is the horizontal length scale. For Cobb the mean current $U \approx 10 \text{ cm s}^{-1}$. Its pinnacle is at latitude 46.75° N ; hence the planetary vorticity $f = 1.06 \times 10^{-4} \text{ s}^{-1}$. The radius of Cobb varies from 5 km at the flat top to 15 km at the base. The Rossby number is, therefore, in the range of 0.06–0.19, which meets the condition of (2.1).

The horizontal momentum equations become a simple balance between the Coriolis force and the pressure gradient

$$-fv = -\frac{1}{\rho_0} \frac{\partial p}{\partial x}, \quad (2.2)$$

$$fu = -\frac{1}{\rho_0} \frac{\partial p}{\partial y}, \quad (2.3)$$

where ρ_0 is the water density, p is the pressure, and u and v are horizontal velocities in the x and y directions. If we also take a hydrostatic balance in the vertical

$$0 = \frac{1}{\rho_0} \frac{\partial p}{\partial z} + g, \quad (2.4)$$

where g is the acceleration due to gravity. Eliminating p by cross differentiation in the horizontal momentum equations gives

$$f \left(\frac{\partial v}{\partial y} + \frac{\partial u}{\partial x} \right) = 0. \quad (2.5)$$

Using the continuity equation, $\nabla \cdot \mathbf{u} = 0$, (2.5) leads to

$$\frac{\partial w}{\partial z} = 0. \quad (2.6)$$

Differentiating the horizontal momentum equations with respect to z gives

$$\frac{\partial v}{\partial z} = \frac{\partial u}{\partial z} = 0. \quad (2.7)$$

Hence, we have the Taylor-Proudman theorem

$$\frac{\partial \mathbf{u}}{\partial z} = 0; \quad (2.8)$$

the flow does not vary in the vertical. All horizontal flows, where the Rossby number is small compared to 1, follow isobaths. If a horizontal flow encounters abrupt topography, then the flow is incapable of flowing over the topography, and would instead have to flow around it; thus, a Taylor column forms over the top of the topography.

For seamounts in the Northern Hemisphere, this column will have an anti-cyclonic flow as suggested by conservation of potential vorticity

$$\frac{D}{Dt} \left(\frac{\zeta + f}{h} \right) = 0, \quad (2.9)$$

where the relative vorticity

$$\zeta \equiv \frac{\partial v}{\partial x} - \frac{\partial u}{\partial y}, \quad (2.10)$$

and h is the depth of the water. Take a column of water during spin up of a mean flow (a condition where Taylor-Proudman theorem does not hold) that has no relative vorticity. When it flows over an obstacle its height is reduced and acquires relative vorticity, and in the Northern Hemisphere this forms an anti-cyclonic gyre over the topography.

The oceans are much more complex than this simple model. To study the effects of stratification and viscous forces on the flow over topography a number of laboratory experiments (Davies 1972; Boyer *et al.* 1987; Boyer and Zhang 1990; Zhang and Boyer 1993) and numerical models (Chapman and Haidvogel 1992) have been developed. The complexity of flows over seamounts becomes clear when trying to apply the results of these experiments and models to the conditions at Cobb. I begin with the approach set out by Freeland (1994) who used the results of Chapman and Haidvogel (1992). Three critical parameters were determined to define whether a Taylor cap formed: the Rossby number Ro , the fractional height of the seamount $\delta = h/H$, where h and H are the heights of the seamount and water column off the seamount, and the Burger number $S = NH/fD$, where N is the buoyancy frequency. For a tall seamount with $\delta = 0.9$, which is similar to Cobb, they determined that Taylor caps could occur for $S = 1$ and $Ro < 0.15$. Freeland (1994) discusses the parameter space within which the flow around Cobb lies. He argues that, because of changes in the mean flow in the vertical, the Rossby number may lie in the range of 0.12–0.24, the fractional height is between 0.7 and 1, while the Burger number lies between 7 and 34. Chapman and Haidvogel's (1992) highest value of $S = 1$ is much smaller than seen at Cobb. Freeland argues that the change in critical Rossby number at which closed circulation first occurs is small for Chapman and Haidvogel's (1992) models where S goes from 0 to 1. He concludes that if the mean flow occurs only above

300 m, and we consider the area of the pinnacle as negligible, then the flow around Cobb lies within the region of parameter space in which a Taylor cap will exist. He also concludes that the vertical height (which scales as fD/N) of the cap above the flat top is only 40 m. While these results explain observations, that are given later, of closed circulation over the seamount, the model that Freeland used ignores periodic flows. I believe the tidal components of the flow may play as significant a role as the mean flow component in determining the flow field around Cobb.

The laboratory work of Boyer and Zhang (1990) and Zhang and Boyer (1993) shows a more complex picture of the flow field around topography. They chose to work in an area of parameter space appropriate for Fieberling Guyot ($32^{\circ} 28' \text{ N}$, $127^{\circ} 47' \text{ W}$), as part of a large theoretical and observational study of Fieberling. Perhaps the most significant parameters they included were the result of adding viscous terms and a sinusoidal current component that was superimposed on a mean flow. Given that the parameters of Cobb and Fieberling are significantly different, and the complexity of parameter space discussed by Freeland (1994), the laboratory results cannot be directly applied to Cobb, but they do suggest a number of flow regimes that may be observed at Cobb.

First from Boyer and Zhang (1990), where the mean current was taken to be non-zero, at low Rossby number, $Ro = 0.01$, there is a Taylor cap over the top of the seamount. With mid-values of the Rossby number, $Ro = 0.07$, standing vortices form on the lee side of the seamount. For high values of the Rossby number, $Ro = 0.18$, vortex shedding occurs on the lee side of the seamount and results in the formation of a vortex street. Second, Zhang and Boyer (1993) changed the flow field to contain no mean current and found 6 flow regimes. A common characteristic of all these regimes was the presence of a rectified, anti-cyclonic, topographically trapped current. These results suggest that the flow field around Cobb may be very complex, with significant variations over the time scales of days and weeks as mean and tidal flows change.

2.2 Turbulence and Mixing

There are various places where a discussion of oceanic three dimensional turbulence theory could begin, but I will start with the turbulent kinetic energy (TKE) equation (Kundu 1990)

$$\frac{D}{Dt} \left(\frac{1}{2} \overline{u_i^2} \right) = - \frac{\partial}{\partial x_j} \left(\frac{1}{\rho_0} \overline{p u_j} + \frac{1}{2} \overline{u_i^2 u_j} - 2\nu \overline{u_i e_{ij}} \right) - \overline{u_i u_j} \frac{\partial U_i}{\partial x_j} - \frac{g}{\rho_0} \overline{\rho' w} - 2\nu \overline{e_{ij}^2}, \quad (2.11)$$

where the fluctuating strain rate is

$$e_{ij} = \frac{1}{2} \left(\frac{\partial u_i}{\partial x_j} + \frac{\partial u_j}{\partial x_i} \right), \quad (2.12)$$

the velocity is $U_i + u_i$, $\bar{U}_i = U_i$, $\bar{u}_i = 0$, the density is $\rho_0 + \rho'$, $\bar{\rho}_0 = \rho_0$, $\bar{\rho}' = 0$, ν is the kinematic viscosity, and the overbar implies a spatial average that is longer than the turbulent scales yet shorter than the energy containing scales. The first three terms on the right hand side of (2.11) are of the form of a flux divergence; hence they represent a transport of turbulent kinetic energy. The fourth term, the shear production P , represents the rate of generation of turbulent kinetic energy by an equivalent loss of mean kinetic energy. The fifth term, referred to as the buoyancy production B , can be either positive or negative; hence can either be a source or sink for turbulent kinetic energy. The last term is the viscous dissipation denoted

$$\epsilon = 2\nu \overline{e_{ij}^2}, \quad (2.13)$$

which is a sink for turbulent kinetic energy.

With observations of oceanic turbulence the assumption is made that the local rate of change and the transport terms of (2.11) are small. This leads to a simple balance of production, dissipation and buoyancy flux

$$- \overline{u_i u_j} \frac{\partial U_i}{\partial x_j} = \frac{g}{\rho_0} \overline{\rho' w} + \epsilon. \quad (2.14)$$

The ratio of the buoyancy flux B to production P is known as the flux Richardson number $R_f = B/P$; hence (2.14) becomes

$$P = R_f P + \epsilon \quad (2.15)$$

and

$$B = \frac{g}{\rho_o} \overline{\rho'w} = \frac{R_f}{1 - R_f} \epsilon = \Gamma \epsilon, \quad (2.16)$$

where Γ is known as the mixing efficiency. Direct measurements of P and B are technically difficult but they can be derived from the relatively easily measured ϵ when Γ is known. By taking the Osborn (1980) model, representing the flux as an eddy diffusion,

$$-\overline{\rho'w} = K_\rho \frac{\partial \rho_o}{\partial z}, \quad (2.17)$$

where K_ρ is the the vertical eddy diffusivity. Using (2.16) and (2.17) gives the eddy diffusivity in terms of the dissipation rate

$$K_\rho = \frac{\Gamma \epsilon}{N^2}, \quad (2.18)$$

where the approximation $N^2 \approx -\frac{g}{\rho_o} \frac{\partial \rho_o}{\partial z}$ is assumed. With the knowledge of dissipation rates, buoyancy frequency and the mixing efficiency vertical diffusivities can be estimated

2.3 Measuring Turbulent Dissipation

Oceanic turbulence measurement has seen the development of both sensors and instruments. The pioneering work for measuring oceanic turbulence was completed by Grant *et al.* (1962) using a pair of platinum film probes. One probe was sensitive to temperature and the other, functioning as a hot film anemometer, was sensitive to velocity. The sensors were mounted on the nose of a body that was towed in a tidal channel. The signals proved prone to problems from high frequency vibration and phytoplankton passing close to or becoming attached to the velocity probe (Nasmyth 1970). The greatest drawback of the velocity sensor was its sensitivity to both velocity and temperature variations, which made it inappropriate for many open ocean conditions where there were small velocity fluctuations and large temperature fluctuations; the permanent thermocline is an example.

Grant *et al.* (1968) also mounted the sensors on a submarine in the open Pacific Ocean. They found sharp interfaces between turbulent and quiescent patches. This intermittency, plus motions from internal waves, created a complex combination of horizontal and vertical variability. This inspired the development of vertical profiling instruments that originally focused on the temperature fluctuations (Osborn and Cox 1972) as determined by fast response thermistors. Here the velocity was not measured, instead the variance of the temperature gradient was used to determine a vertical eddy diffusivity for heat. The method assumed steady and lateral homogeneous conditions and no divergence of heat flux variance across boundaries. Similar techniques for small-scale salinity and density measurements were developed by Gregg *et al.* (1973).

Direct velocity measurements were finally available with the development of the airfoil shear probe (Osborn 1974), which was initially used on vertical profilers. The probe tip is an axisymmetric body of revolution aligned with the axis of the free falling profiler. Fluctuating horizontal velocities produce fluctuating angles of attack of the total velocity vector, causing fluctuating lift force on the probe tip. These forces are transferred through the silicon rubber tip to two piezoceramic Bimorph beams that are embedded in the tip. The beams produce voltage potentials when bent. A number of vertical profilers are developed around this probe (Oakey and Elliott 1982; Gregg and Sanford 1988). Some of the profilers have been capable of sampling very near the bottom. Examples are the expendable instrument developed by Lueck (Price *et al.* 1993) and non-expendable instruments such as FLY (Fast Light Yo-yo) II (Dewey *et al.* 1987). The FLY II collected all the microstructure data that will be presented in this thesis.

Other instruments that have been developed around the airfoil shear probe have returned to the initial experiments of horizontal profiling. This includes towed bodies that have been developed (Osborn and Lueck 1985a) and are continuing to be developed by Lueck (*pers. comm.*). Turbulence packages with the airfoil shear probe

have also been mounted on a submarine (Osborn and Lueck 1985b). Perhaps the most challenging of vehicles making *horizontal* measurements is a moored instrument developed by Lueck (*pers. comm.*). For this instrument, turbulent patches are advected past the shear probes by the mean current. This instrument has forced another development in airfoil shear probes. The original probe tips developed by Osborn (1974) were made with silicon rubber. The rubber was sufficient in keeping water from the ceramic beam during the profile time of the free falling instrument (≈ 1 hour). Various coatings of the beams have improved their life time. The best result achieved by Lueck was over 25 days by coating the beam with a thin layer of tin-lead solder. Another approach to reducing probe degradation is the development of a strain gauge sensor to replace the ceramic beam. The strain gauges are mounted on an aluminum beam and surrounded by silicon rubber. The strain gauges are not as prone to degradation by water but are still being studied for their temperature response.

A very different approach to measuring turbulence has been developed by Gargett (1988). The technique uses the vertical velocity field as measured by an ADCP. By using a length scale approach to isotropic, three dimensional turbulence, Gargett (1988) relates the vertical velocity field and its gradient to ϵ . The technique is best used where the vertical scales and velocities of turbulent eddies are large, such as in coastal regions.

2.4 The Bottom Boundary Layer

The definition of the bottom boundary layer (bbl) is in most cases arbitrary. The bottom boundary layer can be considered a region where either the flow field or stratification are directly affected by the bottom. Even this vague definition is perhaps too specific to encompass all of the oceanic conditions and processes that are affected by the bottom. Within this thesis, I will consider the bbl as a region that is 0–20 m

thick, where there is a bottom mixed layer and/or where turbulence is created by viscous forces near the bottom.

The no-slip boundary condition implies that strong shear can occur near the bottom, which can induce turbulence and mixing. Wall bounded shear flows of an otherwise homogeneous mean current in an unstratified fluid with no Coriolis forcing and no time dependence are well known and can be derived by simple dimensional analysis. I will follow the development of this dimensional analysis as set out by Kundu (1990). Near a smooth wall, the mean velocity U should be dependent only on density ρ , the shear stress on the wall τ_0 , the viscosity ν and the distance from the wall z . A commonly defined parameter

$$u_* = \sqrt{\frac{\tau_0}{\rho}}, \quad (2.19)$$

is the friction velocity. Hence, the mean velocity $U = U(u_*, \nu, z)$ and can be expressed in a non-dimensional form

$$\frac{U}{u_*} = F\left(\frac{zu_*}{\nu}\right) = F(z_+), \quad (2.20)$$

which is known as the law of the wall.

Near the wall, the Reynolds stresses are small, therefore, the flow is dominated by viscous effects and this region is called the viscous sublayer. Within the sublayer the stress can be considered constant and equal to the wall stress

$$\nu \frac{\partial U}{\partial z} = \tau_0, \quad (2.21)$$

so that

$$U = \frac{z\tau_0}{\nu} = z_+. \quad (2.22)$$

This viscous sublayer is very thin, < 1 cm for Chriss and Caldwell (1982); however, FLY II can profile only to within 15 cm of the bottom. I can, therefore, ignore the viscous sublayer for the measurements taken at Cobb.

In the region outside the viscous sublayer there is a transition region or buffer layer. Outside the buffer layer is the region known as the internal sublayer or logarithmic layer, where turbulence stresses are dominant. It can be determined simply by dimensional analysis which gives

$$\frac{dU}{dz} = \frac{u_*}{\kappa z}, \quad (2.23)$$

where the von Karman constant $\kappa \approx 0.4$. Integration gives

$$U = \frac{u_*}{\kappa} \ln z + \text{constant}. \quad (2.24)$$

There may be no viscous sublayer if the bottom is rough, but the flow field above the rough elements of the bottom should contain an internal sublayer. If the roughness elements have a height z_0 , then above these elements the flow will be logarithmic and of the form

$$\frac{U}{u_*} = \frac{1}{\kappa} \ln \frac{z}{z_0}. \quad (2.25)$$

The bbl may also be approached in terms of turbulence rather than mean flow. In the log layer the gradient of the mean velocity is given by (2.23). Hence, the production rate of TKE for a smooth wall bounded shear flow (Tennekes and Lumley 1972) is

$$-\frac{u_i u_j}{\partial x_j} \frac{\partial U_i}{\partial x_j} = \frac{u_*^3}{kz}, \quad (2.26)$$

where the Reynolds' stress is assumed equal to u_*^2 . Consider the region of the bottom mixed layer (bml) where there is no stratification. There is effectively no buoyancy flux and, hence, production equals dissipation of TKE,

$$\epsilon = \frac{u_*^3}{kz}. \quad (2.27)$$

This simple approach is only useful where $B \ll P$, which is only true where the bbl is well mixed.

2.5 Internal Waves

Another source of near bottom turbulence is internal waves. Internal waves are both generated and reflected by topography (Munk 1966; Baines 1974; Baines 1982; Eriksen 1985; Gilbert and Garrett 1989; Sjöberg and Stigebrandt 1992). This results in increased energy density of the internal wave field near topography, which may lead to increased internal wave shear and breaking, and the production of turbulence and mixing.

Some of the dynamics of internal waves in a stratified rotating fluid as developed in Kundu (1990) are outlined below. The equations of motion of linear internal gravity waves in a stratified, inviscid, Boussinesq, incompressible fluid are

$$\begin{aligned}
 \frac{\partial u}{\partial x} + \frac{\partial v}{\partial y} + \frac{\partial w}{\partial z} &= 0 \\
 \frac{\partial u}{\partial t} - fv &= -\frac{1}{\rho_0} \frac{\partial p}{\partial x} \\
 \frac{\partial v}{\partial t} - fu &= -\frac{1}{\rho_0} \frac{\partial p}{\partial y} \\
 \frac{\partial w}{\partial t} &= -\frac{1}{\rho_0} \frac{\partial p}{\partial z} + g \\
 \frac{\partial \rho}{\partial t} - \frac{\rho_0 N^2}{g} w &= 0,
 \end{aligned} \tag{2.28}$$

where f is the planetary vorticity, p is the pressure, ρ_0 is the density, g is the acceleration due to gravity and N is the buoyancy frequency. By assuming a solution for the velocity vector of the form

$$\mathbf{u} = [u, v, w] = [\hat{u}(z), \hat{v}(z), \hat{w}(z)] e^{i(kx+ly-\omega t)} \tag{2.29}$$

the equations of motion can take the form

$$\frac{d^2 \hat{w}}{dz^2} + m^2 \hat{w} = 0 \tag{2.30}$$

where

$$m(z)^2 \equiv \frac{(k^2 + l^2)[N(z)^2 - \omega^2]}{\omega^2 - f^2}, \tag{2.31}$$

and the wavenumber vector $\mathbf{K} = [k, l, m]$. If $m^2 < 0$, then \hat{w} is exponentially decaying or growing with z . If $m^2 > 0$, then \hat{w} is sinusoidal and internal waves occur. This limits the frequency band of internal waves to

$$f < \omega < N, \quad (2.32)$$

where it is assumed that $N > f$, which is true for the scope of this thesis. Assuming a slowly varying $N(z)$ with depth and orienting the x -axis in the direction of propagation, the dispersion relationship for internal waves becomes

$$\omega^2 - f^2 = \frac{k^2}{m^2}(N^2 - \omega^2). \quad (2.33)$$

The frequency of an internal wave determines the directions of its phase velocity

$$\mathbf{c} = \frac{\omega \mathbf{K}}{K^2}, \quad (2.34)$$

and group velocity

$$\mathbf{c}_g = \frac{(N^2 - f^2)km}{(m^2 + k^2)^{3/2}(m^2 f^2 + k^2 N^2)^{1/2}} [m, -k] \quad (2.35)$$

but not their magnitudes. The velocity components of the wave

$$\frac{u}{w} = \pm \frac{m}{k} = \tan \theta \quad (2.36)$$

where θ is the angle of the wavenumber vector \mathbf{K} with the horizontal. The phase velocity \mathbf{c} is in the direction of \mathbf{K} , but group velocity \mathbf{c}_g is orthogonal to \mathbf{K} . The fluid velocity \mathbf{u} is parallel to \mathbf{c}_g .

The modeling of internal wave generation has been done by ray theory (Baines 1974; Baines 1986) or local generators (Sjöberg and Stigebrandt 1992). Both models use the basic physical premise that the normal component of a barotropic tide that impinges on topography must go to zero. This results in the production of a periodic baroclinic flow, the internal tide. The ray path method has a flaw that is pointed out by Sjöberg and Stigebrandt (1992), the internal wave field at any point depends on the

entire generation area. Internal wave fields originating from separate local generators are assumed to be coherent. They argue that there should be no such coherency given the three-dimensional nature of natural slopes. By using the local generator approach at vertical steps with data bases for bathymetry, vertical density gradient, and barotropic tides, Sjöberg and Stigebrandt estimated the flux of tidal energy to turbulence via topographically generated internal tides. By using a flux Richardson number $R_f \approx 0.05$, approximately that of the global R_f (Lueck and Reid 1984), they showed that all the upward vertical transport ($15^6 \text{ m}^3 \text{ s}^{-1}$) in the deep ocean could be explained by the dissipation of topographically generated internal tides.

Eriksen (1985) argues that reflection of internal waves of all frequencies may generate sufficient turbulent mixing to provide all the upward vertical transport in the deep ocean. Upon reflection, two properties of an internal waves are conserved. The frequencies of the incident and reflected waves are equal, implying that the angles of the wavenumbers of the two waves to the vertical are equal. Therefore, two ray paths of an incident internal wave that reflects off a flat sloping bottom will either be further apart or closer together upon reflection and either decrease or increase the wavenumber's magnitude. Ray paths that are further apart upon reflection reduce the energy density of the wave by spreading its energy over a larger volume. Ray paths that are closer together upon reflection increase the energy density, which may increase the likelihood that the internal wave will become unstable and produce turbulence. If the bottom has the same slope as the wave, then a critical reflection occurs and the energy density of the reflected wave goes to infinity.

Where the boundary condition is one of no normal flow, Eriksen (1985) shows that the ratio of reflected to incident vertical wavenumbers is

$$\frac{m_r}{m_i} = -\frac{\cos(\alpha - \theta_i)}{\cos(\alpha + \theta_i)} - \frac{\sin 2\theta_i \sin 2\alpha (\cos \phi_i - 1)}{2 \cos(\alpha + \theta_i) \cos(\alpha - \theta_i)} \quad (2.37)$$

where $s = \tan \alpha$ is the bottom slope, $\tan \theta = m(k^2 + l^2)^{1/2}$ and subscripts i and r refer to incident and reflected values. Azimuth ϕ corresponds to the ray path normal

to the isobaths and $\tan \phi = k/l$. When the incident wave is inclined the same as the bottom slope, reflected waves are unable to propagate away from the boundary. This arises at the critical frequency of

$$\omega_c^2 = \frac{N^2 s^2 + f^2}{1 + s^2}. \quad (2.38)$$

The ratio of the energy density of the reflected and incident waves is

$$\frac{E_r}{E_i} = \left(\frac{m_r}{m_i} \right)^2. \quad (2.39)$$

Eriksen (1985) shows a number of conditions where the energy density of the wave can be amplified upon reflection. There are a large hierarchy of results but these are not important for the work at Cobb. What is required is a spectrum of waves incident on bottom with varying slope.

Eriksen (1985) determines the effect of an incident internal wave field that follows the Garrett-Munk (GM) spectrum (Munk 1981) reflecting off a flat sloping bottom. The spectrum of the reflected wave was amplified at frequencies close to the critical frequency. Using the observational requirement that the spectrum of the internal wave field must readjust to the GM spectrum a few hundred meters above the bottom, Eriksen computed a redistributed energy flux normal to the bottom; the difference in the energy density of the incident and reflected wave fields integrated over all azimuths, frequencies and wavenumbers. Only a small percentage of the redistributed energy flux needs to go into turbulence and mixing to produce an effective vertical diffusivity $K_v = 10^{-4} \text{ m}^2 \text{ s}^{-1}$ in the world's oceans.

Gilbert and Garrett (1989) developed the response of internal waves reflecting from a bottom of varying slope. They suggest that concave sites are less likely than convex sites to show energy enhancement near the critical frequency. Hence, dissipation rates associated with internal wave breaking should be higher near convex topography rather than concave topography. However, they note that the most convincing evidence of energy and shear enhancement near ω_c was near topography that

was neither concave nor convex, but had a nearly constant slope.

2.6 Large Scale Mixing

I am particularly interested in Cobb Seamount with respect to the amount of mixing occurring around it. There has been a continuing debate as to where the mixing in the ocean occurs. It has been well understood that there is enhanced turbulence and mixing near continental margins, in coastal waters, around islands and near seamounts (Dewey 1987; Eriksen 1985; Osborn 1978; Nabatov and Ozmidov 1988; Toole *pers. comm*). Whether this enhanced mixing occurs over a wide enough area to affect the overall mixing in the ocean is uncertain.

This debate, as pointed out by McDougall (1989), is inspired by the difference in vertical diffusivity required by ocean models versus measurements of vertical diffusivities in the open ocean. The Stommel and Arons (1960) model for the circulation of the deep ocean presents an upwelling velocity field that is homogeneous in both latitude and longitude, and increases linearly with height above the bottom. For the upwelling velocity field to balance the deep water formation rate requires a vertical diffusivity $K_v \approx 10^{-4} \text{ m}^2 \text{ s}^{-1}$. Munk (1966) assumed a simple vertical advective-diffusive balance within the deep-central Pacific, where the renewal of bottom water was assumed to occur at great depths. Thus, from vertical profiles of temperature and salinity he acquired a *scale height* $K_v/w \approx 1 \text{ km}$ and from vertical profiles of Carbon 14 he acquired a *scale time* $K_v/w^2 \approx 200 \text{ years}$. Munk estimated the upward vertical velocity and vertical diffusivity in the deep Pacific as $w \approx 4.4 \text{ m year}^{-1}$ and $K_v \approx 1.3 \times 10^{-4} \text{ m}^2 \text{ s}^{-1}$. Indirect measurements of vertical diffusion by microstructure observations (Lueck *et al.* 1983; Gregg 1987; Schmitt *et al.* 1994; Polzin *et al.* 1994) in the open ocean have put $K_v \approx 10^{-5} \text{ m}^2 \text{ s}^{-1}$ over a depth range of 25–3000 m. The indirect nature of these measurements has been criticized; however, recent direct

measurements of vertical diffusion by a tracer experiment in the North Atlantic (Ledwell *et al.* 1993) has shown the microstructure estimates are robust, with an error of less than a factor of 2. The order of magnitude difference in vertical diffusivity between models and measurements in the open ocean has led to the argument that a large portion of the ocean's mixing occurs at its boundaries.

The significance of boundary mixing was postulated by Munk (1966). Temperature and salinity (T-S) characteristics acquired at the boundaries are readily transferred along isopycnals or, more correctly, along neutral surfaces (McDougall 1989). Isopycnals that outcrop at high latitudes may be as deep as 1 km at low latitudes. Thus, the surface boundary may be vital to the upper ocean (< 1 km deep) while the bottom boundary may be vital to the deep ocean. The efficiency of near boundary processes in mixing the oceans is uncertain. Armi (1978) and Phillips *et al.* (1986) have indicated processes that can advect mixed water at a sloping boundary into the ocean interior; however the efficiency of mixing within a turbulent wall bounded layer may be quite small. Garrett (1979) argues that the strongest turbulence occurs within the bottom mixed layer and contributes negligible effective mixing in the already diminished stratification. The near boundary mixing originating from internal waves reflecting (Eriksen 1985; Gilbert and Garrett 1989) and generating (Baines 1982; Sjöberg and Stigebrandt 1992) from the bottom is not limited by the problem of restratification in the bml. The enhanced turbulence from internal wave breaking and shear occurs 100's of meters above the bottom, which is well above the typical 10's of meters of the mixed layer.

Armi (1978), McDougall (1989) and Garrett (1991) discuss the hypothesis that strong mixing near the bottom boundary is equivalent to weaker mixing throughout the open ocean. McDougall (1989) has it in the form

$$K_b A_b = K_i^{eff} A_i \quad (2.40)$$

where K_b is the vertical diffusivity near the boundary, A_b is the area of the enhanced

mixing near the boundary, K_i^{eff} is the effective diffusivity that the boundary mixing produces in the ocean interior and A_i is the area of the ocean interior. This model (2.40) is true only where the vertical density gradient is horizontally uniform. What we really need to compare is the mass flux near the bottom boundary versus the mass flux in the open ocean. This approach is used later in this thesis to show the significance of mixing at Cobb and other seamounts for mixing the world's oceans.

Chapter 3

Equipment and Data Processing

3.1 Measurement Positions

Measurements with the FLY II free fall microstructure profiler were taken around Cobb Seamount between June 23 and June 30, 1992. This was part of a cruise to Cobb on the *CSS Tully* which left Victoria on June 22 and returned on July 1. There were three groups aboard. The Freeland and Dower group deployed three current meter moorings and 2 satellite tracked drifters, and performed CTD/rosette and zooplankton surveys. The Juniper and McBell group incubated samples from the CTD rosette. The Lueck group, of which I was a member, deployed an Acoustic Doppler Current Profiler (ADCP) and performed a microstructure survey with FLY II.

With the microstructure survey, eight series of profiles were performed numbered from 0 to 7. Series 0 was a set of profiles, and shipboard tests. During one of the profiles the retrieval line became entangled with the bottom and the profiler stayed on the bottom for over 30 minutes. Series 1 involved only one profile during which the retrieval line was entangled for over 2 hours. Series 2 suffered from radio transmission interference and winch problems. None of the profiles from these series have been converted to physical units.

The first successful set of profiles was series 3. This was an attempt at a 24 hour time series on the eastern flank of the seamount (Fig. 3.3). After a number of successful profiles above the bottom, a new retrieval technique, referred to as the *kiss and run* method, was developed that allowed profiling to the bottom with a reduced chance of

	<i>series</i>			
	3	4	5	6
profiles	68	9	39	25
start day	27	28	29	29
start time	16:15	00:46	14:44	22:50
series length [hour]	19.58	5.05	6.88	2.90
transect distance [km]	N/A	N/A	13.9	4.8
mean time between profiles [min]	17.5	37.9	10.9	7.2
median time between profiles [min]	12.1	36.6	11.2	8.1
mean distance between profiles [km]	0.71	0.76	N/A	N/A
median distance between profiles [km]	0.46	N/A	N/A	N/A

Table 3.1: Characteristics of each successful series.

line entanglement. At the beginning of each profile a depth sounding was taken. Using the real time display of pressure from FLY II we determined when the instrument was 10–20 m above the bottom and then began to retrieve the line, thereby reducing slack in the line, which reduced the chance of line entanglement. Some of our profiles using this technique did not end at the bottom because the depth sounder determines the depth with some horizontal averaging; hence, the water column through which the instrument fell was as much as ± 20 m deeper. An equipment failure ended series 3 after less than 20 hours. There were two breaks of over 1.5 hours, both were on June 28 at about 01:30 and 16:30 hours PDT.

Series 4 coincided with a 12 hour CTD time series by the Freeland and Dower group (Fig. 3.4). Series 5 and 6 were transects of the seamount beginning at the pinnacle. Series 5 extended from the pinnacle to the southeast and series 6 extended from the pinnacle to the east (Fig. 3.5). All positions were measured by the Global Positioning System (GPS) at the start of the profiles. The accuracy is claimed to be ± 30 m, but Lueck (*pers. comm.*) has determined the rms fluctuations to be as large as 100 m. The currents advected FLY II. during its free-fall, horizontally 10–50% of the profile depth.

Series 7, an attempt at following turbulent patches, did not prove to be very

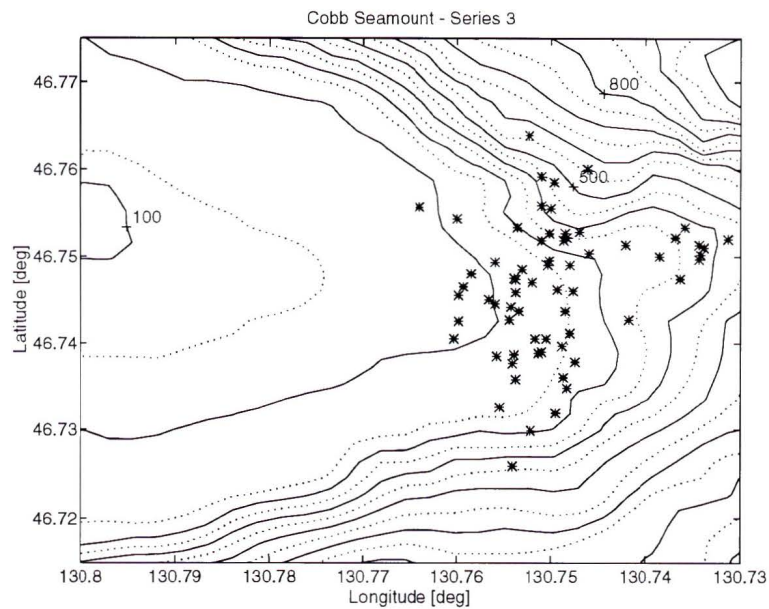


Figure 3.3: Positions of series 3 profiles. Solid line contours begin at 100 m and continue at 100 m intervals; dashed line contours begin at 150 m and continue at 100 m intervals.

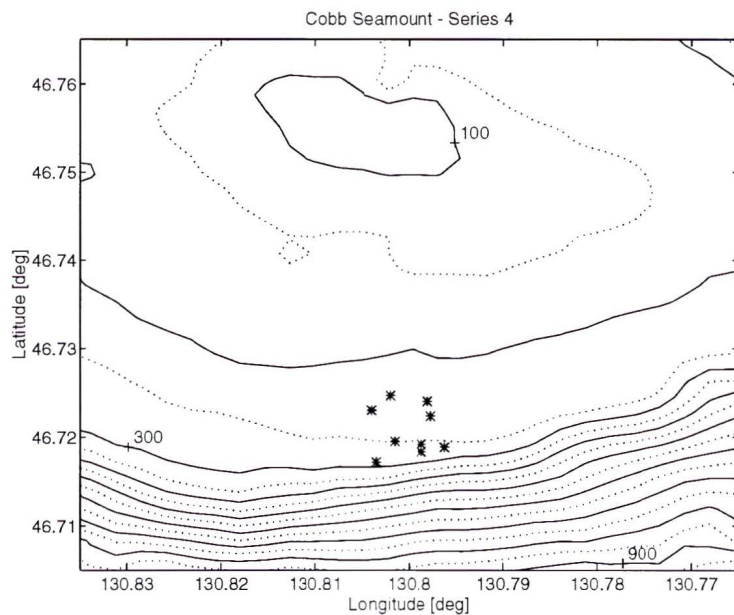


Figure 3.4: Positions of series 4 profiles. Solid line contours begin at 100 m and continue at 100 m intervals; dashed line contours begin at 150 m and continue at 100 m intervals.

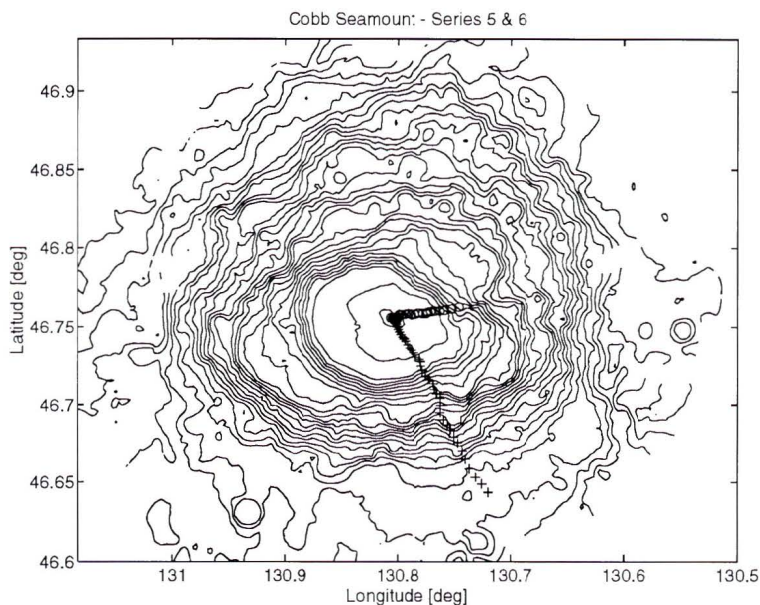


Figure 3.5: Positions of series 5 (+) and 6 (o) profiles. The contour lines are at every 100 m where the minimum contour is 100 m.

successful and no data from this series has been converted to physical units. Only series 3, 4, 5 and 6 have been processed and used in this thesis. These series are also respectively referred to as the 19 hour time series, the CTD time series, transect 1 and transect 2.

3.2 FLY II Profiler

The FLY II (Fast Light Yo-yo) was designed as a microstructure free falling profiler that could land on the bottom (Dewey *et al.* 1987). It is able to simultaneously measure vertical gradients of the horizontal perturbation velocities, temperature, conductivity and pressure. With the probe guard installed, the instrument's nose mounted sensors profile to within 15 cm of the bottom. Unfortunately, the instrument proved to be prone to tangling with basalt columns or boulders on the bottom with its almost neutrally buoyant KevlarTM retrieval line.

For the June 1992 cruise at Cobb, FLY II was equipped with airfoil ceramic shear probes ($\frac{du}{dt}$), two fast response thermistors (T_1 and T_2), a SeaBirdTM conductivity cell

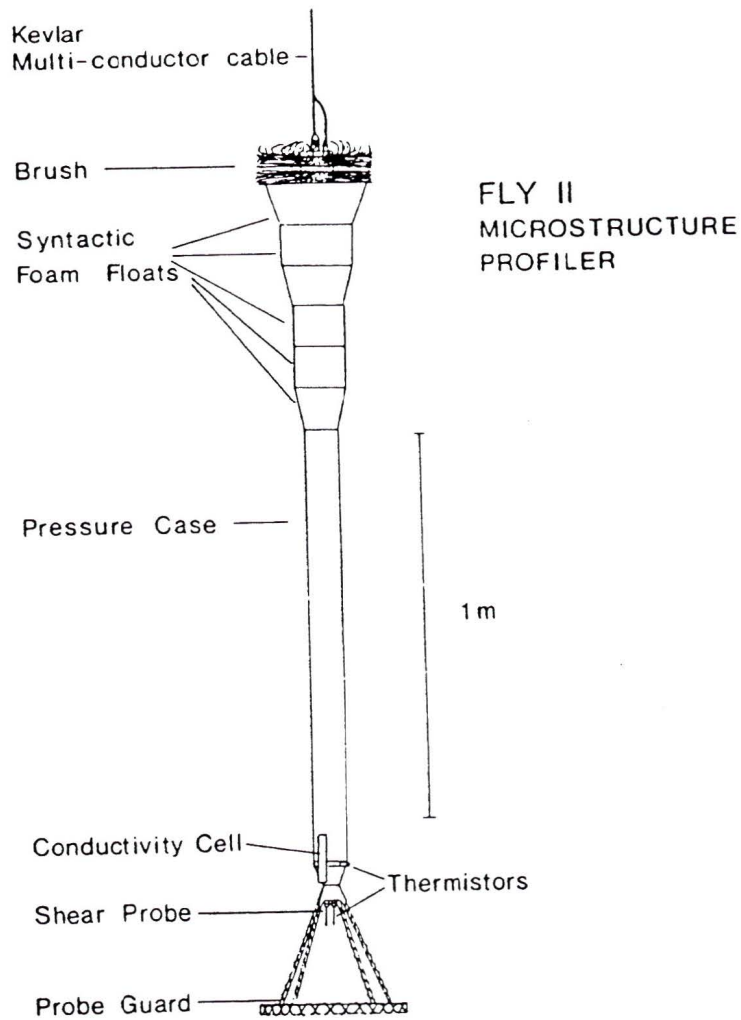


Figure 3.6: The FLY II free-falling microstructure profiler. This is the same configuration as used during the June 1992 cruise with the exception of the brush, which was replaced with increased flotation (adapted from Dewey 1987).

	<i>series</i>			
	3	4	5	6
fast 1	$\frac{du}{dt}$	$\frac{du}{dt}$	$\frac{du}{dt}$	$\frac{du}{dt}$
fast 2	$\frac{du}{dt}$	$T_1 + \alpha^{-1} \frac{dT_1}{dt}$	$T_1 + \alpha^{-1} \frac{dT_1}{dt}$	$T_1 + \alpha^{-1} \frac{dT_1}{dt}$
slow 1	$\frac{dT_2}{dt}$	$\frac{dT_2}{dt}$	$\frac{dT_2}{dt}$	$\frac{dT_2}{dt}$
slow 2	Battery	Battery	Battery	Battery
slow 3	T_2	T_2	T_2	T_2
slow 4	P	P	P	P
slow 5	$\frac{dT_2}{dt}$	$\frac{dT_2}{dt}$	$\frac{dT_2}{dt}$	$\frac{dT_2}{dt}$
slow 6	Tilt1	Tilt1	Tilt1	Tilt1
slow 7	C	C	C	C
slow 8	Tilt2	Tilt2	Tilt2	Tilt2

Table 3.2: Signals recorded on the fast and slow channels.

(C), a pressure transducer (P) and two tilt gauges. The T_1 signal was not recorded as is but was instead added to its scaled time derivative. The reasons for this will become clear later in this chapter. The time derivative of T_2 and the internal power supply (alkaline c-cells) voltage were also recorded. Analog boards and analog to digital (A/D) electronics were contained within the pressure case. Sensor signals were digitized by a 12 bit A/D converter with 2 fast channels, sampled at $1920/7 \approx 274$ samples per second, and 8 slow channels, sampled at $240/7 \approx 34$ samples per second (Table 3.2). The A/D converter ranged from -2048 to 2047 counts, which corresponds to voltage of -5 to +5 volts. The digitized signals were transmitted in real time through conductors in the retrieval line and logged by a personal computer (PC) on deck. Data files were later transferred to magnetic tape as a permanent archive.

3.3 Digital Signal Processing of FLY II Data

In post-cruise processing the data files from the successful series were demultiplexed and truncated before being converted to physical values. The data files were demultiplexed on a PC and were then transferred to a UNIX based machine and converted to IEEE standard from the IBM PC standard. Poor quality data at the beginning

and end of the files were removed by truncating the files. Surface waves produced a pitching motion of the profiler that decayed away by 10 m. This motion contributed to the shear probe signals and had to be removed. Data collection was usually ended after the instrument hit the bottom or after the instrument was beginning to rise during its retrieval when no bottom hit occurred. The time of a bottom hit could be approximately resolved with depth and tilt signals, but it was the shear probes that reacted the most swiftly and sharply to the impact. All data after the impact were removed. For the profiles where no impact occurred, the first indication that the instrument was beginning to reduce its fall speed, due to retrieval, was taken as the end of the file and all remaining data were truncated.

3.3.1 Pressure and Fall Speed

The pressure transducer voltage signal V_p was recorded on one of the slow channels. It was converted to physical units by the calibration

$$P = A_p + B_p V_p \quad (3.41)$$

$$\text{Range} : -63.0 \text{ to } 368.2 \text{ m}$$

$$A_p = 152.61 \text{ m}$$

$$B_p = 43.11 \text{ m V}^{-1}.$$

The signal was then smoothed forwards and backwards with a Butterworth filter which had a 1/4 Hz cutoff frequency. This ensured that no phase lag was created during the filtering process. The smoothing was necessary to produce a fall speed that was not contaminated by the high frequency noise of the original pressure signal. The fall speed was calculated by taking the first difference of the smooth pressure signal and dividing by the sampling time for a slow channel ($T_s = 0.0292 \text{ s}$).

3.3.2 Low Resolution Temperature and Temperature Gradient

FLY II was equipped throughout the experiment with one FP07 fast response thermistor in its nose. The signal voltage for this thermistor V_t was recorded on one of the slow channels. The calibration was

$$T_2 = A_t + B_t V_t + C_t V_t^2 + D_t V_t^3 \quad (3.42)$$

$$\text{Range} : -2.42 \text{ to } 27.90 \text{ }^\circ\text{C}$$

$$A_t = 14.5589 \text{ }^\circ\text{C}$$

$$B_t = 2.68429 \text{ }^\circ\text{C V}^{-1}$$

$$C_t = 0.0241041 \text{ }^\circ\text{C V}^{-2}$$

$$D_t = -0.00546280 \text{ }^\circ\text{C V}^{-3}.$$

The signal was differentiated by analog circuits before the A/D conversion. Two of the slow channels were filled with the temperature derivative voltage signal $V_{\frac{dT_2}{dt}}$ which was converted to temperature gradient with

$$\frac{dT_2}{dz} = \frac{V_{\frac{dT_2}{dt}} (B_t + 2C_t V_t + 3D_t V_t^2)}{GW} \quad (3.43)$$

$$\text{Range} : -56.4 \text{ to } 56.4 \text{ }^\circ\text{C m}^{-1}$$

$$G = 0.19 \text{ s},$$

where W is the fall speed and G is the gain of the differentiator circuit.

3.3.3 Conductivity and Salinity

The signal from the SeaBirdTM conductivity cell was converted from a frequency signal into a voltage V_c . The calibration for conductivity ratio was

$$C = A_c + B_c V_c + C_c V_c^2 + D_c V_c^3 \quad (3.44)$$

$$\text{Range} : 0.3509 \text{ to } 1.2405$$

$$A_c = 0.728952$$

$$\begin{aligned}
 B_c &= 0.0893144 \text{ V}^{-1} \\
 C_c &= 0.00266985 \text{ V}^{-2} \\
 D_c &= -0.0000145388 \text{ V}^{-3}
 \end{aligned}$$

The conductivity ratio, temperature and pressure were converted to salinity using the Lewis and Perkin (1981) method.

Salinity, the total amount of solids in grams contains in one kilogram of water when all the carbonate has been converted to oxide, the bromine and iodine replaced by chlorine and all organics oxidized, is measured indirectly with conductivity, temperature and pressure. This empirically determined *practical* salinity has a precision of ± 0.003 psu (practical salinity units). Salinity spiking was initially a serious problem (Fig. 3.7). Short term anomalous spikes of over 0.2 psu occurred and longer term problems produced anomalous non-monotonic salinity profiles. The temperature signal was processed for the mismatch between the temperature and conductivity signals, which was the cause of the spiking. Three different lags in the conductivity signal created the mismatch, two were short term lags and one was a long term lag.

The simplest of the short term time lags was primarily due to the placement of the conductivity cell 15 cm downstream of the thermometer. The correction of the lag produced a temperature

$$T_2^{c1}(n) = T_2(n - 24), \quad (3.45)$$

where n is the sample number and the subscript 2 indicates that this is the temperature signal recorded in one of the slow channels (Table 3.2). The result (Fig. 3.7) was the reduction of some of the short term spiking. The other short term lag was discovered when the transfer function from temperature to conductivity was calculated for the isohaline region above 100 m. In this region changes in conductivity were almost entirely due to changes in temperature: hence the transfer function should have been flat if there was no mismatch between the two signals. However, the transfer function

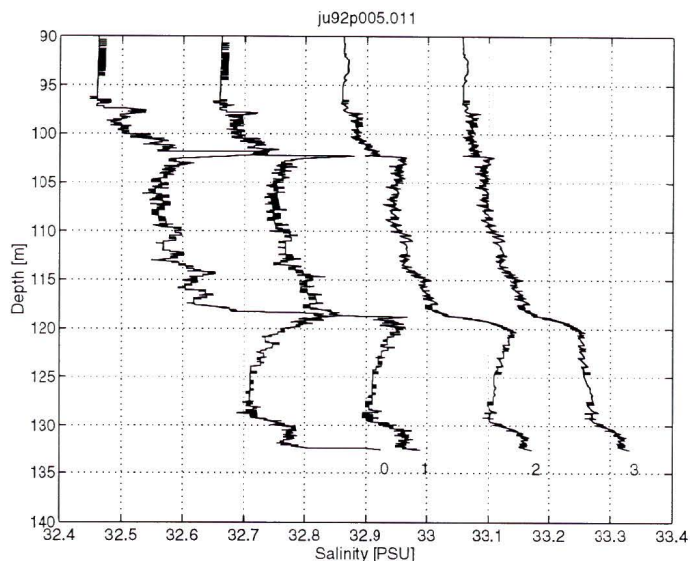


Figure 3.7: Profiles of salinity after various levels of temperature correction. The labeled profiles had: (0) no correction, (1) a lag of 24 units, (2) a lag of 24 units and the Butterworth filter, and (3) a lag of 24 units, the Butterworth filter, and thermal inertia correction.

was not flat but was similar to a first order Butterworth with cutoff frequency of $f_c = 0.52$ Hz. The relative reduction in the frequency response of conductivity was a result of the spatial averaging between the electrodes in the cell and boundary layer effects within the cell. A digital Butterworth filter with this cutoff frequency was applied to the temperature signal. With the two short term corrections applied to the temperature signal, all of the short term spiking was removed (Fig. 3.7). The second correction also reduced quantization noise, as can be seen between 90 and 95 m. The corrections did not remove a longer term mismatch that implied the water column was unstable in salinity at some depths.

A long-term lag in the conductivity signal, due to the thermal capacity of the SeaBirdTM conductivity cell, was reported and corrected by Lueck (1990) and Lueck and Picklo (1990). They modified the conductivity signal to reduce the signal mismatch. Unfortunately, the method required prior knowledge of the temperature coefficient of conductivity and a temperature signal corrected for short-term mismatch as well as the conductivity signal. Further work by Morison *et al.* (1994) was merely

a change in Lueck's algorithm. They modified the temperature signal rather than the conductivity signal. This method is simpler because it does not require any prior knowledge of the temperature coefficient of conductivity and requires no knowledge of the conductivity signal. The velocity dependent filter they applied is

$$T_2^{c3}(n) = -bT_2^{c3}(n) + aT_2^{c2}(n) - aT_2^{c2}(n-1), \quad (3.46)$$

where

$$a = \frac{4f_N\alpha\tau}{1 + 4f_N\tau}, \quad (3.47)$$

$$b = 1 - \frac{2a}{\alpha}, \quad (3.48)$$

$$\alpha = \frac{0.1018}{W - 0.0256}, \quad (3.49)$$

$$\tau = \frac{6.7856}{\sqrt{W} + 4.4015}, \quad (3.50)$$

T_2^{c3} is the temperature corrected for the thermal inertial effect, T_2^{c2} is the temperature corrected for the two short term lags, f_N is the Nyquist frequency and W is the fall speed. Removing the two short term lags and one long term lag resulted in a dramatic reduction in the salinity spiking (Fig. 3.7).

3.4 Enhanced Temperature

The digital temperature signal that was produced with the FP07 thermistor discussed in section 3.3.2 had insufficient resolution for some applications. We considered that if the signal spanned the full oceanic temperature range then it would not have sufficient resolution to determine the temperature changes in the bottom boundary layer nor was it useful in determining Thorpe scaling where overturns were small or in regions of low temperature gradient; however the original analog temperature signal did have sufficient resolution for our needs. The reduction in temperature resolution was the result of digitization, which created quantization noise, the difference between an analog signal and its digitized signal. For series 4-6, one of the two shear

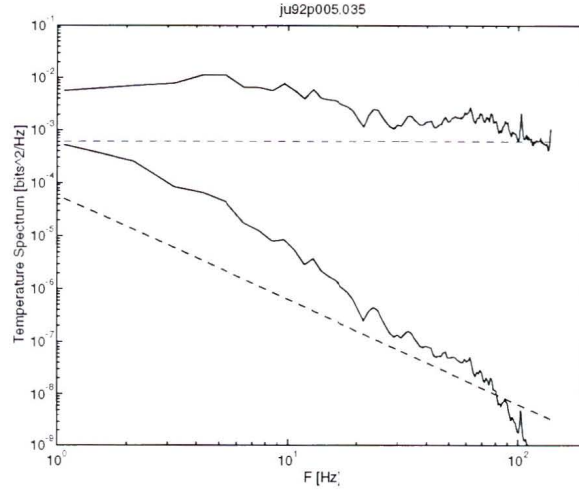


Figure 3.8: Spectra of 30 s of quiescent data; pre-emphasized digital signal (upper solid curve) and its quantization noise spectrum (upper dashed line); enhanced digital signal (lower solid curve) and its quantization noise spectrum (sloping dashed line).

probes mounted in FLY II's nose was removed and was replaced with a second FP07 thermistor. By adding a special analog circuit to FLY II to pre-emphasize the analog signal from this second thermistor, we reduced the effects of quantization noise and, thereby, created a higher resolution digital temperature signal. This follows the method of Mudge and Lueck (1994) of combining an oceanic signal plus its scaled time derivative to produce a pre-emphasized signal before digitization. The combined digital signal is then deconvolved into an enhanced digital oceanic signal with a digital filter. The method is simple to apply, numerically efficient and very effective in reducing quantization noise and increasing signal resolution.

The spectrum of the noise (Fig. 3.8) in the enhanced digital signal is

$$\Phi_e(\Omega) = \frac{1}{1 + \Omega^2/\alpha^2} \Phi \quad (3.51)$$

where Ω is the angular frequency, the gain of the differentiator is $\alpha^{-1} = 0.50$ s and Φ , the spectrum of the quantization noise of the pre-emphasized digital signal, is a constant. If the scaled time derivative had not been added to the the analog temperature signal, the spectrum of the noise in the digital signal would have been Φ . Hence, the enhanced signal has the same noise level as an unenhanced signal for

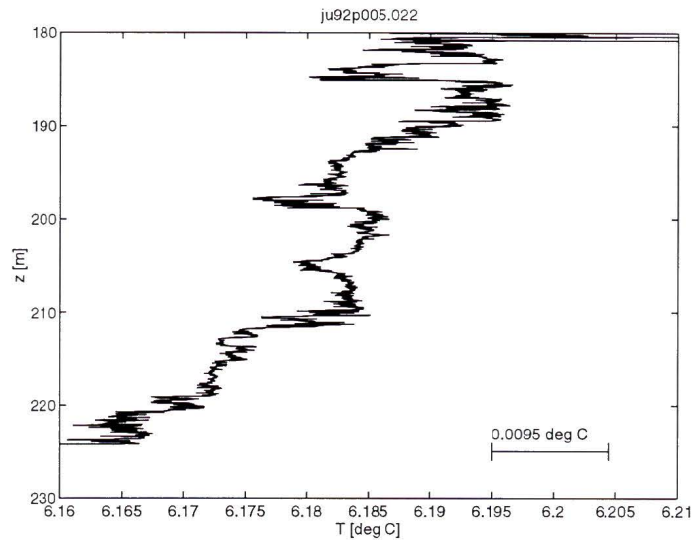


Figure 3.9: A 50 m segment of temperature off the seamount from transect 1. This section is turbulent and had a mean vertical gradient of less than $1 \text{ m}^0\text{C m}^{-1}$. The solid horizontal line indicates the size of a bit prior to pre-emphasis.

$\Omega \ll \alpha$ while at all higher frequencies there is considerable reduction in the noise, with the greatest reduction at the highest frequencies.

The spectra of the pre-emphasized digital signal shows the pre-emphasized analog signal dominates quantization noise over the entire resolvable frequency band (Fig. 3.8). Therefore, the enhanced digital signal is a good approximation of the original analog temperature signal for all frequencies. From Fig. 3.8 it is clear that without the pre-emphasis the original signal would have been dominated by noise for all frequencies above 1 Hz. By pre-emphasis we have increased the useful frequency band of our temperature signal to the limit where the signal may be interpreted as temperature. There is attenuation of the temperature signal above 20 Hz due to the thermistor and above 50 Hz there is significant attenuation due to the analog electronics. Therefore, it is unrealistic to consider improvement in the signal to noise ratio above 50 Hz. At 50 Hz the improvement in resolution of the signal was about 160. Hence, pre-emphasis has raised the resolution from $9.5 \text{ m}^0\text{C}$ to $60 \mu^0\text{C}$ at 50 Hz. The increase in resolution allows us to produce Thorpe scaling for turbulent patches

with a small mean temperature gradient, such as the 50 m patch in Fig. 3.9. Many of the overturns in the 50 m section would be unresolvable if the temperature signal was not enhanced.

The overall improvement in variance of the signal by the pre-emphasis is

$$\frac{\sigma_e^2}{\sigma^2} = \frac{\pi}{2} \frac{\alpha}{\Omega_N} \quad (3.52)$$

where σ_e^2 and σ^2 are the variances of the quantization noise in the enhanced and pre-emphasized digital signals, while Ω_N is the Nyquist frequency of the digital signal. The overall reduction in variance in the signal was 16^2 and if we ignore data above 50 Hz the reduction was 10^2 .

3.5 ϵ as Determined by Microstructure Shear

3.5.1 Removal of Anomalous Signals in Microstructure Shear

Microstructure shear, and thereby the rate of dissipation of TKE ϵ , was among the most difficult physical values to determine. The initial processing of the microstructure shear involved removal of anomalous spikes and periods of high variance that were unrelated to oceanic turbulence.

Spiking in the shear signal is suspected to be primarily due to particle hits on the probes. Spiking and its possible sources are more completely discussed in chapter 8. Other anomalous shear signals were probably the result of guard hits of larger objects, fish wakes, or objects that vibrate, such as jellyfish, attaching to the profiler. All of these anomalous signals increase the power of the shear signal in the band of frequencies that are of interest; hence these anomalous signals can significantly contribute to the variance of the shear and bias the estimated dissipation rates.

Identification and removal of anomalous signals was performed interactively. Unprocessed signal from a shear probe was plotted in 2000-point sections along with temperature gradient for the section and, when available, the shear signal from the

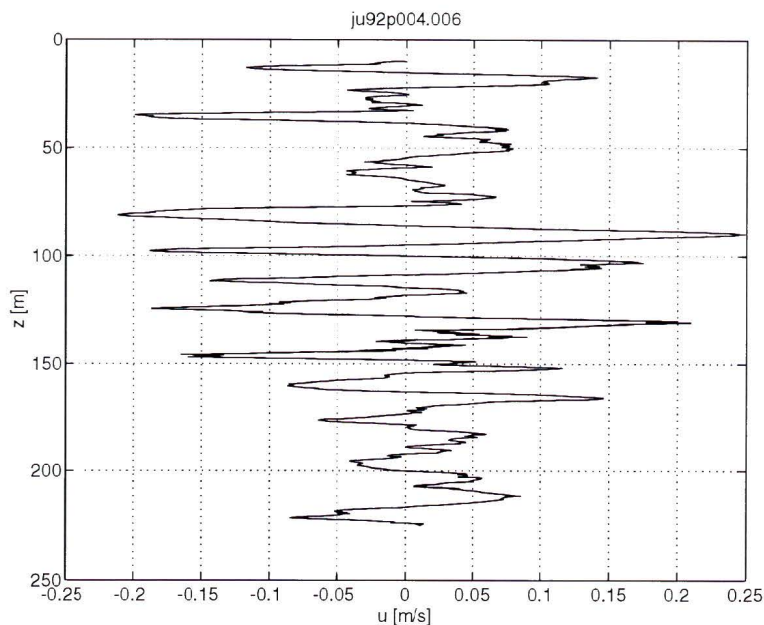


Figure 3.10: Vertically integrated microstructure shear.

other probe. By comparing the three signals and by finding very short sections of signal with anomalously high variance, spikes were identified. Each spike plus 10 points on both sides of the spike were removed and replaced by the mean of the 20 points surrounding the removed section (Fig. 8.46).

Once spikes were removed, the shear signal was filtered to remove regions of the frequency band that were biased by movement and vibration of the profiler. The guard on FLY II was wrapped with nylon line to reduce von Karman vortex shedding, which proved to be a major noise source. The wrapping was recognized by Dewey (1987) to reduce significantly the approximate 30 Hz vibration and overtones of the vortex shedding, however it created a torque on the profiler that caused it to spin in one direction as it fell. Most of this torque was removed by wrapping the guard in both directions. This still leaves some torque on the profiler as can be observed in Fig. 3.10. There is periodic reversal of the velocity with a length scale of 15 m which is probably due to rotation of the instrument. To remove this effect, the shear series was high passed filtered in one direction by a second-order Butterworth filter

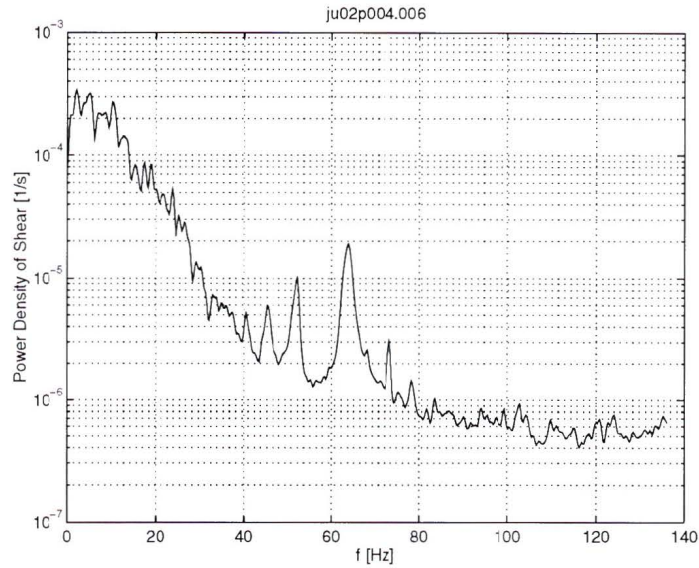


Figure 3.11: Power density spectrum of microstructure shear. From 0–40 Hz the spectrum is dominated by turbulence. From 40–70 Hz the spectrum is dominated by three large spikes that are due to body vibrations. Above 70 Hz the spectrum is dominated by white noise due primarily to quantization. The dissipation rate for the data is $1.4 \times 10^{-7} \text{ W kg}^{-1}$.

with a 0.5 Hz half power cutoff frequency. Vibrations in the profiler were observed at higher frequencies, primarily around 60 Hz (Fig. 3.11). The main pressure case is suspected to have a vibrational oscillation at 64 Hz (Crawford *pers. comm.*). The lower frequency vibrations are probably the result of the guard on the FLY II. Removal of most of these signals was accomplished by a ninth order elliptical filter with a 50 Hz cutoff frequency. This does not dramatically bias most of our results for dissipation. At 50 Hz and a fall speed of $.5 \text{ m s}^{-1}$ the probe resolves only 20% of the power density of the shear. If the dissipation rate is $\approx 10^{-6} \text{ W kg}^{-1}$, then over 95% of the variance of the shear is due to turbulence below 50 Hz. The percentage is even higher for lower dissipation rates. If needed, the bias can be corrected for dissipation rates $> 10^{-6} \text{ W kg}^{-1}$.

3.5.2 Spectral Estimates of ϵ

The despiked and filtered shear probe signal was then converted to vertical shear of u , a horizontal component of the fluctuating velocity field;

$$\frac{\partial u}{\partial z} = \frac{1}{W} \frac{\partial u}{\partial t} = \frac{V_0}{2\sqrt{2}GSW^2}, \quad (3.53)$$

where V_0 is the differentiated voltage of the shear probe, G is the gain in the differentiator, S is the sensitivity of the shear probe, and W is the fall speed of the instrument.

The total rate of dissipation is

$$\epsilon = \frac{1}{2} \nu \overline{\left(\frac{\partial u_i}{\partial x_j} + \frac{\partial u_j}{\partial x_i} \right)^2}, \quad (3.54)$$

where ν is the kinematic viscosity, repeated indices indicate summation and the overbar implies a spatial average (Tennekes and Lumley 1972). A shear probe senses only one component (u) of the fluctuating velocity field, and u varies in both space and time. The probe must traverse a turbulent field with a speed (W) large enough ($u \ll W$) that we can assume the frozen-turbulence approximation and take our average for (3.54) as a spatial average (Tennekes and Lumley 1972). For isotropic turbulence (Oakey 1982)

$$\overline{\left(\frac{\partial u_i}{\partial x_j} + \frac{\partial u_j}{\partial x_i} \right)^2} = 15 \overline{\left(\frac{\partial u}{\partial z} \right)^2}, \quad (3.55)$$

thus under ideal circumstances for a continuous-time signal

$$\epsilon = 7.5 \nu \overline{\left(\frac{\partial u}{\partial z} \right)^2} = 7.5 \nu \int_0^\infty \Phi(f) df, \quad (3.56)$$

where $\Phi(f)$ is the power density spectrum of the microstructure shear as resolved in frequency space f which has a corresponding cyclic wavenumber $\hat{k} = f/W$. The rate of dissipation is calculated in $W \text{ kg}^{-1}$. For oceanic turbulence it is not necessary to integrate the power density from 0 to ∞ . From the empirical universal spectrum

determined by Nasmyth (1970), of which Oakey (1982) published 15 data points, over 95% of the variance of the microstructure shear comes from the band 0.0039–0.12 in normalized wavenumber space \hat{k}/k_s , where

$$k_s = (\epsilon\nu^{-3})^{1/4} \quad (3.57)$$

is the Kolmogorov wavenumber. For the case of $\epsilon = 10^{-6} \text{ W kg}^{-1}$, $W = 0.56 \text{ m s}^{-1}$ and $k_s = 796 \text{ m}^{-1}$, the integration limits in frequency space are 1.7 and 53.5 Hz, which is approximately the frequency band unaffected by filtering.

There are two methods of determining the variance of microstructure shear as suggested by (3.56), either a spatial average (Yamazaki and Lueck 1990) or the classical approach of spectral integration (Osborn 1974). The spatial average technique provides a higher spatial resolution but suffers from a poorer dissipation resolution than the spectral integration technique. I will first explain the technique of spectral integration and then I will develop the technique of spatial average.

The first technique for determining the variance of the shear signal was by the summation of the shear signal's power spectrum estimate Φ_i . The shear series was divided into sections of $M = 1024$ points, with a spatial scale of $\approx 2 \text{ m}$. A spectrum Φ_i was determined over each section by one periodogram using a Hanning window. The i^{th} component of the power spectrum Φ_i has a corresponding frequency

$$f_i = (i - 1) \frac{f_N}{M}, \quad (3.58)$$

where f_N is the Nyquist frequency. Hence, the corresponding cyclic wavenumber is $\hat{k}_i = f_i/W$.

The spectrum was smoothed by a running mean with a 5-point window and was then corrected for the roll-off response at high frequencies for the Osborn type shear probes. The correction developed by Ninnis (1984) is

$$T_i = 1.000 - 0.164 \left(\frac{\hat{k}_i}{\hat{k}_0} \right) - 4.537 \left(\frac{\hat{k}_i}{\hat{k}_0} \right)^2 + 5.503 \left(\frac{\hat{k}_i}{\hat{k}_0} \right)^3 - 1.804 \left(\frac{\hat{k}_i}{\hat{k}_0} \right)^4, \quad (3.59)$$

where $\hat{k}_0 = 1.7 \times 10^2 \text{ m}^{-1}$ is the zero response cyclical wavenumber for Osborn type shear probes. The corrected spectrum is then

$$\Phi_i^c = \frac{\Phi_i}{T_i}. \quad (3.60)$$

For a continuous shear signal, the variance can be estimated by integrating part of the spectrum

$$\sigma_e^2 = W \int_0^J \Phi^c(\hat{k}) d\hat{k}. \quad (3.61)$$

Assuming the spectrum follows the universal spectrum, the limit J can be chosen such that σ_e^2 is 85% of the total variance. Unfortunately, to determine J exactly requires prior knowledge of the total variance.

For the discrete signal, estimating J and, hence, σ^2 is reasonably simple. A series of cumulative sums of the smoothed and corrected spectrum was determined

$$\sigma_j^2 = \sum_{i=1}^j \Phi_i^c, \quad (3.62)$$

from which I estimated dissipation rate series

$$\epsilon_j = 7.5\nu\sigma_j^2, \quad (3.63)$$

and partial Kolmogorov wave number series

$$k_{sj} = (\epsilon_j\nu^{-3})^{1/4}. \quad (3.64)$$

The point where $\hat{k}_j/k_{sj} \approx 0.075$ was found. The cumulative sum of the spectrum at this point resolved 85% of the total variance, assuming that the spectrum follows Nasmyth's universal spectrum; however our estimate of k_{sj} was about 95% of its true value, which produced an underestimation of the total variance of a few percent. This error has been ignored. Where $\hat{k}_j/k_{sj} \approx 0.075$ was true for $\hat{k}_j < 10$ cpm, the end point of the sum of Φ_i^c was taken at $\hat{k}_j \approx 10$ cpm. If $\hat{k}_j/k_{sj} \approx 0.075$ was true for $f_j > 50$ Hz, the cutoff frequency of the elliptical filter, then the end point was taken

at $f_j \approx 50$ Hz. By performing a spline fit to Nasmyth's universal spectrum for the value of \hat{k}_j/k_{sj} used as the end point of the integration, I determined the fraction F_U of the total variance integrated. The spectral estimate for the dissipation rate is then

$$\epsilon = \frac{\epsilon_J}{F_U}, \quad (3.65)$$

where J is now the end point for the summation. The minimum resolvable dissipation rate that was possible with this spectral technique was $\approx 10^{-9}$ W kg $^{-1}$.

The second method for determining the dissipation rate is a spatial average

$$\epsilon = 7.5\nu \overline{\left(\frac{\partial u}{\partial z}\right)^2}, \quad (3.66)$$

which is outlined by Yamazaki and Lueck (1990). The method's greatest advantage is the high spatial resolution that is possible. While the dissipation rates estimated over a small scale are statistically uncertain, the log-normal nature of ϵ implies there may be severe underestimations but relatively small overestimations. The method's greatest disadvantage is a result of the variance being determined from all frequencies of the power density spectrum, including those which are dominated by noise. This leads to a high estimate of the dissipation when the dissipation rate is small ($\epsilon < 10^{-8}$ W kg $^{-1}$) because spectral components dominated by noise are included in the estimates. For moderate values of dissipation (10^{-8} W kg $^{-1} < \epsilon < 10^{-6}$ W kg $^{-1}$) the technique suffers little from the bias created by noise or from the limited frequency band (0.5–50 Hz) of the filtered shear signal.

When the dissipation rate is large ($\epsilon > 10^{-6}$ W kg $^{-1}$) less than 95% of the variance of microstructure shear is in the frequency band 0.5–50 Hz. Much of the spectrum of the shear is within the band where there is significant roll-off response due to the Osborn type shear probes. This produces a low estimate of the dissipation rate. Using the inverse of the correction proposed by Ninnis (1984) on Nasmyth's universal spectrum, the response of an Osborn type shear probe to a turbulence field with various dissipation rates was determined. Estimates of the variance of the microstructure

shear in the band 0–50 Hz from the modified universal spectrum were determined for the various dissipation rates. These variance estimates were then used to determine the underestimated dissipation rates that were due to the roll-off response of the shear probe and the filtering of the shear signal. An interpolation of the relationship between the true dissipation and the underestimated dissipation rates was then used to correct the measured dissipation. The minimum resolvable dissipation rate using the spatial averaging technique was approximately 3–4 times larger than was possible with the spectral technique; however the spatial scale of the dissipation rates was 20 times smaller by using the spatial averaging technique.

The estimate of dissipation rate can be broken down into 5 steps; 1) despiking of microstructure shear, 2) band pass filtering of shear, 3) spectral estimation and Ninnis correction, 4) spectral integration and 5) variance adjustment (extrapolation). The error in dissipation rate estimates is in general $\pm 50\%$ (Oakey 1982). The primary error sources are; the assumption of isotropy (Yamazaki 1990), the measurement of fall speed ($\approx 20\%$ error in ϵ), the calibration of shear probe ($\approx 10\%$ error in ϵ), the temperature dependence of shear probe sensitivity ($\approx 20\%$ error in ϵ) and the assumption of the spectral shape of the shear signal.

3.6 Length Scales and Decay Time of Turbulence

In the study of turbulence, a number of length scales have been derived. Some are related to the mean scale of overturns in turbulent patches. A common length scale that was developed through mixing-length models is the Ozmidov scale

$$l_0 = \left(\frac{\epsilon}{N^3} \right)^{1/2}, \quad (3.67)$$

where N is the buoyancy frequency, is proposed to be proportional to the height of the largest eddy that is unaffected by buoyancy in stratified, turbulent shear flow (Dillon 1982). A vertical scale of eddies l_T determined from high-resolution temperature signals was proposed by Thorpe (1977) to be proportional to l_0 .

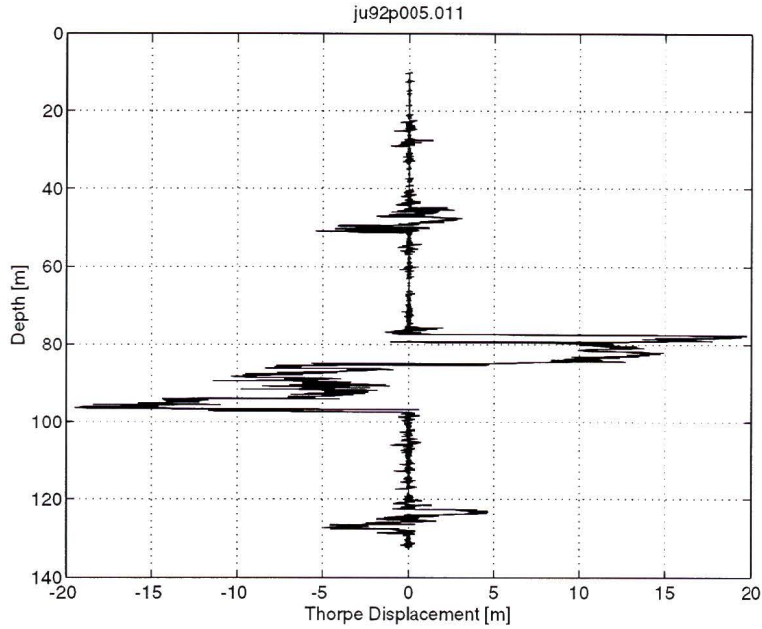


Figure 3.12: Thorpe displacement for a region of strong turbulence and no intrusions.

The Thorpe scale l_T is ideally determined from a density profile ρ_i . The density profile is sorted into a monotonic sequence ρ_n that represents a stably stratified water column. The distance each water parcel is moved, the Thorpe displacement, is

$$d_i = z_i - z_n, \quad (3.68)$$

where z_i and z_n are the depth of the corresponding ρ_i and ρ_n . The Thorpe scale is then defined as

$$l_T = \overline{(d_i^2)}^{1/2}, \quad (3.69)$$

where the overbar indicates an appropriate average. The choice of an appropriate average will be discussed in chapter 9.

The resolution of density measurements is generally insufficient to resolve Thorpe displacements. Only the largest overturns (> 10 m) can be resolved from the density records taken at Cobb. For smaller overturns, high resolution temperature signals must be used instead. This works only where there is a monotonic relationship between temperature and density. In regions of intrusions, l_T as determined from

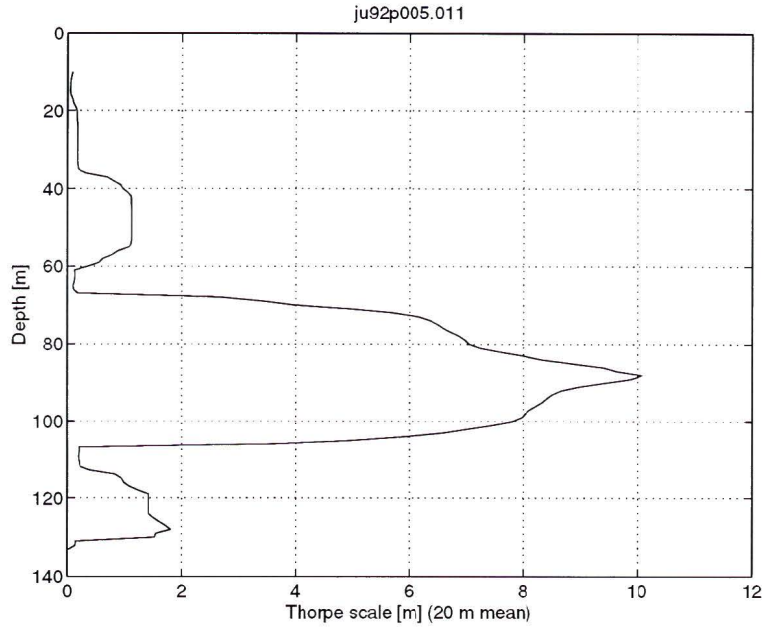


Figure 3.13: Thorpe scale for the same profile as Fig. 3.12, as determined by a 20 m running average.

the temperature record is overestimated. For my estimates of Thorpe displacement I found

$$d_n = z_i - z_n \quad (3.70)$$

was less noisy than (3.68). If there were no motions on any scale but the largest, then (3.68) and (3.70) are mirror images of each other. It is the small scale turbulence that causes the Thorpe displacement to be noisier in the reference frame of the turbulent unsorted temperature (3.68). Ideally, the Thorpe scales derived from (3.68) and (3.70) should be equivalent with appropriate averaging. When averaged over an entire disturbance, such as the one between 80 and 100 m in Fig. 3.12, the Thorpe scales are virtually identical.

By comparing the length scales l_0 and l_T , an estimate has been made for the decay time scale of turbulence (Crawford 1986). The Ozmidov scale is dependent upon the rate of dissipation while the Thorpe scale depends on the available potential energy (APE) of the water column. Assuming that the APE is related to the kinetic energy

KE of the turbulent patches as $\text{KE} = 3 \text{ APE}$, the decay time of turbulent kinetic energy is approximately

$$\tau_d = \frac{3\text{APE}}{\epsilon} = \frac{3N^2 \overline{d_i^2}}{2\epsilon} = \frac{1.5(l_0/l_T)^2}{N}. \quad (3.71)$$

This leads to a dimensionless time scale

$$\tau_c = \frac{\tau_d N}{2\pi}. \quad (3.72)$$

The ratio of the Ozmidov and Thorpe scales for the ocean range from 0.8 (Dillon 1982) to 0.66 ± 0.27 (Crawford 1986). The related dimensionless decay scales are 0.37 and 0.49 respectively. My calculations assume $\tau_c = 0.5$, giving perhaps an overestimated decay time; hence derivations completed later in this thesis of the distance turbulent patches can advect away from the source of turbulence before they decay to a background level or before they become undetectable may be overestimated. The overestimation is unimportant for my results.

Chapter 4

Background Observations

Cobb Seamount has been studied for answers to the biological and physical effects of a shallow seamount. Questions of biomass, biological productivity, mean currents, isopycnal doming and internal waves have been addressed by Dower (1994), Freeland (1994), and Eriksen and Codiga (*pers. comm.*). Was the high biomass and productivity at Cobb associated with some physical process of the mean currents and isopycnal doming? Were there other important physical processes that determined the biological and hydrographic conditions around Cobb?

4.1 Mean Circulation

From the mean current measurement, Freeland (1994) shows the presence of an anti-cyclonic Taylor cap over Cobb Seamount. Current meter moorings were deployed by Freeland during three summer cruises to Cobb (1990, 1991, 1992). All moorings had identical arrangements, with InterOcean current meters at 3, 10 and 50 m from the bottom. The current meters on the individual mooring were arranged to be in the bottom boundary layer, near the top of the bottom boundary layer and at mid-depths. All mean currents 50 m above the bottom follow isobaths. Progressive vector diagrams of the currents show rectilinear motion with only small reversal due to tides.

Shipboard ADCP surveys of Freeland (1994) during 1990 and 1992 show recirculation (closed streamlines) over Cobb. Anti-cyclonic motion begins at ≈ 80 m depth and complete recirculation is evident by 120 m. Hence, the Taylor cap extends to within 100 m of the surface. Dower (1994) has supporting evidence of isopycnal

doming but finds that the doming occurs 10–30 km away from the summit, on the leeward side. This does not correspond with Freeland’s observation of recirculation over the seamount. A hydrographic transect of Cobb by Eriksen and Codiga (*pers. comm.*) shows large scale variations due to internal waves and no obvious isopycnal doming. Only by comparing two ensemble averages of profiles over the seamount and off the seamount was isopycnal doming found. Hence, Dower’s observations over the seamount are probably aliased by internal waves, and true doming was not resolved.

Freeland (1994) indicates there is consistent counter-clockwise veering of the mean current at 3 m versus that at 50 m. This is attributed to a mean downslope Ekman pumping that is expected for an anti-cyclonic Taylor cap over the seamount. Freeland determined the radially outward flow to be approximately 3 cm s^{-1} , requiring a return flow at mid-depth of $0.2\text{--}0.4 \text{ cm s}^{-1}$. Some debate over the depth of the return flow has occurred: Greg Holloway (*pers. comm.*) has suggested that the return flow may occur below the Ekman layer and not above it. The flow would be up small canyons of the seamount where the canyons walls support the pressure gradient required for a geostrophically balanced flow. Holloway points out that if the return flow was above the Ekman layer and was geostrophically balanced, the mean pressure gradient around a horizontal circle centered at the seamount would be non-zero and the pressure would be multi-valued. He also cites the presence of a thin, cold, bottom mixed layer over the seamount (to be shown later). However, the mid-depth return flow need not be geostrophically balanced. The Coriolis forces perpendicular to the return flow decelerates the anti-cyclonic flow over the seamount by the process of spin-down (Garrett *et al.* 1993). Hence, there is no requirement of isopycnal tilting to balance the Coriolis forces. The presence of the cold bml may be easily explained by internal waves that are observed both in the current meter and CTD records. Holloway’s idea of return flow in thin, narrow layers below the Ekman layer requires certain conditions

of the flow that would be difficult to satisfy. This canyon flow returns through a cross-sectional area that is much smaller than that of the Ekman layer but the volume flux in both must be identical. Therefore, the speed of the return flow must be larger than the flow in the Ekman layer. I estimate that the canyon flow would have to be greater than 30 cm s^{-1} . The canyon flow goes upslope, thereby working against gravitational forces. To generate the fast canyon flow against gravitational forces requires a large pressure gradient but there is no obvious source for this pressure gradient. A mid-depth return flow is 100 times slower and can follow isopycnals, thereby requiring a smaller pressure gradient.

Two satellite-tracked drogued-drifters were deployed over Cobb during the 1990 and 1992 cruises by Freeland (1994). They indicated the mean current in the region of Cobb is $10\text{-}12 \text{ cm s}^{-1}$. During the 1990 and 1992 cruises the current was in eastward and south-eastward directions respectively.

4.2 Internal Waves

The current meters deployed during the 1992 cruise show an energetic internal wave field. The moorings were deployed in a line east of the pinnacle. Moorings M1, M2 and M3 were placed over the flat top of the seamount, near the rim of the seamount and on the flank of the seamount. They were anchored at the 153, 200, and 350 m isobaths. Freeland (*pers. comm.*) indicates that the kinetic energy of the internal wave field is greatest near the bottom of mooring M2 (Table 4.3). The energy of the internal

Height	M1	M2	M3
50 m	51.2	50.8	35.8
10 m	63.1	113.9	13.8
3 m	50.6	101.7	13.6

Table 4.3: Fluctuation kinetic energies of currents with periods less than 20 hours for the 1992 cruise (Freeland *pers. comm.*). The values are in $\text{cm}^2 \text{ s}^{-2}$.

waves below the rim (M3) takes a maximum at the 50 m current meter. I propose

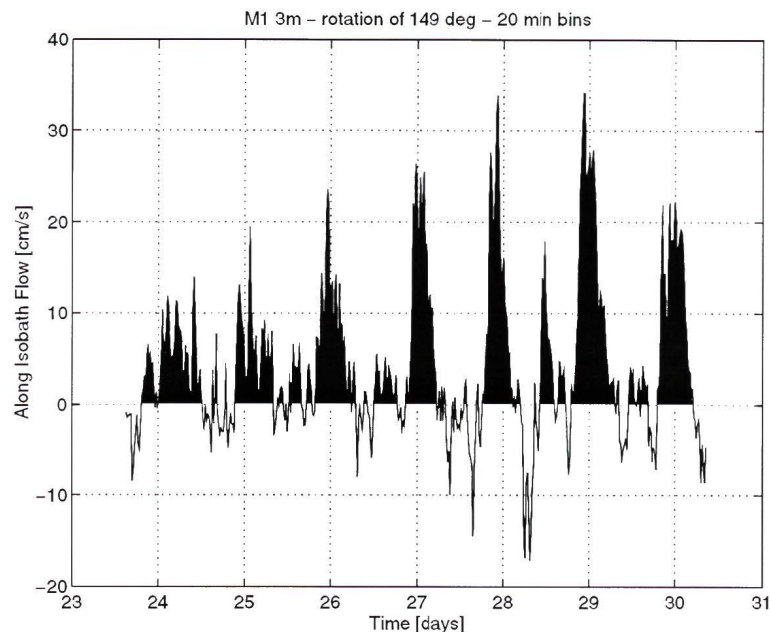


Figure 4.14: Along isobath flow on the flat top of Cobb, 3 m above the bottom. The filled curve is for flow to the SE. The series began June 23, 1992 at 14:59.

that this is the result of internal waves from the rim traveling radially outwards with a slight downward inclination. Freeland also notes the spectra of the 3 m current meter on M2 has large deviations from the Garrett-Munk (GM) spectrum, showing increased energy in the internal wave field, especially at the semi-diurnal internal tidal frequency. Hence, Freeland concludes that there is significant amplification of internal waves near the rim of Cobb. Dower (1994), from two time series of isopycnals, one on the eastern side of Cobb and the other 25 km north of the seamount, found internal waves were more energetic near the seamount.

My examination of the data collected by Freeland gives a clue to the structure of the bottom boundary layer at Cobb. Currents are shown from the 3 m high current meter from mooring M1. It was positioned on the flat top of the seamount, 2 km east of the pinnacle. The along-isobath flow (Fig. 4.14) has strong diurnal and semi-diurnal components but shows little reversal. Freeland found the semi-diurnal component of flow is more energetic at 3 m than at 50 m, showing the presence of an energetic internal wave with a near semi-diurnal period. The cross-isobath (Fig. 4.15)

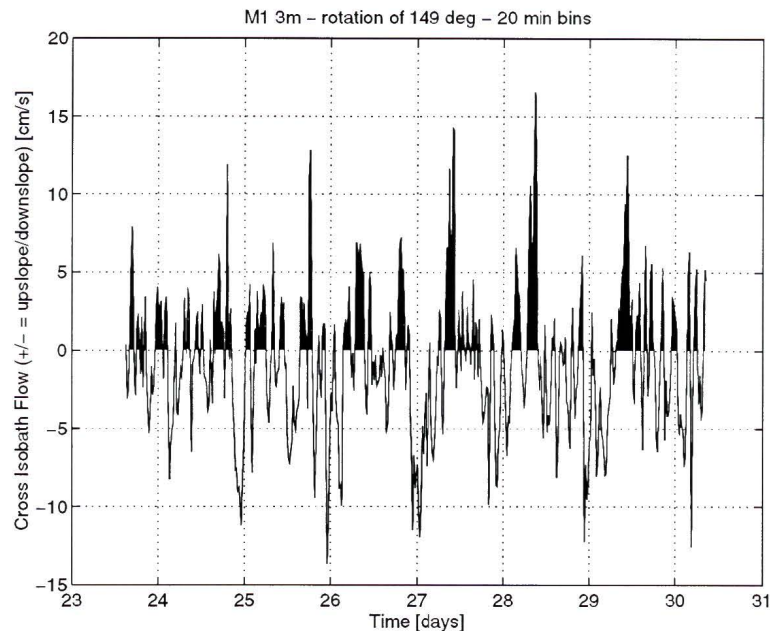


Figure 4.15: Cross isobath flow on the flat top of Cobb, 3 m above the bottom. The filled curve is for flow upslope. The series began June 23, 1992 at 14:59.

is dominated by flows occurring at periods of a few hours and not by the diurnal and semi-diurnal components. The flow implies there may be a strong dependence of vertical motion along the boundary on high frequency internal waves.

The temperature gradient in the bottom boundary layer as determined from Freeland's data shows variations in the bottom mixed layer at both tidal and higher frequencies (Fig. 4.16). The normalized temperature gradient is the temperature difference between the current meters at 10 m and 3 m on M1 divided by 7 m and by the average temperature gradient from the far field of transect 1 at approximately the same isotherm as sampled by the current meters. The normalized temperature gradient correlates well with the diurnal component of the along isobath flow. A stronger flow produces a smaller temperature gradient and thereby a thicker bml. This is related to the stronger flow generating more turbulent mixing and downslope Ekman flow, both create thicker bottom mixed layers. The temperature gradient, when the diurnal component of the along isobath flow is small, becomes quite high

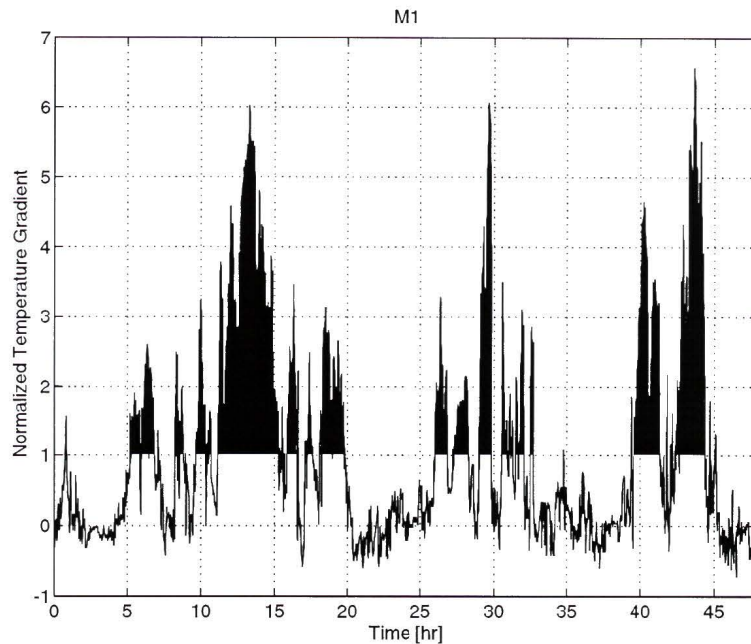


Figure 4.16: A time series of vertical temperature gradient, as determined from the bottom two current meters of M1, that is normalized by the far field temperature gradient. The filled curve is for gradients larger than the norm. The time series is from June 28–29, 1992.

(over 6 times above the far field value). Short period variations are perhaps the result of internal waves. The stratification in one case goes from 6 times far field value to no stratification in less than an hour. Based on the above, the diurnal tide and higher frequency flows dominate the mean flow in determining bbl structure. Profiles in the bottom boundary layer that show rapid variations in bml height with times of extremely high temperature gradient can therefore be expected.

4.3 Biological Implications of Cobb Seamount

Dower (1994) has found high concentrations of both phytoplankton and zooplankton over the seamount. He finds that high phytoplankton concentrations are due to the effects of phytoplankton uplift by doming of isopycnals over the seamount as the phytoplankton are advected by the mean current; thus bringing the phytoplankton into a shallower depths with improved light conditions. The high zooplankton

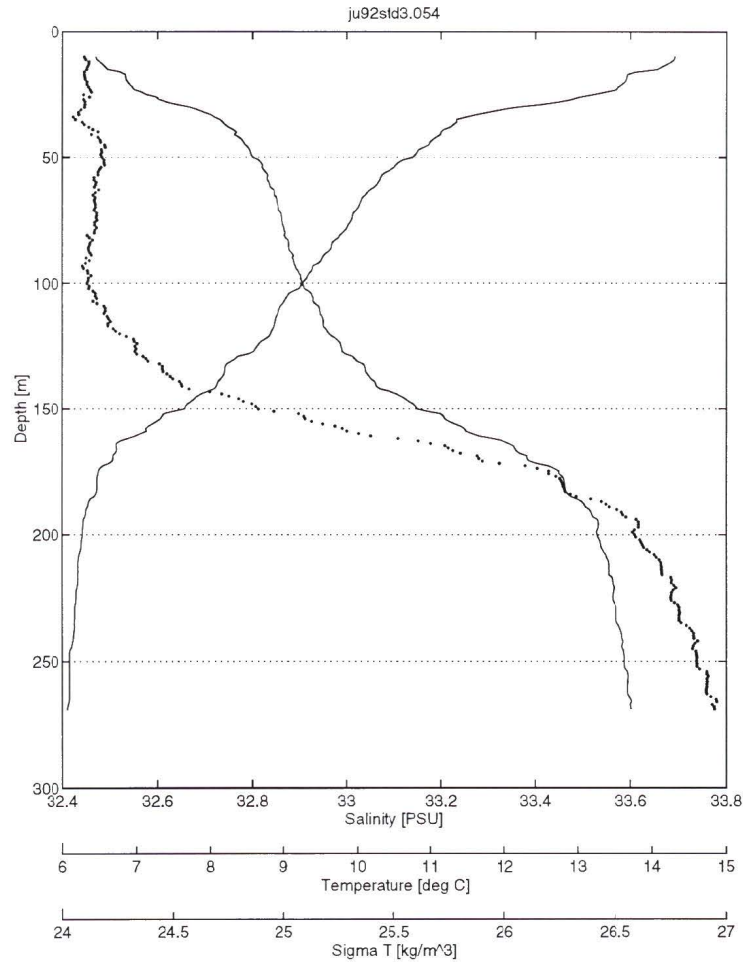


Figure 4.17: Salinity (dots), temperature (decreasing with depth), and density (increasing with depth) for one profile from the eastern flank of the seamount. All parameters are averaged into 1 m bins.

concentrations are the result of the high phytoplankton productivity.

4.4 CTD Results

The typical structure of the water column around Cobb during the cruise can be seen from one of the profiles taken off the seamount's eastern flank by FLY II (Fig. 4.17). Between 0 and 50 m is the seasonal pycnocline and between 100 and 200 m is the permanent pycnocline (Fig. 4.18). Above 100 m the water is relatively isohaline in comparison to the rest of the profile. There were no strong wind events during the cruise; therefore the structure of the water column stayed relatively constant for all

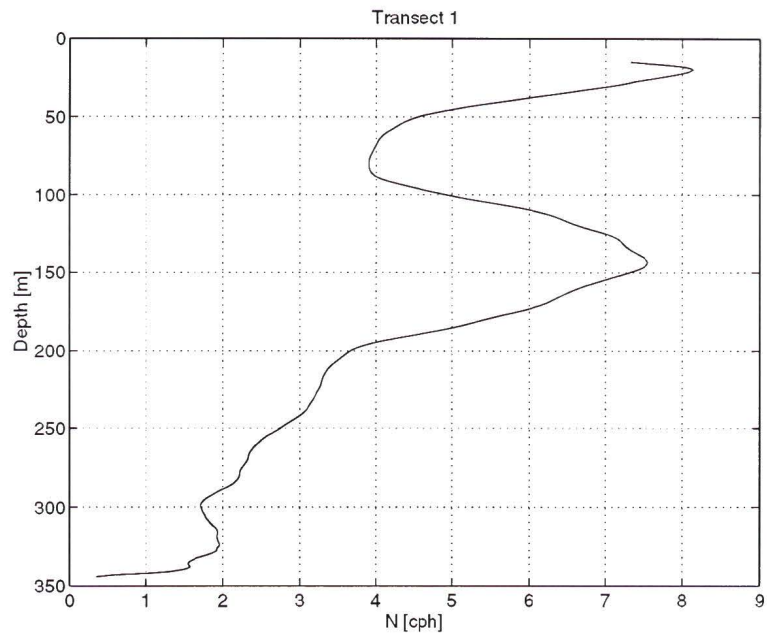


Figure 4.18: The far field buoyancy frequency, N , as determined from an average of the last 20 profiles from the first transect and a 20 m running average.

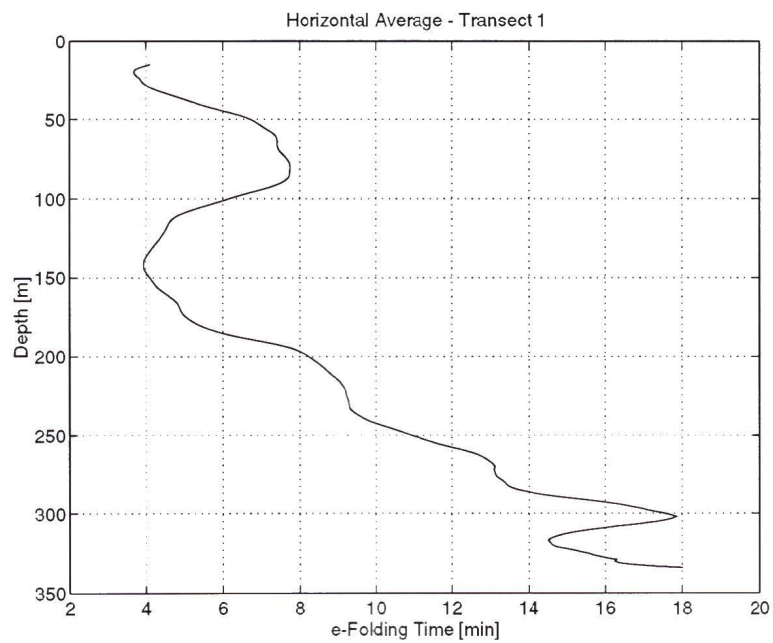


Figure 4.19: The e-folding time, τ_c , as determined from the N in Fig. 4.18.

profiles.

The decay time scale of turbulence is dependent upon the buoyancy frequency. Taking τ_c as given in (3.72) equal to 0.5, the e-folding time scale τ_d will probably be overestimated. The e-folding time scale ranges from a minimum of 4 minutes to a maximum of 18 minutes for the cruise (Fig. 4.19). For example, if a patch were to be advected by the mean current of 10 cm s^{-1} over a distance of 1 km, then the turbulent patch would e-fold between 9 to 42 times depending on the depth of the patch. This implies that turbulent patches advect a short distance ($< 1 \text{ km}$) from where they were generated before decaying to a background level.

Chapter 5

Transects

During the 1992 cruise we performed two transects of the seamount with the microstructure instrument FLY II. These allow us to address a number of questions:

- Do isopycnals dome over the seamount?
- Is turbulence around Cobb primarily generated by the mean flow or internal waves?
- Is there enhanced turbulence associated with the rim of the seamount where enhanced internal wave energy was observed by Freeland?
- Is there enhanced mixing at Cobb and how significant is it?

5.1 Isopycnal Surfaces

Isopycnal doming is not evident in either of the transects (figures 5.20 and 5.21). The complete lack of a large scale trend in the isopycnals is the most prominent feature of both plots. From transect 1 the 24.8 kg m^{-3} isopycnal at the depth of 50 m has no mean change in height from near the pinnacle to over 13 km away. The 25.0 kg m^{-3} isopycnal is lowest near the seamount, while the 26.5 kg m^{-3} isopycnal rises near the seamount up to 30 m over its far field depth. In the second transect, isopycnals above 50 m all dome over the pinnacle, but this is a very small scale effect, less than 1 km horizontally from the pinnacle.

The lack of obvious large scale trends is due to the dominance of internal waves. Motions near the bottom, especially near the pinnacle, have a very small horizontal

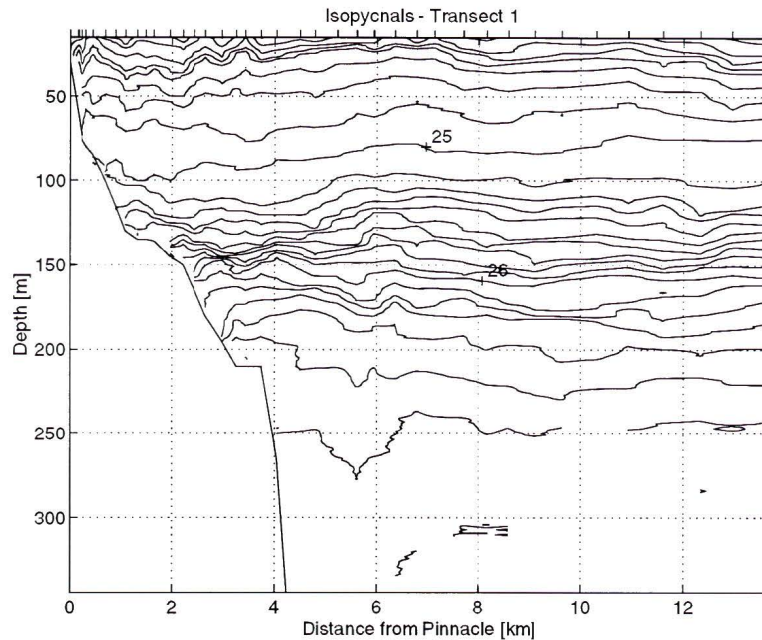


Figure 5.20: Constant σ_T surfaces for the first transect. The ticks on the upper x-axis indicate profile positions. The isopycnals are set 0.1 kg m^{-3} apart, with isopycnals of 25 and 26 kg m^{-3} marked. The bottom depth is indicated by the solid line at the left of the plot.

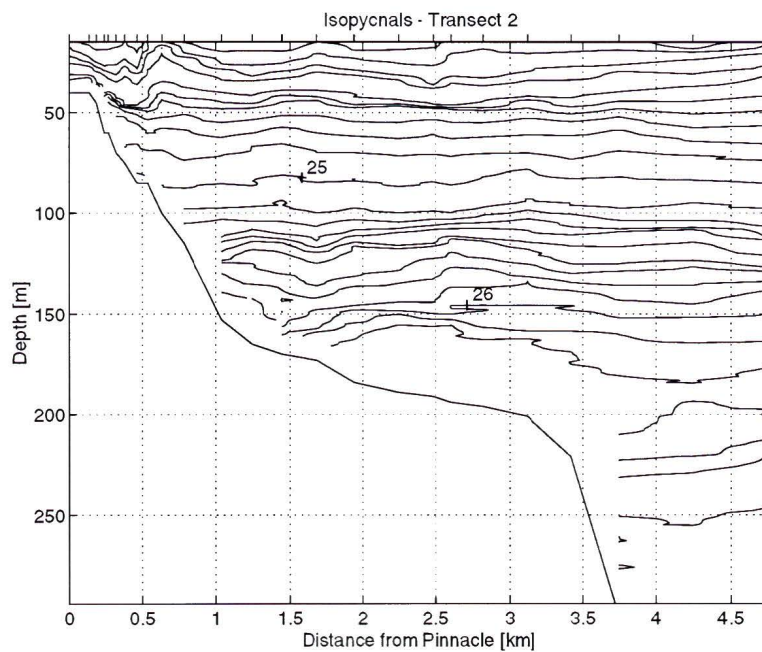


Figure 5.21: Constant σ_T surfaces for the second transect. The ticks on the upper x-axis indicates profile positions. The isopycnals are set 0.1 kg m^{-3} apart, with isopycnals of 25 and 26 kg m^{-3} marked.

scale (< 1 km) but they correspond to vertical displacements of isopycnals of over 20 m. Motions away from the pinnacle are on a larger horizontal scale (1–4 km), with some vertical displacements over 15 m. In the far field there is little isopycnal motion. Without proper time averages of density profiles over the seamount internal wave motions will bias large scale isopycnal displacements that are the result of circulation over the seamount. The time averages would have to be equal to or greater than 12.5 hours to remove the effect of the strong semi-diurnal internal wave signal observed by Freeland (*pers. comm.*).

The effects of internal waves on isopycnals within the bbl and the structure of the bml, are extraordinary. There is a complete lack of a consistent structure for the entire bml. In transect 1 isopycnals 24.9 and 26.3 kg m^{-3} show a local decrease in the density of the bbl relative to the far field, while isopycnals 25.1 and 26.5 kg m^{-3} show local increases in density. Some areas of the bbl have isopycnal spreading with surrounding regions of convergent isopycnals. Some examples are at 110, 150 and 180 m. These correspond to areas of thick bml surrounded by areas of thin bml. High frequency internal waves during a time of small along-isobath flow are likely sources of this structure. Transect 2 shows a similar effect of internal waves in the bbl.

These transects are not snap shots of the isopycnals as the measurements were not synoptic. The time for the completion was 7 hours for the first transect and 3 hours for the second. Given the low period internal waves observed in the current meter measurements and isopycnal motions by Dower (1994), we are unable to differentiate between temporal and spatial variability in the isopycnals. This issue is also confused by the lack of dependence of wavelength and group speed on the frequency of internal waves. The wavelength we observe may be the result of an internal wave of any frequency.

5.2 Dissipation Rate Transects

The seamount is a source of enhanced dissipation (figures 5.22 and 5.23). Some patches near the seamount have dissipation rates more than three orders of magnitude larger than the far field; however the maxima in ϵ are not at the bottom but are 10's to 100's of meters vertically and 100's to 1000's of meters horizontally from the bottom.

In transect 1 there are two prominent layers of enhanced turbulence. The shallowest of the enhanced dissipation layers is centered at 150 m and is approximately 100 m thick. It becomes distinct from bottom enhanced turbulence at 5 km from the pinnacle and becomes indistinct from background turbulence at 12 km from the pinnacle. The dissipation rates in this feature are only an order of magnitude larger than far field results. Interestingly, the layer is at the same depth as the permanent pycnocline. The source of this enhanced dissipation layer is most likely internal waves. Within the permanent pycnocline the e-folding time scale of turbulence is approximately 5 minutes. Given the mean current observed by the drogued drifters, the e-folding length scale is only 30 m; therefore the source for this enhanced dissipation has to be local, within a few 10's of meters of where the observations took place. The enhanced turbulence cannot be the result of turbulent patches that are generated at the bottom of the seamount by shear in the mean flow and advected the many kilometers to where enhanced dissipation is observed. High frequency, 4–7 cph, internal waves can exist only in the seasonal and permanent pycnocline. These internal waves will be trapped within the pycnocline and will not form the characteristic sloping ray path of internal waves in a slowly and monotonically varying, stratified fluid. Internal waves of lower frequencies are refracted within the pycnocline, bringing ray paths closer together and increasing the energy density thereby increasing the likelihood of internal wave breaking. Therefore, the layer is likely generated by internal waves that originate from the seamount and are trapped or refracted within the pycnocline.

The deeper layer begins at the rim and extends horizontally 4 km and down 50 m.

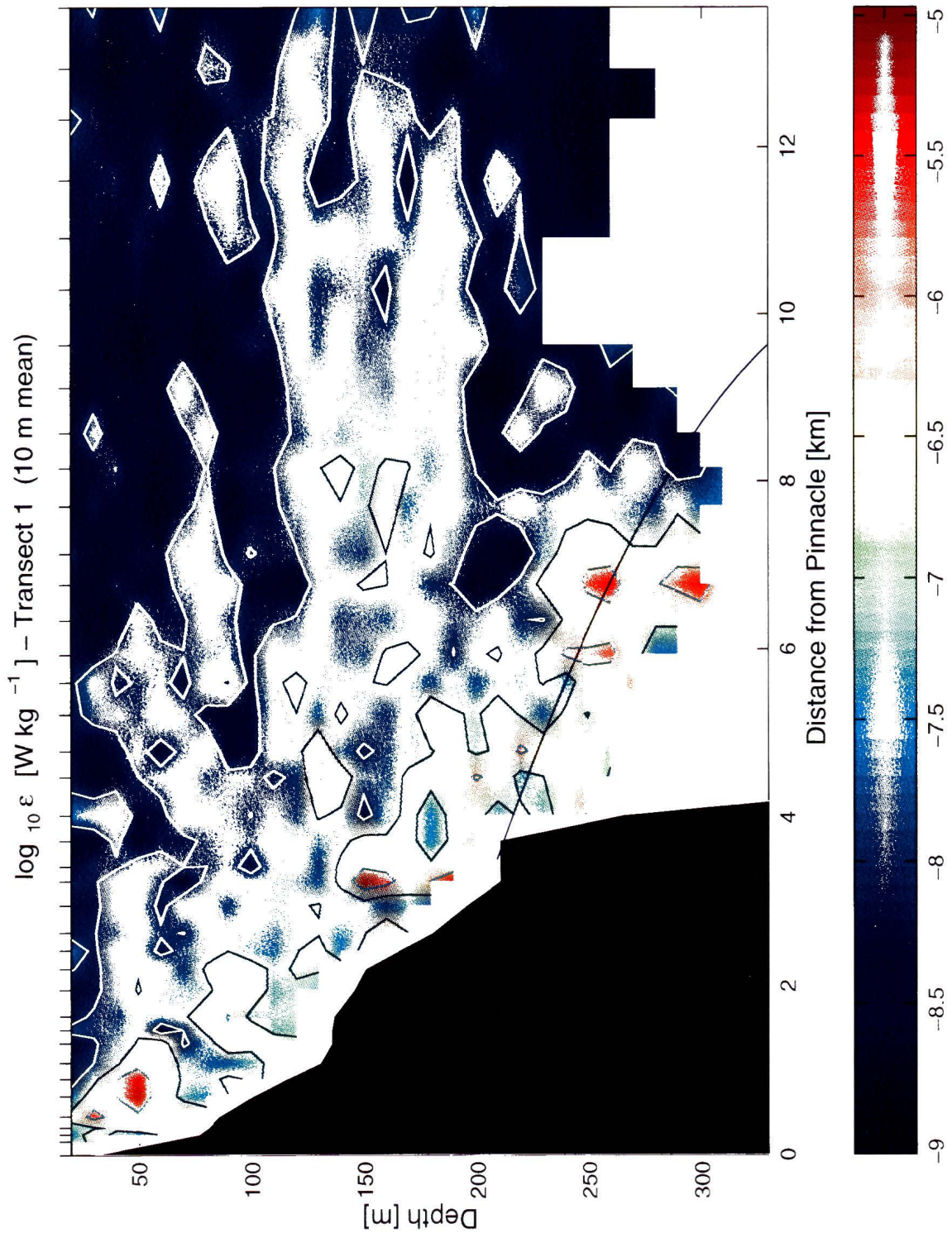


Figure 5.22: $\log_{10} \epsilon$ for transect 1. Contours for $\epsilon = 10^{-6}, 10^{-7}$ and $10^{-8} \text{ W kg}^{-1}$ are plotted. ϵ has been averaged into 10 m bins. The solid line that begins at the rim and extends to ≈ 10 km from the pinnacle is the ray path for a semi-diurnal internal wave derived by Kevin Lamb (*pers. comm.*), assuming no mean current.

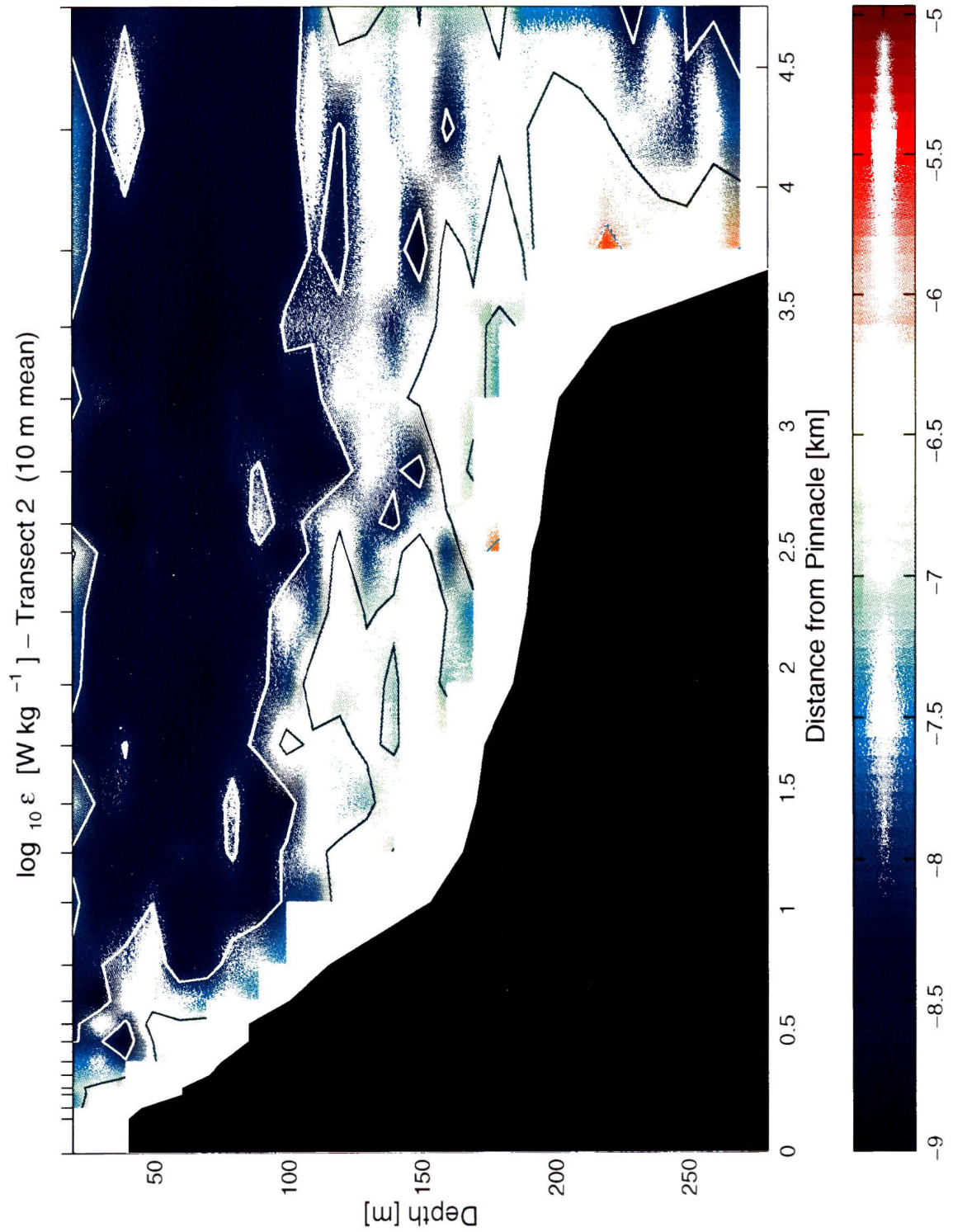


Figure 5.23: $\log_{10} \epsilon$ for transect 2. Contours for $\epsilon = 10^{-6}, 10^{-7}$ and $10^{-8} \text{ W kg}^{-1}$ are plotted. ϵ has been averaged into 10 m bins.

Its thickness is at least 50 m but may be significantly more because the profiles were not deep enough to observe the bottom of the layer. The dissipation rates in the layer are over a magnitude larger than those in the layer at 150 m. The maxima of 10^{-6} W kg⁻¹ are 3 km southeast of and 1 km above the seamount. As with the shallower layer, the source of the enhanced dissipation is internal waves. The e-folding time scale of turbulence at the depth of the layer is 12 minutes, with a corresponding length scale of 70 m. If the patches of maximum dissipation in the layer were generated at the seamount and advected the required 3 km, the patches would have e-folded over 40 times. The original patch would have had a dissipation rate of 10^{12} W kg⁻¹! Only a couple of kilograms of water with such a high dissipation rate are required to supply the 1.9×10^{12} W of energy dissipated by the secular deceleration of the Moon - Ocean - Earth system (Dewey 1987). If we assume a heat capacity of the water to be approximately that of pure water at one atmosphere then the original patch would increase its temperature by 1 °C every 4 μ s, causing all of the boundary layer to quickly boil away.

The lower layer follows the ray path of a semi-diurnal internal wave originating from the rim of the seamount. The ray path was calculated by Kevin Lamb (*pers. comm.*) using the average N profile in Fig. 4.18 and by assuming no mean current. The magnitude of the group velocity of the wave is dependent on wavelength but is independent of frequency. Therefore, the mean flow of 10 cm s⁻¹ to the south-east will tend to reduce the slope of the ray path.

It has also been assumed that the internal wave is radiating radially outward. The azimuth of the incident and reflected internal waves need not be zero; however the smallest slope of a reflected wave that could have been observed by the transect would be a wave whose horizontal ray path was parallel to the transect and orthogonal to the isobaths. This implies that the top of the layer may be well defined but the bottom is not and it may not be parallel to the top. The semi-diurnal internal tide

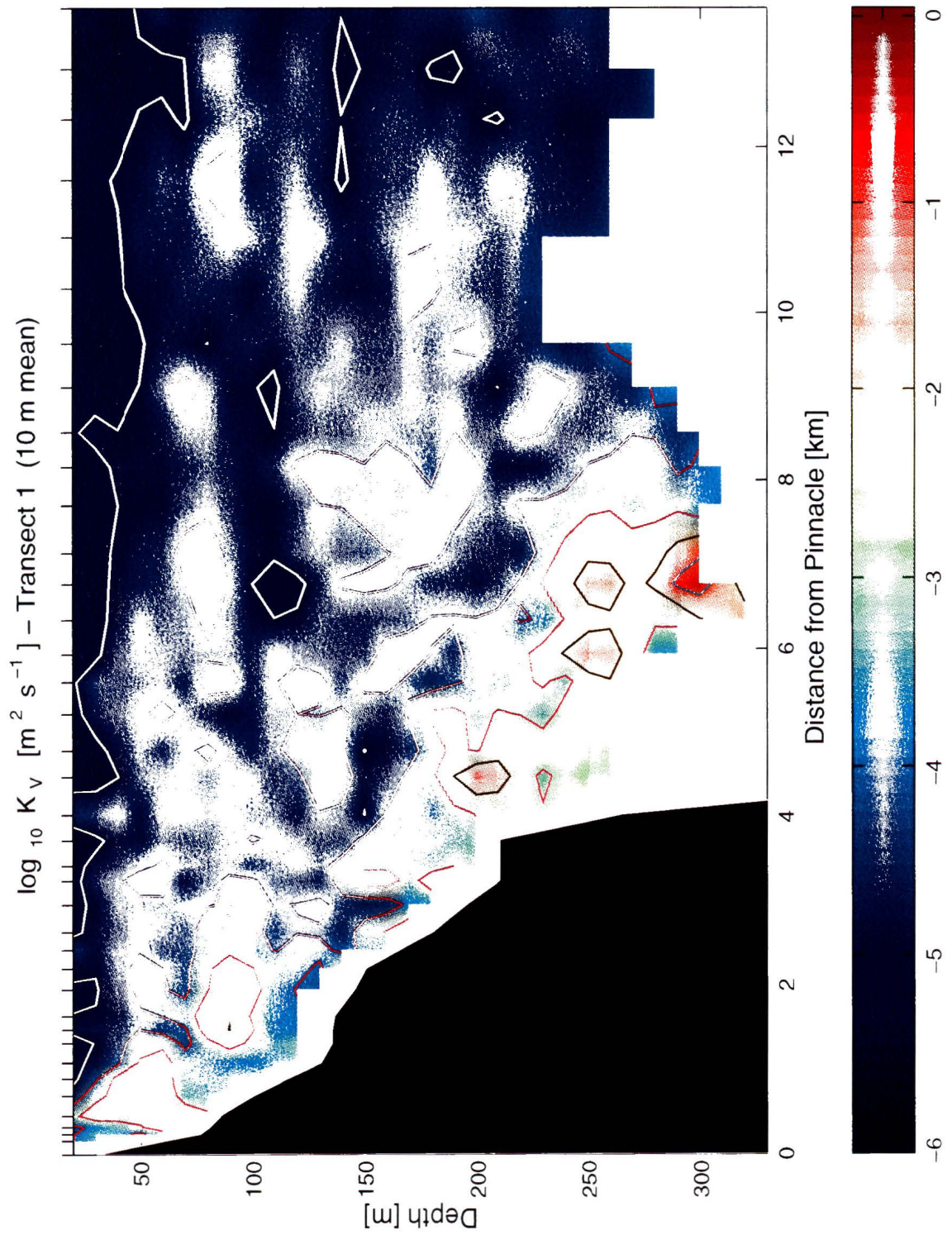


Figure 5.24: $\log_{10} K_v$ for transect 1. Contours for $K_v = 10^{-1}, 10^{-2}, 10^{-3}, 10^{-4}$ and $10^{-5} \text{ m}^2 \text{ s}^{-1}$ are plotted. K_v has been averaged into 10 m bins.

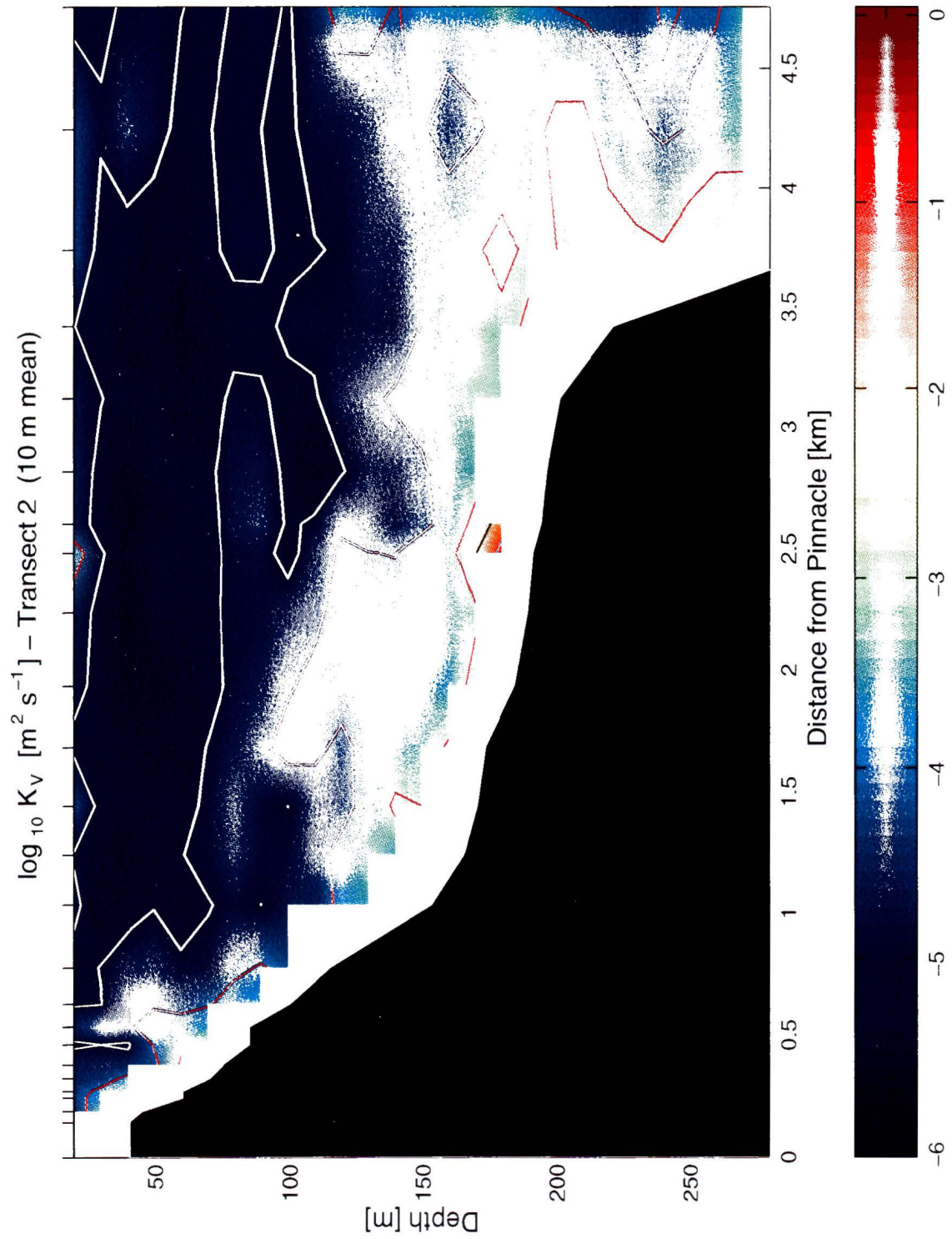
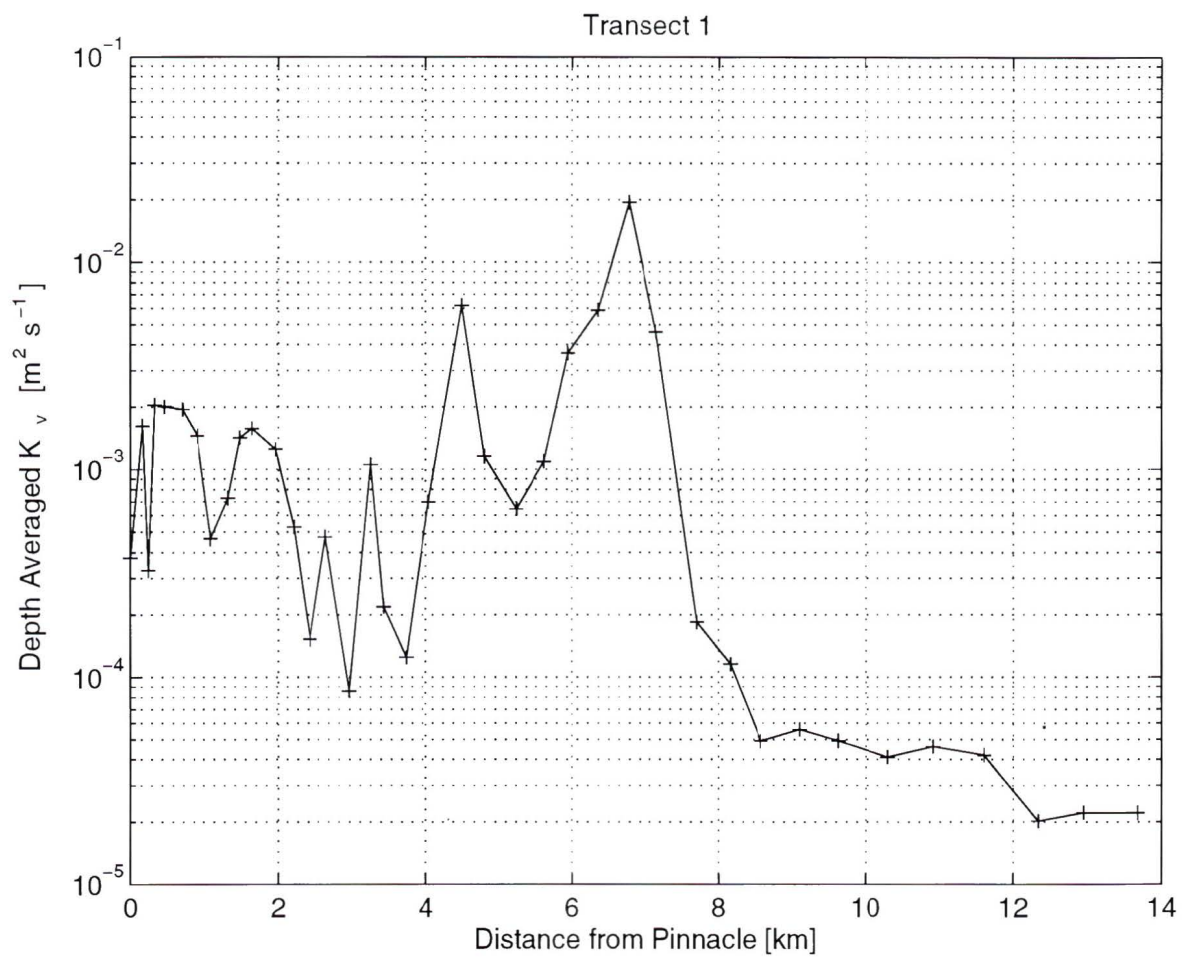


Figure 5.25: $\log_{10} K_v$ for transect 2. Contours for $K_v = 10^{-2}, 10^{-3}, 10^{-4}$ and $10^{-5} \text{ m}^2 \text{ s}^{-1}$ are plotted. K_v has been averaged into 10 m bins.

Figure 5.26: Depth averaged K_v for transect 1.

5.4 Mixing Transect

The total amount of mixing performed by the seamount can be estimated from the first transect. The density flux from (2.16) is

$$\langle \rho' w \rangle = \frac{\Gamma \epsilon \rho}{g}, \quad (5.73)$$

where the overbar has been replaced by $\langle \rangle$. Integrating (5.73) produces a mass flux

$$F_{Mass} = \int \langle \rho' w \rangle dA = \sum_i \langle \rho' w \rangle_i A_i, \quad (5.74)$$

where the sum is over every profile i , and A_i is the circumferential area of each profile i , namely

$$A_i = 2\pi r_i \Delta r_i, \quad (5.75)$$

where r_i is the distance of the profile from the pinnacle, and Δr_i is the width of the ring within which each profile is centered. Dividing the mass flux near the seamount (5.74) by the density flux in the open ocean

$$A_o = \frac{\sum_i \langle \rho' w \rangle_i A_i}{\langle \rho' w \rangle_o}, \quad (5.76)$$

provides a way to determine A_o , the area of the open ocean that does an equivalent amount of mixing as the waters around Cobb. $\langle \rho' w \rangle_o$ is the density flux in the open ocean as determined by

$$\langle \rho' w \rangle_o = \frac{K_v \rho N^2}{g}, \quad (5.77)$$

where $K_v = 10^{-5} \text{ m}^2 \text{ s}^{-1}$ is taken from the results of Ledwell *et al.* (1993) for the mid-Atlantic at a depth of about 300 m and N is from an average of the last 20 profiles in transect 1. The assumption that K_v is independent or is at least slowly varying with depth is reasonable for the open ocean. Vertical diffusivities in the far field of transect 1 are depth independent (Fig. 5.24). Lueck *et al.* (1983) found that, west of Vancouver Island, vertical diffusivities ranged from $0.4\text{--}2.1 \times 10^{-5} \text{ m}^2 \text{ s}^{-1}$ over the depth range 25–1125 m. Observations 20–40 km from Fieberling Guyot (Polzin

et al. 1994), show $K_v = 0.69$ to $1.60 \times 10^{-5} \text{ m}^2 \text{ s}^{-1}$ over the depth range 100–3000 m, with no depth dependence.

The resulting profile of A_o (Fig. 5.27) shows that the mixing at Cobb is equivalent to as much as 100,000 km² of open ocean mixing at depths between 250–300 m. At most depths the area is less than this and is closer to 10,000 km². If we consider the local region around Cobb (Fig. 5.28), within the 100,000 km² box centered on Cobb there are at least 4 other *large* seamounts and a number of smaller seamounts; within the 10,000 km² there are two large seamounts. By comparing these boxes to local geography a better picture of the large region that must be affected by mixing at Cobb may be obtained

The larger value of 100,000 km² implies that Cobb mixes the equivalent of about 0.06% of the open ocean portion of the Pacific, or about 0.12% for the Atlantic. Smith and Jordan (1988) approximate that the number of seamounts in the Pacific is 30,000. If each seamount was as effective as the maximum mixing at Cobb, then seamounts would produce 18 times more mixing than what occurs in the open Pacific Ocean. This would readily provide the order of magnitude increase in diffusivities required to explain the difference in diffusivities observed in the open ocean versus what is required by ocean models. If we assume instead that each seamount only mixes the equivalent of 10,000 km², then seamounts still produce ≈ 1.8 times the mixing that occurs in the open ocean.

5.5 Discussion

No isopycnal doming that could be associated to a Taylor cap was observed at Cobb Seamount. Internal wave driven isopycnal motions appear to dominate any tilting that may be due to the mean geostrophic current. The effects of a Taylor cap might be observed by averaging profiles taken over at least 12.5 hours to remove the internal semi-diurnal tide signal, or over 16.4 hours to remove all internal wave signals. The

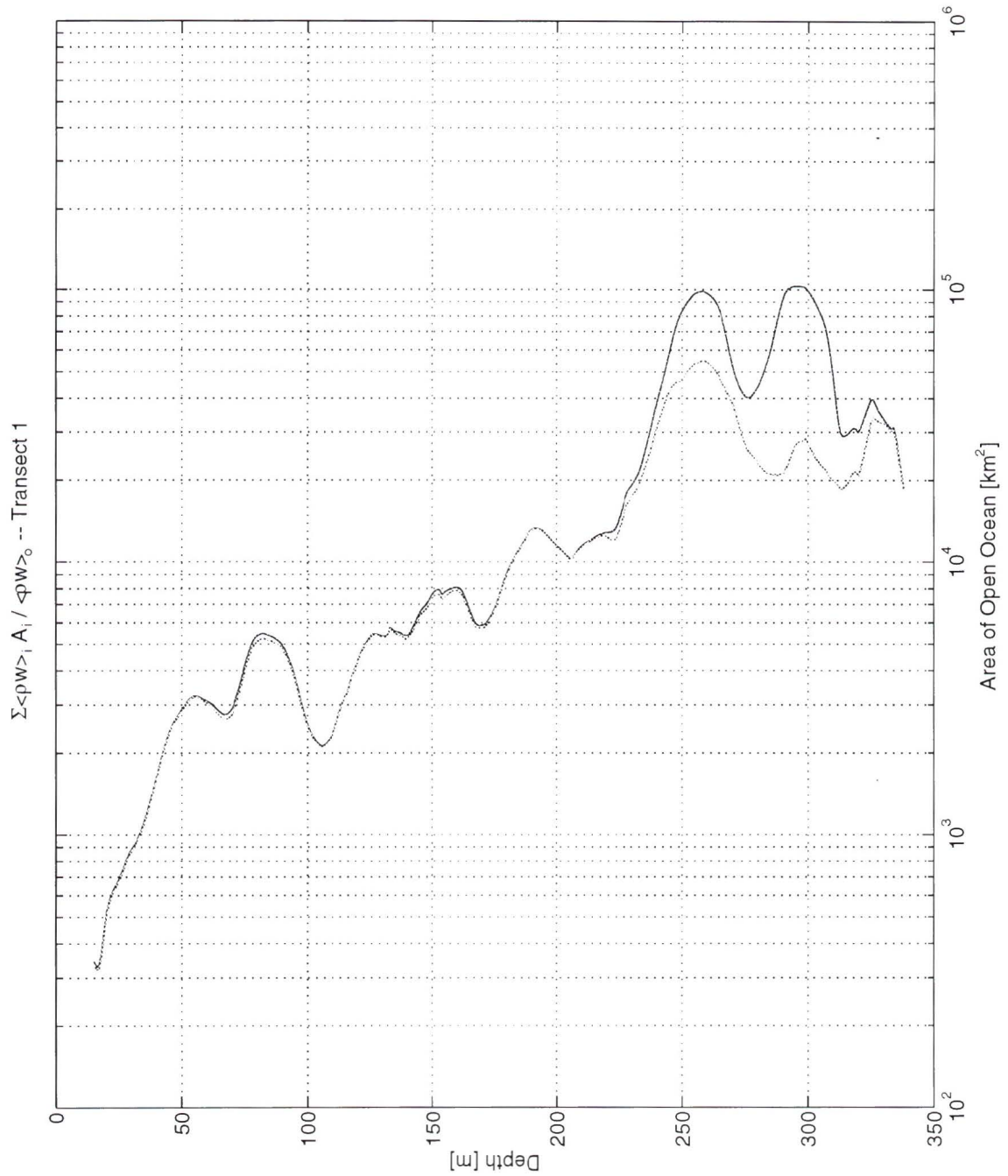


Figure 5.27: Area of open ocean equivalent to the observed mixing in transect 1. The solid line includes all profiles in its mass flux summation, while the dotted line has had the profile with the largest density flux removed when determining the mass flux.

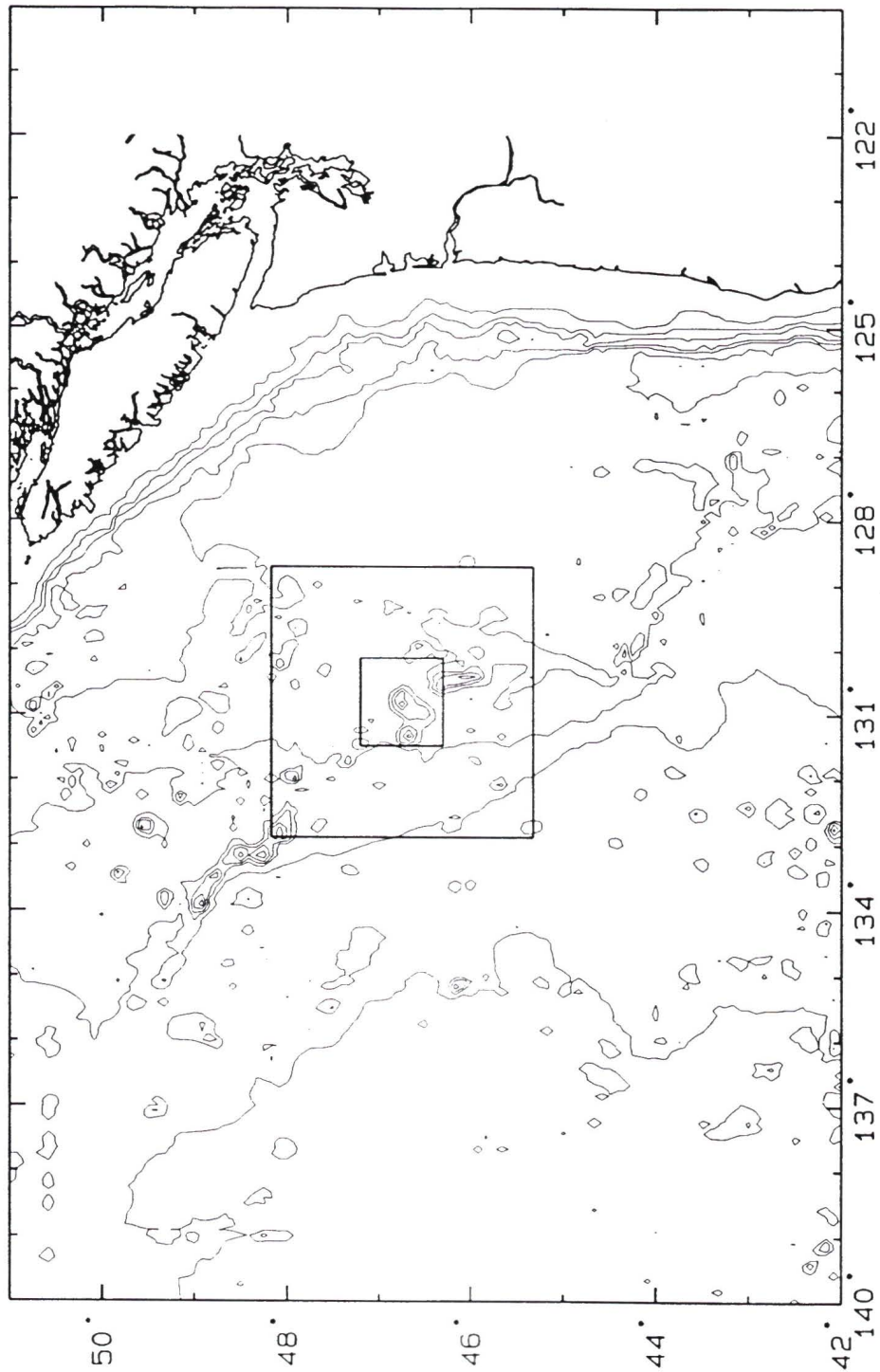


Figure 5.28: The northeast Pacific of the region surrounding Cobb Seamount. Contours are at 500 m intervals beginning at 500 m and ending at 4000 m. Cobb Seamount is centered in the two boxes plotted. The boxes have an area of 10,000 and 100,000 km².

doming observed by Dower (1994) off the seamount may simply have been the result of internal waves and have nothing to do with a Taylor cap or standing vortices. While the isopycnals show that internal waves are energetic around the seamount, it is not obvious whether the rim region is more significant than other areas.

Enhanced turbulence is found further away from the bottom than the typical 10's of meters for a turbulent bottom boundary layer that is generated by a mean flow. High values of dissipation rate are found 100's to 1000's of meter from the bottom. The only likely source for the turbulence is internal waves that originate from the seamount. The most significant portion of the internal wave field appears to be the semi-diurnal internal tide. The most significant mixing at the seamount occurs where the internal tide that originating from the rim, where the minimum slope is nearly critical, is transmitted. The total mixing done by the seamount in the depth range 150–350 m is equivalent to mixing in $1-10 \times 10^4 \text{ km}^2$ of the open ocean.

The effect of mixing at Cobb appears, by our estimates, to be important on a basin scale but may also have significant impacts on a local scale. The mixing may help to support the large biomass around Cobb. The high diffusivities around the seamount, plus the periodic upslope flow, should bring nutrient rich water up to a depth where phytoplankton can exploit it. This may insure that phytoplankton growth is not nutrient limited over Cobb.

The mixing at Cobb may be either overestimated or underestimated for a number of reasons. The dotted line in Fig. 5.27 is an estimate of mixing when the profile with the largest values of density flux is removed. This has reduced the area of open ocean by $\frac{1}{2}-\frac{1}{5}$ of the original value at some depths. This shows the large degree of statistical uncertainty in our estimate. The assumption of cylindrical symmetry could be significantly incorrect. No profiles were taken on the northern and western flanks of the seamount and the limited extent of the second transect does not allow it to confirm or reject the presence of an enhanced ϵ and K_v layer off the rim; however,

the 19 hour time series, that will be shown later, does show a similar layer off the eastern flank of the seamount. The 19 hour time series will also show the turbulence to be persistent for the length of the series but there may be significant longer term variability. Only a few profiles in went below 300 m and none below 350 m during the cruise. Profiles that did not go below 300 m make no contribution to the mass flux estimate, and this produces an underestimate of the mixing between 300–350 m. Below 350 m we have no knowledge of the mixing. This is especially important considering the circumference of the seamount is greater with depth. The area of the enhanced mixing ring could be over 4 times larger near the base of the seamount with a similar increase in the mixing at this depth. With all of these possible sources of errors, many that are not completely understood, it is not possible to place error bars on the estimate of mixing occurring around Cobb.

Chapter 6

Time Series

Two time series were completed with the FLY II. The longest, the 19 hour time series, was performed over the eastern flank of Cobb. The other, the CTD time series, was over the flat top, south of the pinnacle. The time series allow us to address some questions:

- Do isopycnals show strong internal wave signals?
- Are there depth variations in enhanced turbulence, and might they give clues to the source?
- Is there an enhanced dissipation layer similar to the lower layer in transect 1 over the eastern flank of the seamount?
- Is enhanced turbulence persistent?

6.1 Isopycnal Surfaces

The isopycnals from the 19 hour and CTD time series show the effects of internal waves of many different frequencies (Fig. 6.29 and 6.30). The sampling time of the 19 hour time series was rapid enough that we might expect to observe fluctuations of the isopycnals that happen with a period of 25 minutes or greater. For the CTD time series the lowest resolvable period is 80 minutes.

The isopycnal surfaces of the 19 hour time series have various periodic motions (Fig. 6.29). Throughout the permanent pycnocline, but particularly at the top of the pycnocline, there is a semi-diurnal isopycnal displacement of greater than 20 m.

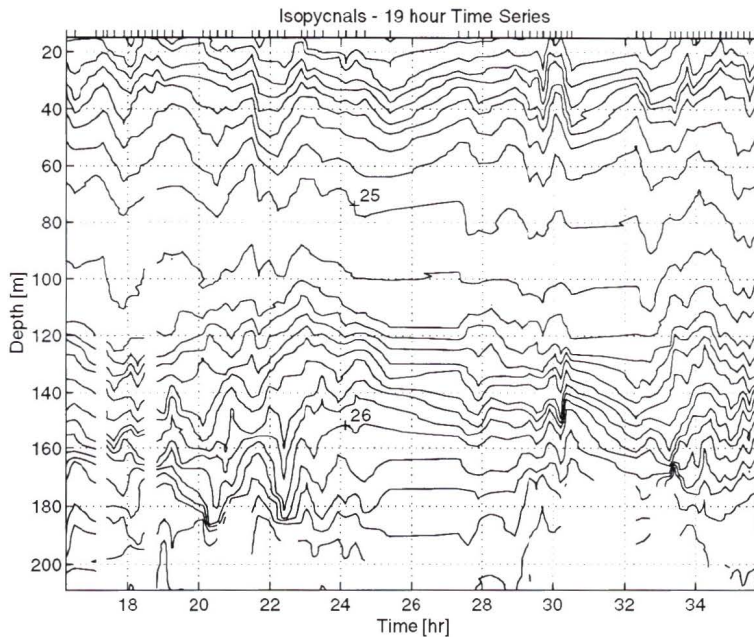


Figure 6.29: Constant σ_T surfaces for the 19 hour time series. The ticks on the upper x-axis indicate profile times. The isopycnals are set 0.1 kg m^{-3} apart, with isopycnals of 25 and 26 kg m^{-3} marked.

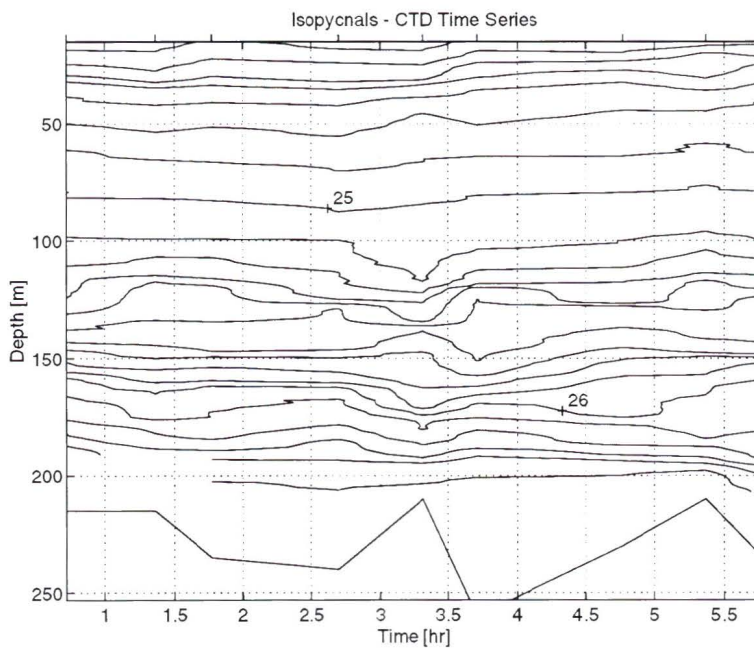


Figure 6.30: Constant σ_T surfaces for the CTD time series. The ticks on the upper x-axis indicates profile times. The isopycnals are set 0.1 kg m^{-3} apart, with isopycnals of 25 and 26 kg m^{-3} marked. The solid line at the bottom gives the depth of the water column.

Within the first 8 hours, motions with a 2 hour period are evident from 15 m to the top of the permanent pycnocline at 110 m. The displacements are between 15 and 20 m. Between 27:00 and 31:00 hours, motions with a period of 1.5 hours are present but displacements are less than 10 m. Within the last 4 hours of the time series a periodic motion of 2 hours occurs but here the displacement of isopycnals are present from 15 to 160 m. Some of these displacements are over 20 m. Within the seasonal and permanent pycnoclines, isopycnal motions with periods of an hour and less occur. Some of these can be detected throughout the entire pycnocline while others occur in only part of the pycnocline. The majority of the displacements of isopycnals at these low periods are less than 10 m. There is a general trend that longer period waves produce larger isopycnal displacements; therefore long period waves are resolved without significant aliasing.

The isopycnals of the CTD time series have motions that occur from time scales larger than the length of the time series to the smallest resolvable period (Fig. 6.30). Isopycnals near the surface tend to rise and those near the bottom tend to drop with time. If this motion is periodic it is the result of an internal wave with a period greater than 10 hours. Near the surface there are motions with periods of 2 hours and isopycnal displacements of less than 5 m. Between 60 and 80 m the motions have a period of 5 hours. Within the permanent pycnocline the motions occur at periods between 1 and 2 hours. Some of the related displacements are over 10 m. Some isopycnal movements may be the result of very strong mixing in the pycnocline (Fig. 6.32) and not internal waves.

6.2 Dissipation Rate Time Series

Dissipation rates have large scale changes with depth in the 19 hour time series (Fig. 6.31). Dissipation rates above 100 m are generally $< 10^{-8} \text{ W kg}^{-1}$ while below 100 m they are generally $> 10^{-8} \text{ W kg}^{-1}$. Below 230 m ϵ tends to be lower than

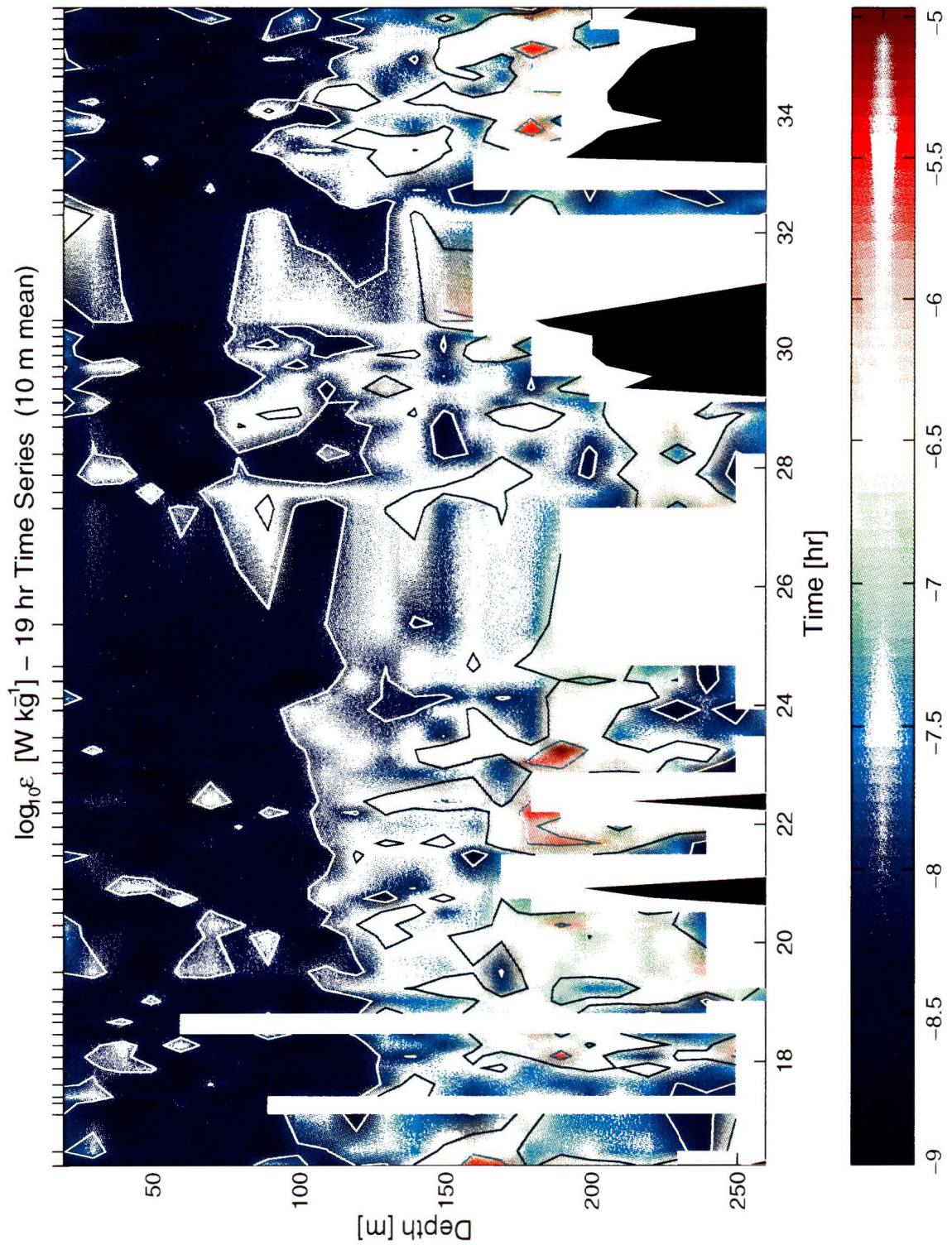


Figure 6.31: $\log_{10} \epsilon$ for the 19 hour time series. Contours for $\epsilon = 10^{-6}$, 10^{-7} and 10^{-8} W kg^{-1} are plotted. ϵ has been averaged into 10 m bins.

above 230 m. Dissipation maxima, areas with $\epsilon > 10^{-6} \text{ W kg}^{-1}$, occur from 70 to 150 m above the bottom before hour 26:00 and less than 50 m after hour 32:00. These dissipation maxima are reminiscent of the lower enhanced dissipation layer in transect 1. The drifting and repositioning of the ship during the time series provided the opportunity to transect the high dissipation layer numerous times. The area covered by the time series has a maximum north-south distance of ≈ 4.1 km and maximum east-west distance of ≈ 2.4 km. Between 18:00 and 25:00 hours the profiling pattern was equivalent to 5 transects from the rim to over 2 km east of the rim (Fig. 3.3). Profiles taken after 32:00 hours were to the south of the profiles taken before 26:00 hours. The profiling was done in a north-south line, with all the profiles close to the rim. The maxima we see here are similar to the high-dissipation lower layer that begins at the rim in transect 1. Between 26:00 and 32:00 hours the dissipation rates are not as large as at other times, however, between 27:00 and 29:00 hours there is a layer of $\epsilon > 10^{-7} \text{ W kg}^{-1}$ at a depth of 230 m. These profiles were taken further north and in deeper water (450-550 m) than any other profiles in the series. The layer at 230 m may also be part of an enhanced turbulence layer as exists before 26:00 hours and after 32:00 hours, only further from its source. We have, therefore, found an enhanced turbulent layer over the entire eastern portion of the seamount that is covered by the 19 hour time series. This indicates that the turbulent layer originating from the rim in transect 1 (Fig. 5.22) is not a unique feature of the south-east portion of the seamount.

Before 26:00 hours the enhanced dissipation layer persisted for the entire 8 hours we were profiling east of the rim. The layer between 26:00 and 32:00 hours was present for the entire 2 hours we profiled in the deep water. After 32:00 hours the layer persisted for the 3 hours we were near the rim. During these times the dissipation rates in the layer never dropped below $10^{-7} \text{ W kg}^{-1}$. Given the e-folding time of less than 10 minutes at the depth of 200 m, the internal wave field must

be continually creating turbulence over the time of our observations. Therefore, the internal-wave-driven enhanced-turbulence layer is a persistent feature whose time average is probably within an order of magnitude of ϵ values from a single profile. The thickness of the layer is less than 60 m and is thus only a feature associated with the rim.

The CTD time series has what were initially unexpected dissipation rates (Fig. 6.32). A layer of enhanced dissipation is present within the permanent pycnocline. It is the only feature of enhanced dissipation present in the time series and it was first observed over 100 m above the bottom. The enhanced dissipation layer was persistent throughout the entire 5 hours of the series. The layer went deeper with time and was within 30 m of the bottom on the second last profile. The maxima in dissipation in the layer are $> 10^{-6} \text{ W kg}^{-1}$.

The layer is unlikely the result of turbulent patches generated at the bottom and advected to the site of the time series. The layer is both thin and persistent along with being over 3 km from the pinnacle; therefore boundary separation at the pinnacle would need to be persistent, producing turbulent patches with dissipation rates that are a number of orders of magnitude larger than what was observed in the time series (27 orders if the mean advection was only 10 cm s^{-1}). Also, boundary separation could only occur over a depth range of 50 m to produce such a thin layer. This source for the layer is very unlikely given that the observations of dissipation rates near the pinnacle were no greater than those observed in the CTD time series. The source of the enhanced dissipation is probably an internal wave originating from the bottom.

6.3 Diffusivity Time Series

As with dissipation rates, there are large changes in diffusivity with depth for the 19 hour time series (Fig. 6.33). Diffusivities greater than that of the open ocean, $10^{-5} \text{ m}^2 \text{ s}^{-1}$, occur below 70 m for the vast majority of the time series. The enhanced

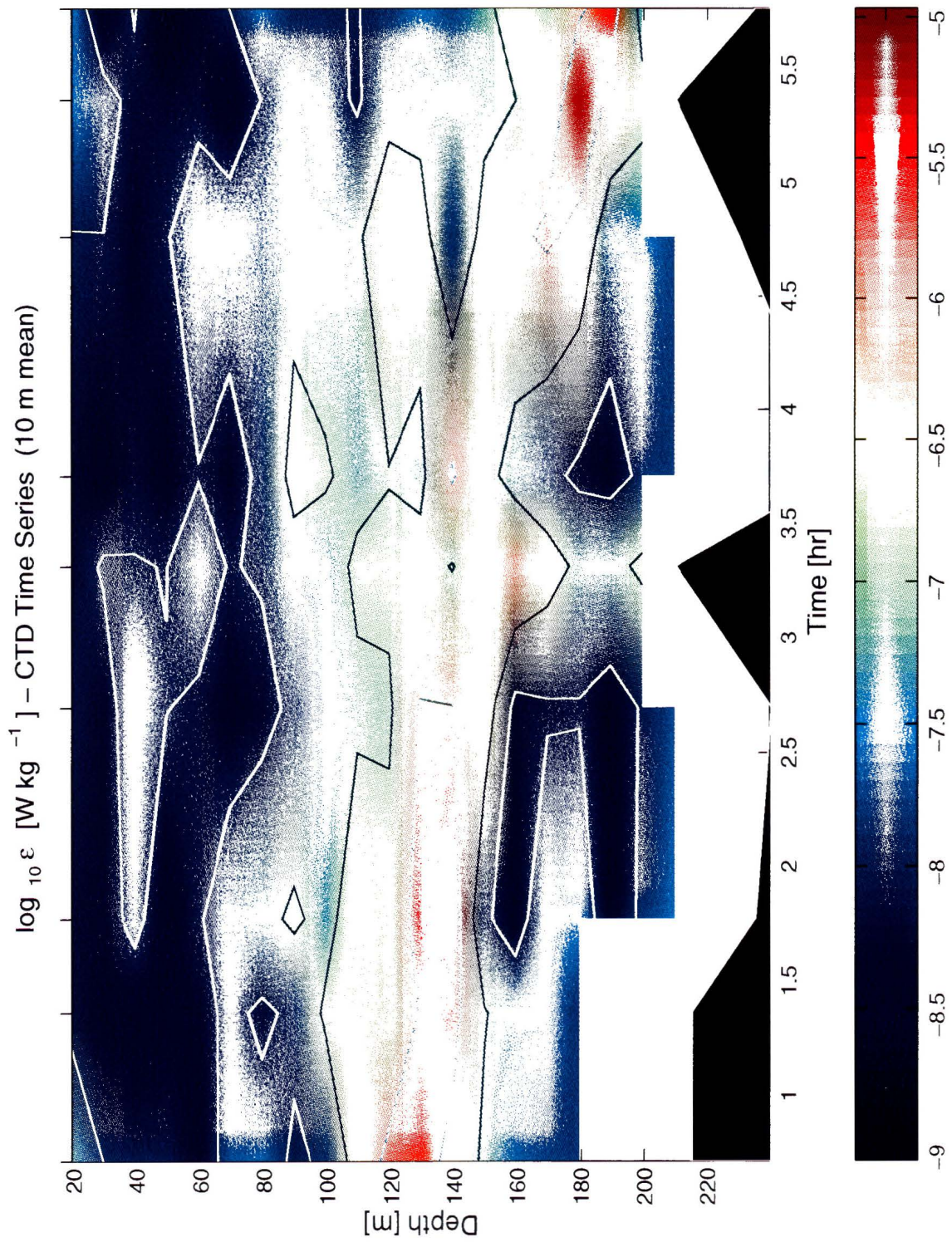


Figure 6.32: $\log_{10} \epsilon$ for the CTD time series. Contours for $\epsilon = 10^{-6}$, 10^{-7} and 10^{-8} W kg^{-1} are plotted. ϵ has been averaged into 10 m bins.

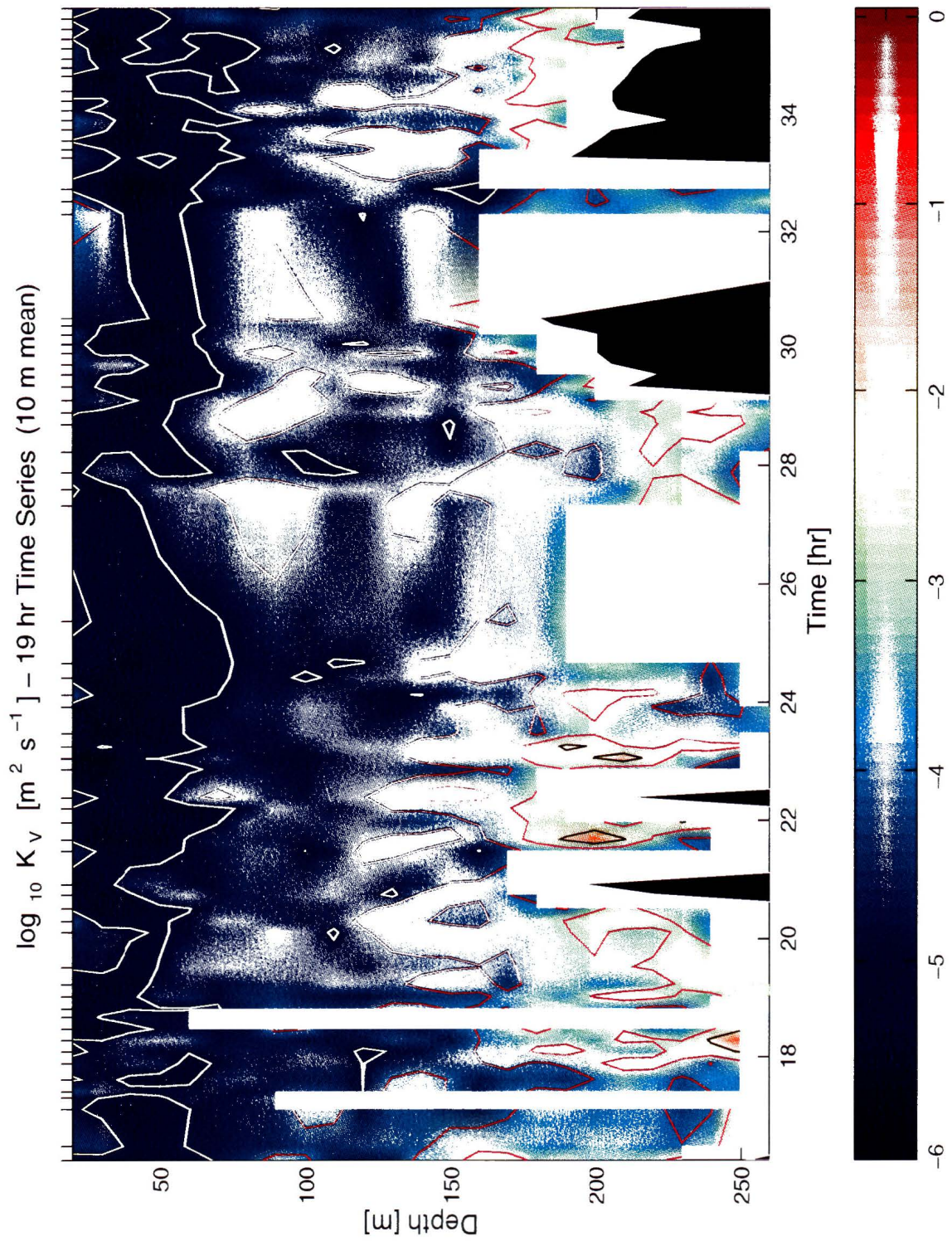


Figure 6.33: $\log_{10} K_v$ for the 19 hour time series. Contours for $K_v = 10^{-2}, 10^{-3}, 10^{-4}$ and $10^{-5} \text{ m}^2 \text{ s}^{-1}$ are plotted. K_v has been averaged into 10 m bins.

dissipation layer generated near the rim has the highest diffusivities. The shallowest (175 m) part of the layer has maximum diffusivities of $> 10^{-3} \text{ m}^2 \text{ s}^{-1}$ after 32:00 hours, as does the deepest (230 m) part of the layer between 26:00 and 32:00 hours. However, the largest diffusivities in the time series occur before 26:00 hours at the depths of 200 and 250 m and are $> 10^{-2} \text{ m}^2 \text{ s}^{-1}$. These maxima are as large as all but one of the local maxima found in transect 1. Therefore, enhanced mixing occurs over a large depth range and is persistent on the eastern flank of the seamount but the greatest mixing occurs in the internal wave generated layer off the rim, as we saw in transect 1.

The CTD time series has diffusivities that follow the pattern of the dissipation rates (Fig. 6.34). There is an enhanced diffusivity layer within the permanent pycnocline whose center drops with time from 130 m at the start to 180 m at the end of the time series. The layer persists through the entire 5 hours of the series. The maximum diffusivity in the layer, $> 10^{-3} \text{ m}^2 \text{ s}^{-1}$, is over 2 order of magnitude larger than open ocean values.

6.4 Discussion

Isopycnals have motions of various frequencies. Some of the amplitudes of these internal wave driven motions are greater than 10 m. Enhanced dissipation is generally found at greater depths and near the bottom. The most intense turbulence is found too far above the bottom to be associated with shear of the mean flow near the bottom. As seen in the transects, internal waves probably generate most of the enhanced turbulence. Most important was the discovery of an enhanced turbulence layer originating from the eastern portion of the rim which proves that enhanced turbulence layers generated by the semi-diurnal internal tide are not unique to transect 1. Turbulence around the seamount is persistent with dissipation rates varying by only a factor of 10.

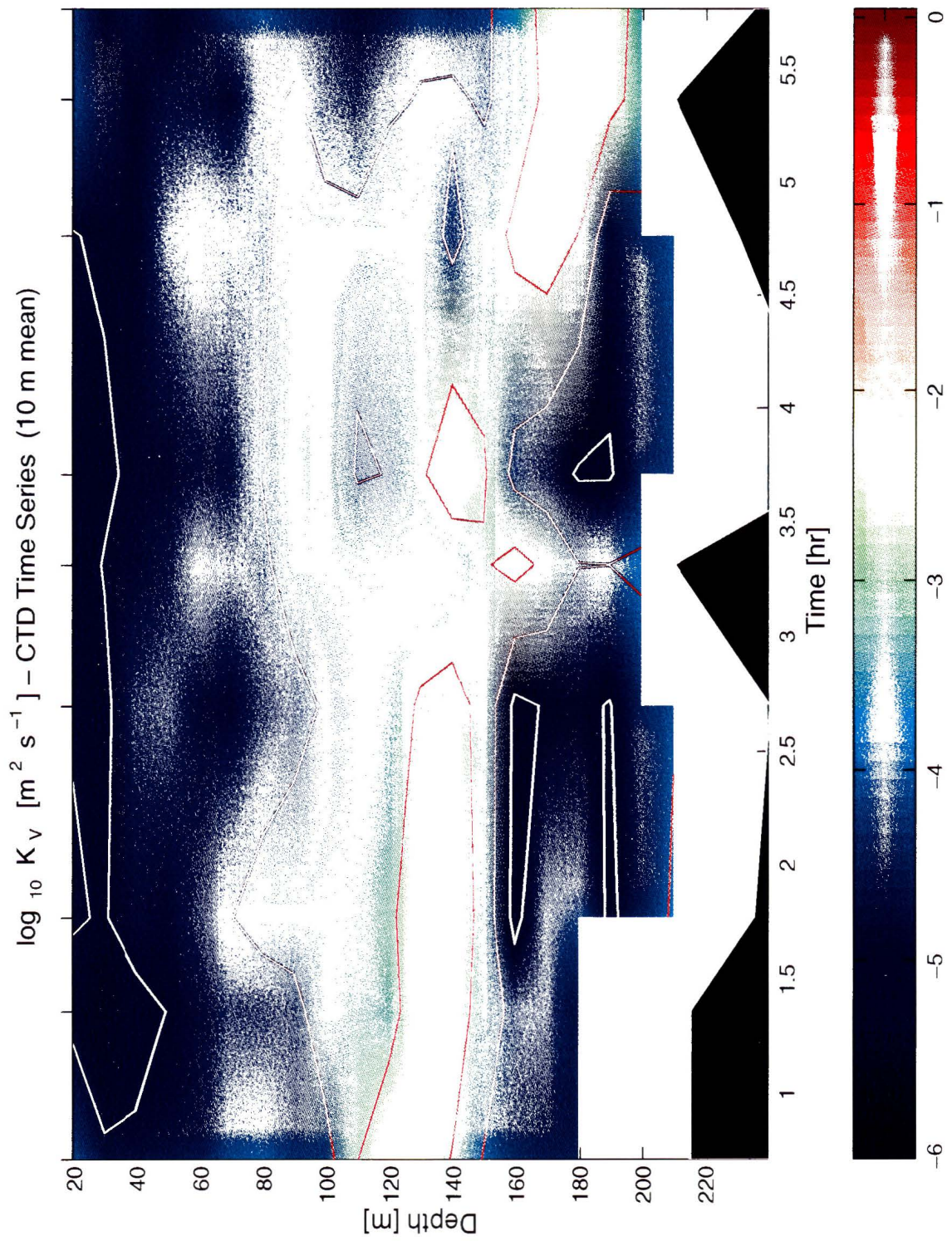


Figure 6.34: $\log_{10} K_v$ for the CTD time series. Contours for $K_v = 10^{-3}$, 10^{-4} and $10^{-5} \text{ m}^2 \text{ s}^{-1}$ are plotted. K_v has been averaged into 10 m bins.

Chapter 7

Bottom Boundary Layer Observations

FLY II was designed to land on the bottom we planned to have the majority of the profiles finish on the bottom. Unfortunately, during two of the first four profiles, the instrument's retrieval line became entangled for extended periods. It was only after a number of successful profiles away from the seamount during the 19 hour time series, and a change in retrieval technique, that we began to allow the instrument to land on the bottom again. Unfortunately, we did not acquire many bbl profiles because of the then limited amount of time left for the cruise.

These first ever profiles through the bbl of a seamount by a microstructure instrument allow us to address some questions:

- Does the bottom boundary layer show evidence of periodic domination by the tidal current and internal waves as was observed in the current meter results?
- Is the bottom boundary layer turbulent and does it follow a log layer structure?
- Is mixing in the bottom boundary layer more efficient than typically assumed?

Before going to Cobb Seamount we were already aware of the mean flow measurements of Freeland (*pers. comm.*) during the two previous Summers. We expected the flow field over the seamount to be dominated by an anti-cyclonic Taylor cap which should have generated a generally downward flowing Ekman layer. Following the work of Garrett *et al.* (1993), this should have resulted in a thick bml where the downward flow was eventually arrested by the horizontal density gradients that would have been created. There would still have been strong dissipation values in the bbl due to shear

series	profiles
3	13
4	4
5	15
6	19

Table 7.4: Number of profiles where FLY II landed on the bottom.

of the mean flow near the bottom but mixing in the bbl should have been inefficient in diminished stratification of the thick bml.

As observed in chapter 4, the current meter measurements of vertical temperature gradient in the bbl during times of strong along isobath flow follow this general idea. However, about half of the time the along isobath flow is weak and internal waves dominate the bbl structure. During these periods, the bml goes through rapid changes in thickness, leading to four different types of bottom boundary layer observed at Cobb:

1. The typical log layer. A bbl within which the dissipation rate decreases proportional to $1/z$ where z is the height above the bottom.
2. Dissipation capped by stratification. A thin bml that is capped by strong stratification. The turbulence generated at the bottom is also capped by the stratification.
3. Stratification with uncapped dissipation. A thin bml that is capped by strong stratification; however, the turbulence penetrates the stratified layer.
4. Capped dissipation in bml. A thick bml within which the dissipation rate decreases faster than $1/z$.

Some of the profiles show characteristics of more than one of these bbl types. One profile has none of these characteristics, having a thick bml (≈ 20 m) with a nearly constant dissipation rate throughout the entire bml.

7.1 Log Layer

From the first transect we have an example of the typical log layer type bbl (Fig. 7.35). The dissipation rate was determined by the temporal average technique to attain high spatial resolution. The dissipation has been smoothed with a five point running average, resulting in a spatial resolution of ≈ 0.5 m. The friction velocity was calculated using the high resolution dissipation without smoothing and by assuming that the dissipation fell off as for a smooth wall-bounded shear layer; thus (2.27) becomes

$$u_* = (0.4\epsilon z)^{1/3}. \quad (7.78)$$

The top of the bml was taken to be the lowest point where the temperature gradient, which was smoothed by an approximately 0.5 m running average, was greater than the mean temperature gradient taken over the entire 32.5 m of data shown. The minimum resolvable height of the bml is 0.4 m because of the 0.25 m edge effect of the smoothing and the 0.15 m between the sensors and the guard ring. The top of the turbulent bbl is taken as the deepest point where the smoothed high resolution dissipation rate is below $10^{-7.5}$ W kg⁻¹. The definitions of bml and turbulent bbl height are somewhat arbitrary and for this profile the definition of the bml height may be poor. In the bottom 3 m there are temperature fluctuations that are associated with turbulence and not a mean temperature gradient. This does indicate that the bottom 3 m are not well mixed but that the top of the bml might be best taken to be at 13 m or 18 m where there is a change in the mean stratification. This problem might have been taken care of by further filtering of the temperature record more; however this would have reduced the resolution below what is required to resolve the top of the bml of other profiles. The thickness of the turbulent bbl was 10.9 m, showing that all or most of the bml is turbulent, depending on which value of the bml is taken. Again, the limits placed on the thickness of the bbl may be considered arbitrary. The dissipation rates are almost never below 10^{-8} W kg⁻¹, yet the noise level of the

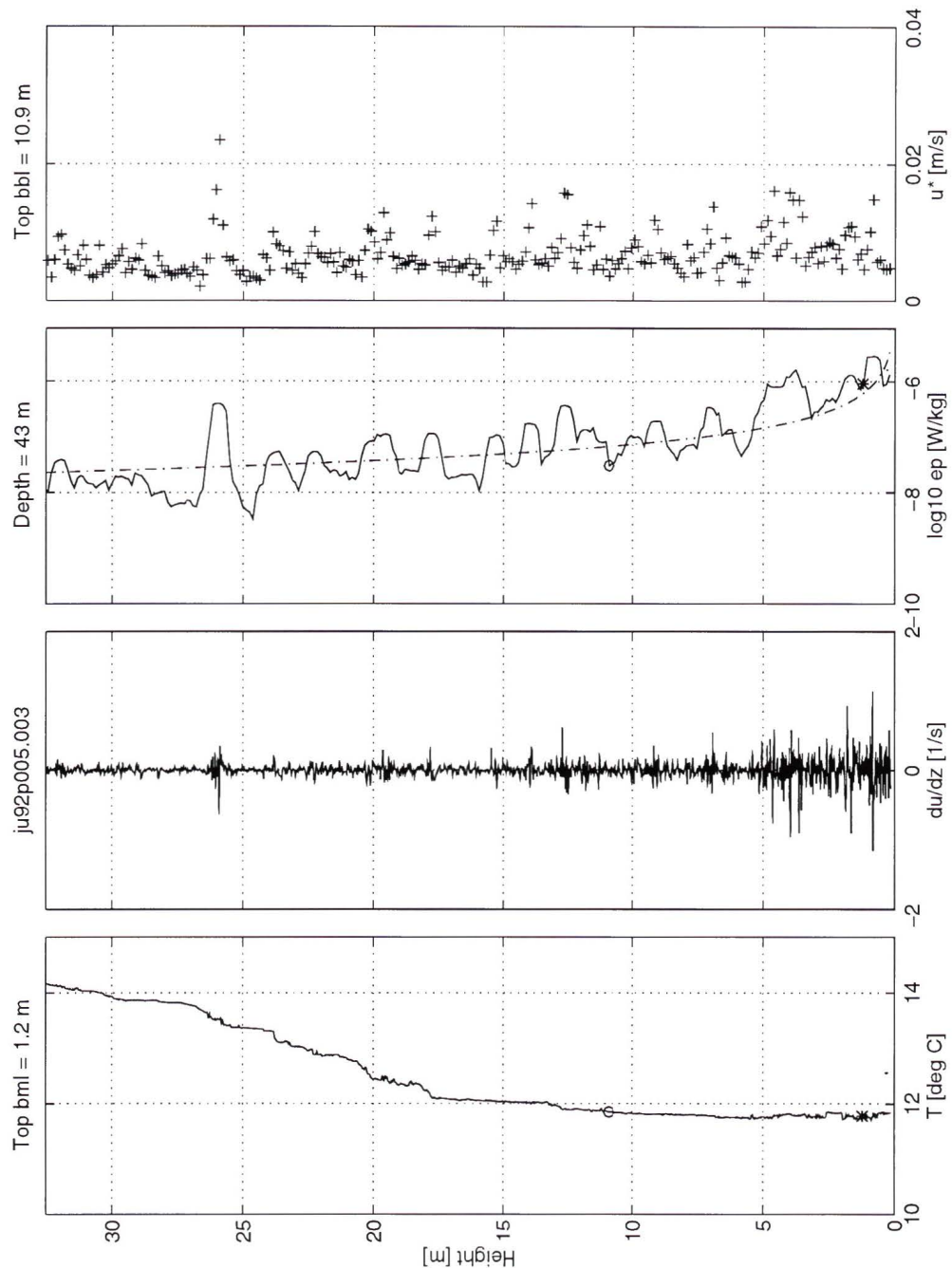


Figure 7.35: The shallowest bottom boundary layer profiled during the first transect. The diagrams from bottom to top are of high resolution temperature, microstructure shear, high resolution dissipation rate (solid line) with the theoretical dissipation for log layer (dashed and dotted line) and friction velocity. The thickness of the bml (*) and the turbulent bbl (o) are given, along with the water depth at the top of the diagrams.

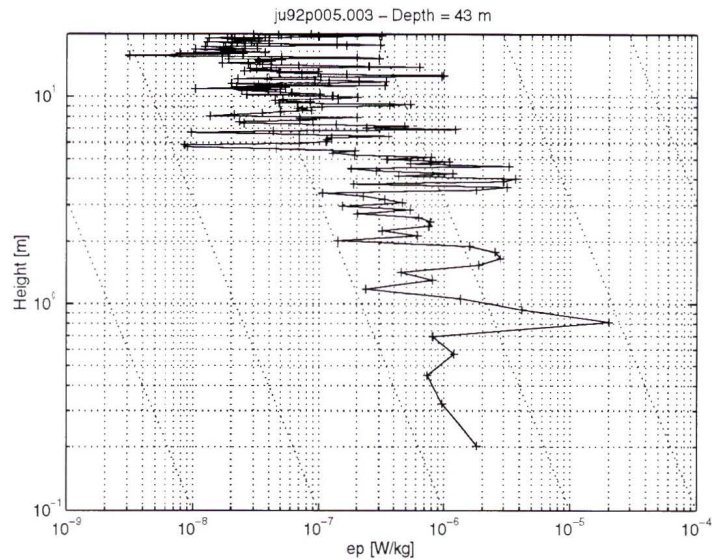


Figure 7.36: The unsmoothed version of high resolution dissipation from figure 7.35. Only the bottom 20 m has been plotted. The dotted diagonal lines all reduce as $1/z$.

instrument is $\approx 10^{-9} \text{ W kg}^{-1}$. Therefore, all of the 32.5 m of the water column may be considered to be mixing. The friction velocity is nearly constant through the first 5 m after which it reduces slightly. This implies that the dissipation rate decreases as a log layer, at least in the first 5 m.

The plot of dissipation rates in log-log space shows that the dissipation rate drops off as $1/z$ (Fig. 7.36). As was implied by the friction velocity, the bottom 5 m of the dissipation profile follows a log layer. Above 5 m there is a sudden drop in dissipation and the data follow the line that begins at $10^{-6} \text{ W kg}^{-1}$. This profile typifies the bbl structure we expected to observe over Cobb at all times. The number of profiles that meet the criterion that a log layer extends at least 4 m above the bottom is given in Table 7.5. In some of these profiles the log layer is greater than 10 m thick.

7.2 Stratification Capped Turbulence

From the second transect we have an example of dissipation rates that are capped by stratification (Fig. 7.37). The bml is very thin, only 0.5 m. The turbulent bbl

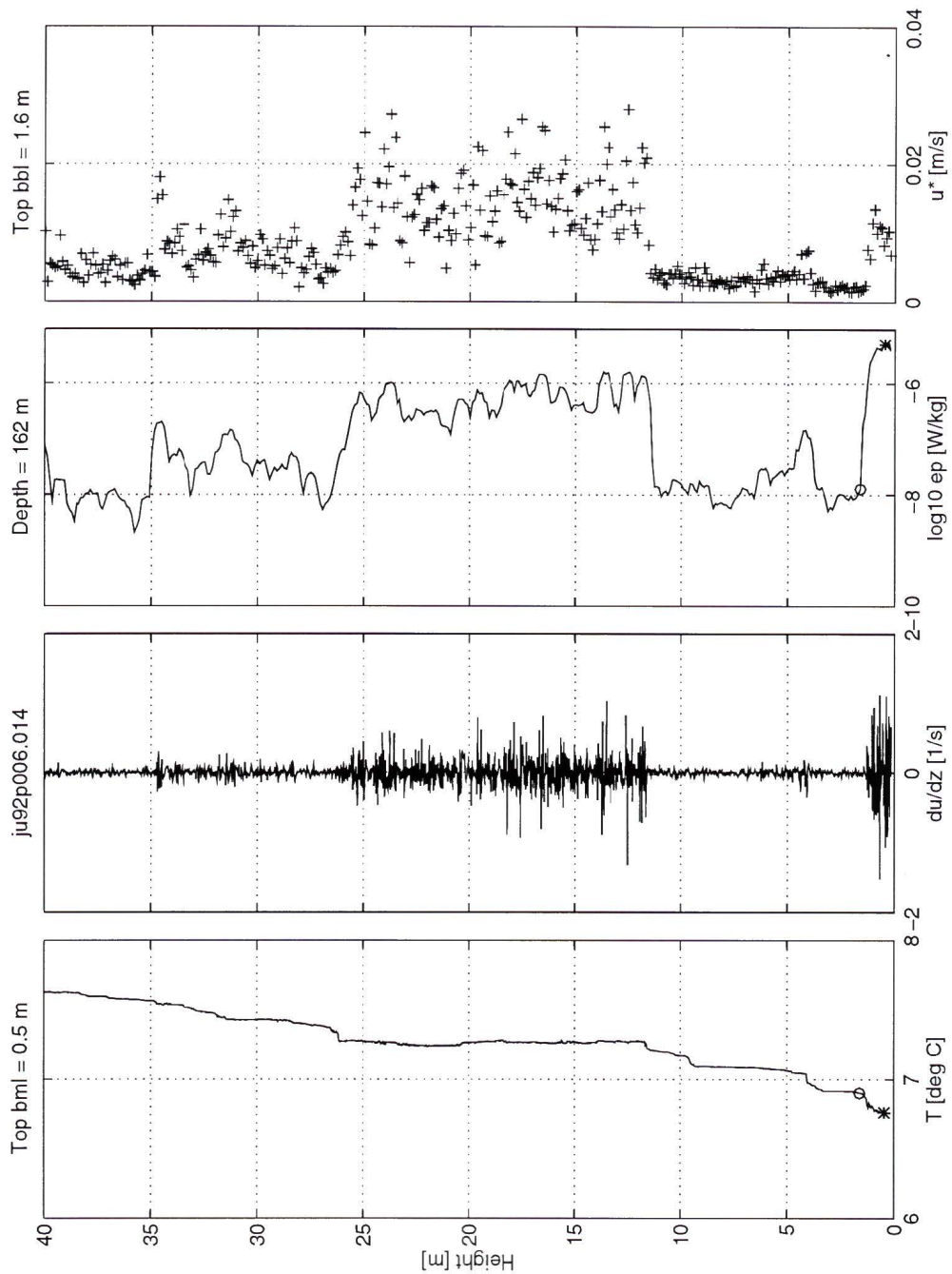


Figure 7.37: A bottom boundary layer over the flat top from the second transect. The diagrams from bottom to top are of high resolution temperature, microstructure shear, high resolution dissipation rate and friction velocity. The thickness of the bml (*) and the turbulent bbl (o) are given, along with the water depth at the top of the diagrams.

series	<i>BBL Type</i>			
	1	2	3	4
3	8	1	5	3
4	2	3	0	0
5	5	6	7	0
6	7	6	6	4

Table 7.5: Number of profiles of each BBL type.

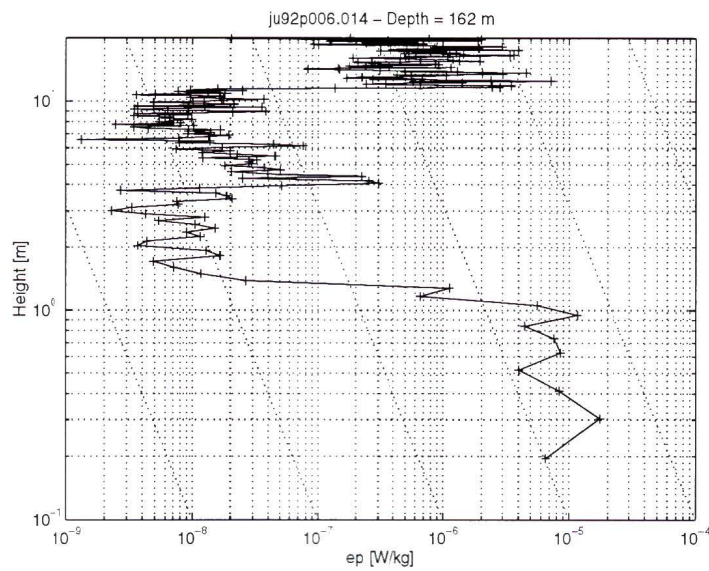


Figure 7.38: The unsmoothed version of high resolution dissipation from figure 7.37. Only the bottom 20 m has been plotted. The dotted diagonal lines all reduce as $1/z$.

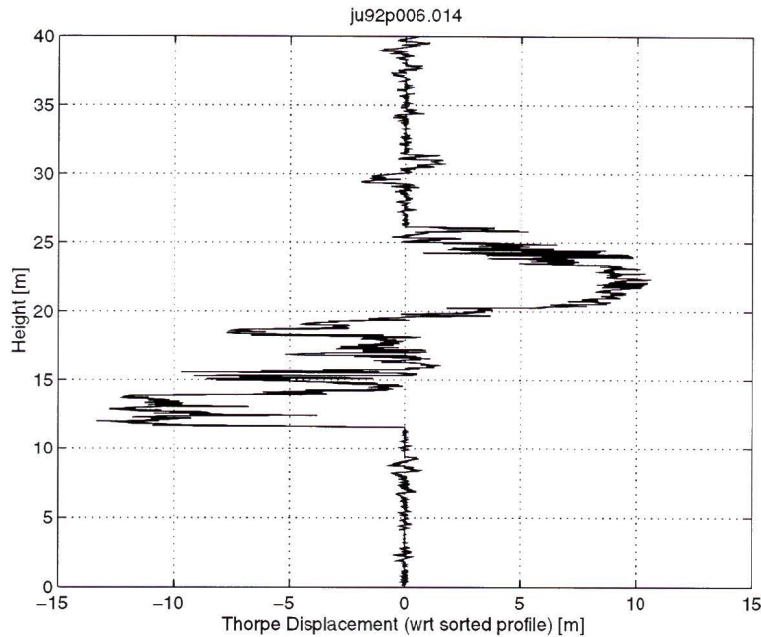


Figure 7.39: Thorpe displacement of the temperature profile in figure 7.37.

thickness is a slightly thicker 1.6 m. The dissipation rate in the bottom 1 m is nearly constant. Between 1 and 2 m the dissipation rate drops by 3 orders of magnitude (Fig. 7.38). The strong stratification caps the turbulence generated at the bottom. To have generated this bbl structure there must have been a thin (< 2 m) upslope flow. The flow could produce strong turbulence which produces mixing, but it may not be strong enough to overcome the stratification effect of advecting cold water upslope.

Above 12 m the dissipation increases by about 2 orders of magnitude to form a nearly constant dissipation layer that is 13 m thick. This layer was not generated near the bottom by shear of the geostrophic-interior flow. The profile was taken over the flat beach region on the eastern side of the seamount; therefore any patch originating from the bottom would have to be advected many 100's of meters. This is unlikely given that the patch is within the permanent pycnocline where the e-folding time is less than 5 minutes. Within the dissipation layer there is a temperature inversion with a corresponding z -like Thorpe displacement (Fig. 7.39) that is characteristic of

a billow. The layer is most likely the result of the breaking of an internal wave.

7.3 Stratification with Uncapped Turbulence

An example of dissipation rates that are unaffected by stratification is given in the third example of a bbl (Figs. 7.40 and 7.41). For this profile there is no bml. The temperature signal has a number of overturns in the bottom 3 m resulting from turbulence. The dissipation rates do not suggest that any log layer has formed. The rates are high for the entire bottom 25 m of the profile. The extremely cold bbl implies a thin jet is flowing upslope, perhaps generated by an internal wave. There is a temperature inversion between 13 m and 25 m which is also evident in the Thorpe displacement (Fig. 7.42). There are many other smaller overturns below 13 m and above 25 m. This profile was near the deepest part of the rim of the seamount, where internal tides may be generated and reflected. The turbulence is probably the result of shear in the flow near the bottom and internal wave breaking. It is an example of where it becomes impossible to distinguish between bottom generated turbulence and turbulence generated by internal waves. In these circumstances the turbulent bottom boundary layer can not be considered separate from the interior.

7.4 Capped Dissipation in BML

The last type of bbl is one with a thick bml but with a dissipation rate profile that decreases faster than $1/z$ (figures 7.43 and 7.44). The bml for our example is 11.7 m thick; however the turbulent bbl is only 2.4 m thick. The bottom 2 m of dissipation rate profile is nearly constant, with a drop of 1.5 orders of magnitude in 30 cm at the height of 2 m. The dissipation rate profile does not decrease as $1/z$ in this case but unlike other profiles this non-log layer bbl is not the result of stratification. The source of this thin turbulent bbl can not be shear of the mean flow generated at a smooth bottom. The source is likely either form drag with high basalt columns and

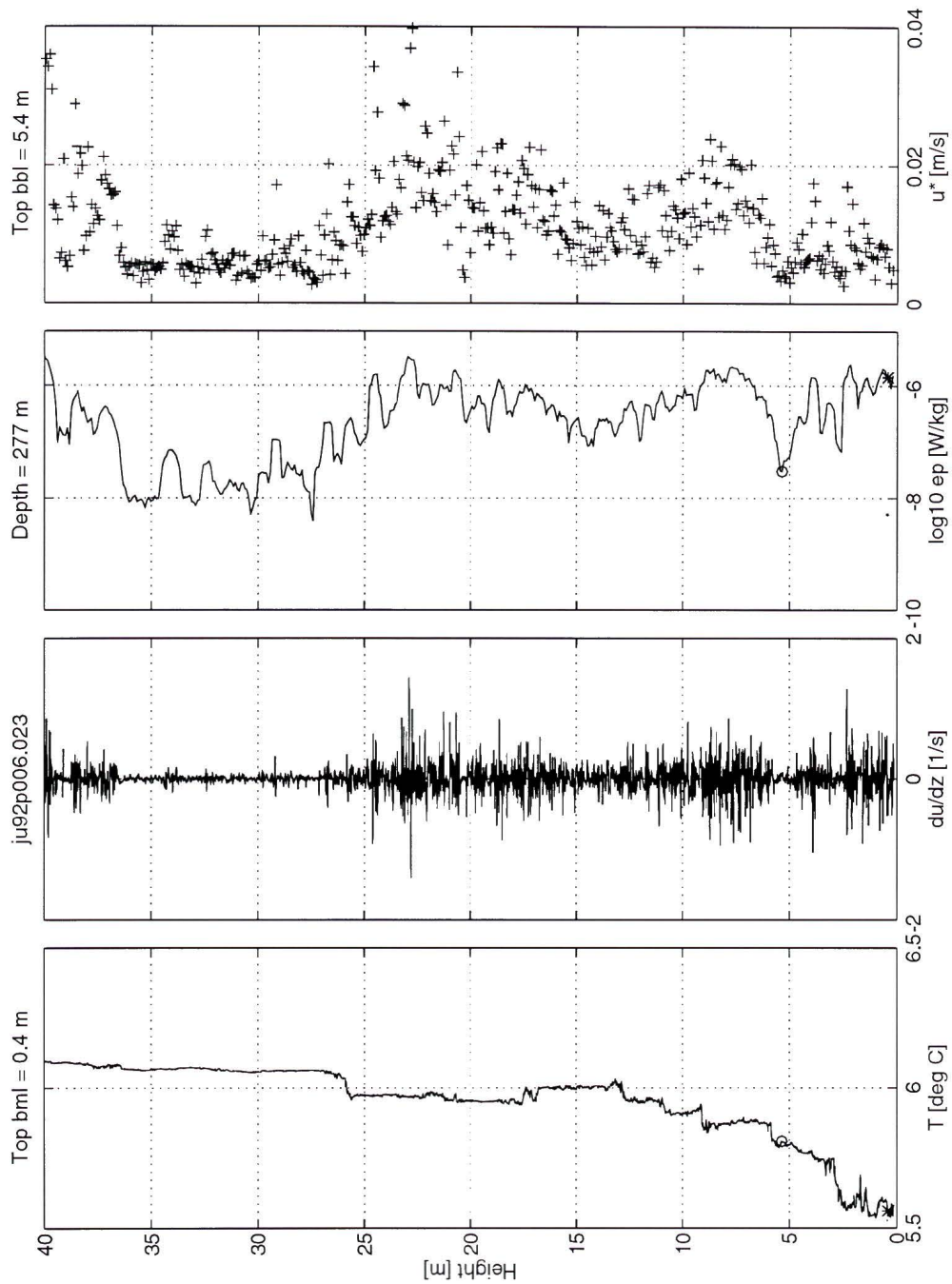


Figure 7.40: The deepest bottom boundary layer profiled during the second transect. The diagrams from bottom to top are of high resolution temperature, microstructure shear, high resolution dissipation rate and friction velocity. The thickness of the bml (*) and the turbulent bbl (o) are given, along with the water depth at the top of the diagrams.

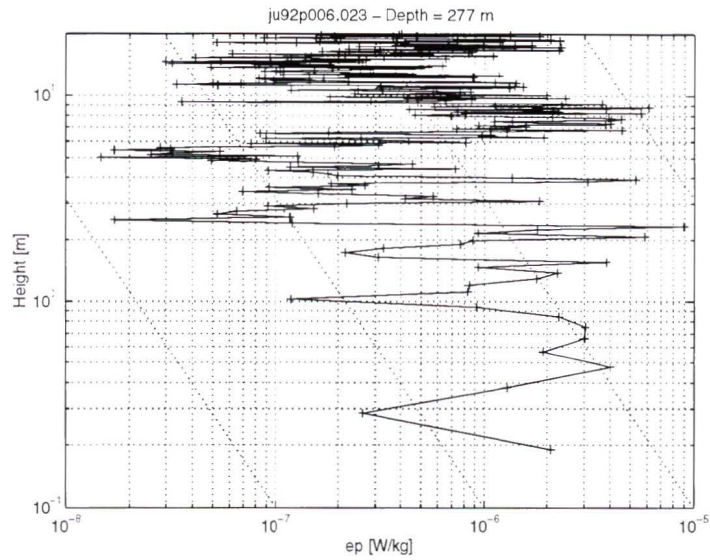


Figure 7.41: The unsmoothed version of high resolution dissipation from figure 7.40. Only the bottom 20 m has been plotted. The dotted diagonal lines all reduce as $1/z$.

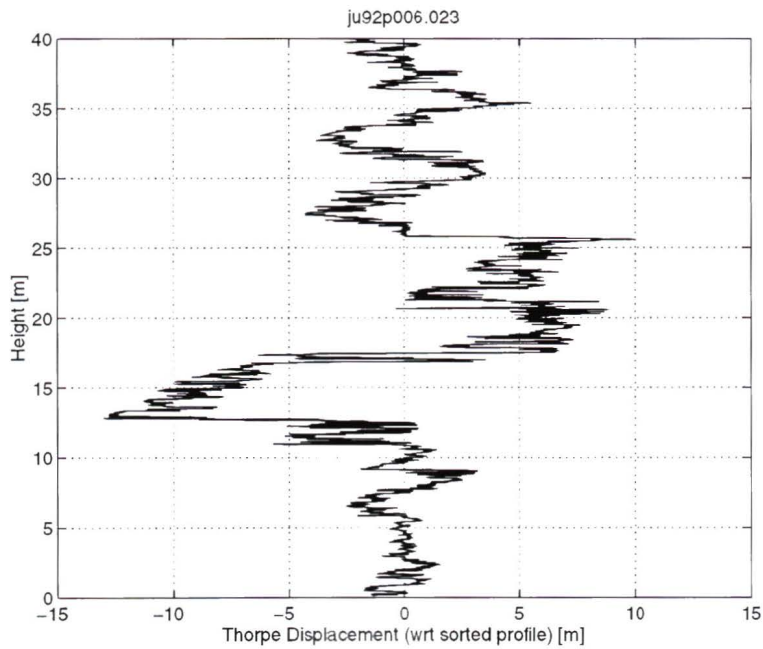


Figure 7.42: Thorpe displacement of the temperature profile in figure 7.40.

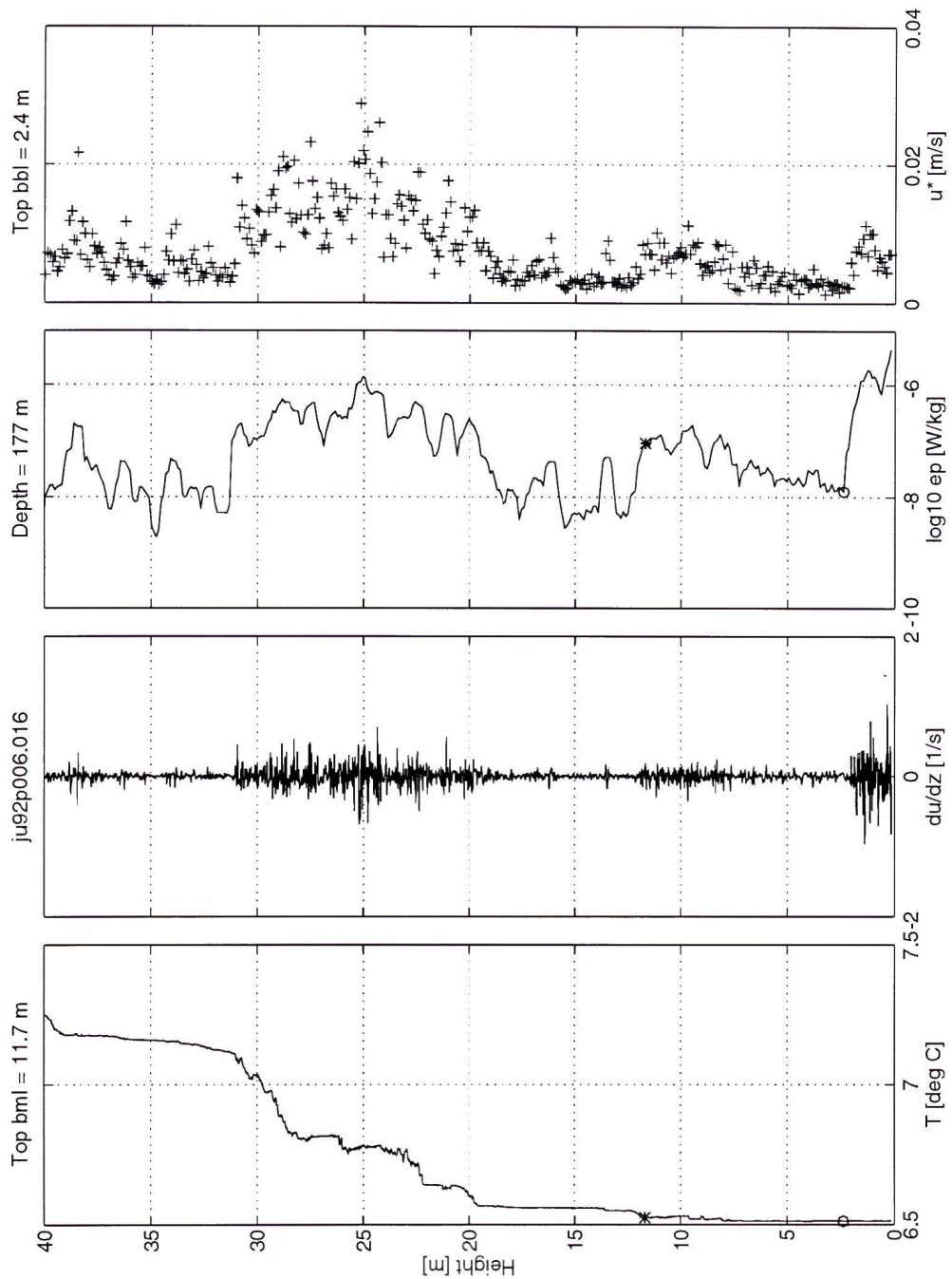


Figure 7.43: The bottom boundary layer from a shallower profile of the second transect. The diagrams from bottom to top are of high resolution temperature, microstructure shear, high resolution dissipation rate and friction velocity. The thickness of the bml (*) and the turbulent bbl (o) are given, along with the water depth at the top of the diagrams.

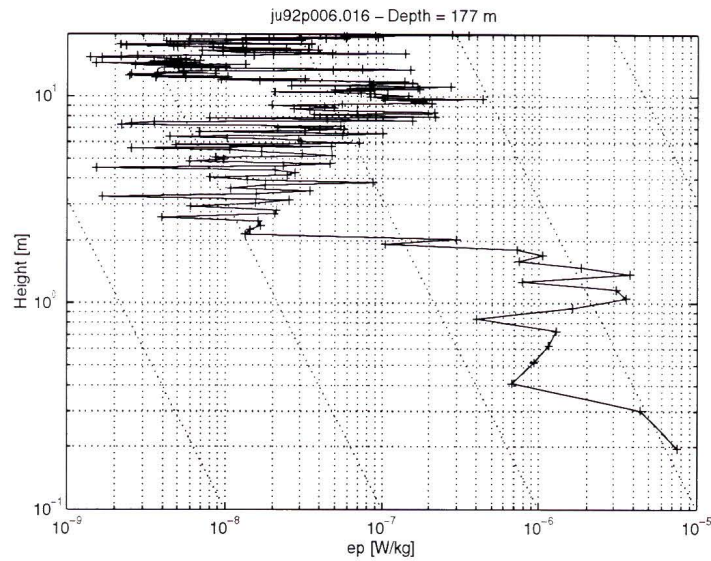


Figure 7.44: The unsmoothed version of high resolution dissipation from figure 7.41. Only the bottom 20 m has been plotted. The dotted diagonal lines all reduce as $1/z$.

boulders or an ≈ 2 m thick current that is flowing either along isobaths or downslope. If the flow were upslope then the temperature profile would be expected to show a rapid decrease in the bottom 2 m, as observed with other profiles.

7.5 Bottom Mixing Efficiency

Bottom boundary mixing at Cobb is intermittent. The bml goes from being very thin (< 1 m) to moderately thick (≈ 10 m) in a few hours. Over longer periods (diurnal tides) the bml may thicken to ≈ 20 m. At the M3 mooring the bml is over 50 m thick on 7 occasions over less than 7 days of current meter records. The occurrences are not periodic. This intermittency in the bottom mixing is probably the result of internal waves and tides. By using the approach outlined by Garrett (1991) for intermittent boundary mixing I will estimate the effective mixing occurring in the bbl.

Under conditions where there is no net upslope or downslope flow, Garrett derives

the effective vertical diffusivity in an intermittently mixed bml as

$$K_v^{eff} = \frac{h^2}{24T}, \quad (7.79)$$

where h is the maximum vertical thickness of the bml and T is the average time between mixing events. For the lowest period between mixing events (≈ 2 hours) $K_v^{eff} \approx 6 \times 10^{-4} \text{ m}^2 \text{ s}^{-1}$. For intermittent mixing at tidal frequencies $K_v^{eff} \approx 2 \times 10^{-4} \text{ m}^2 \text{ s}^{-1}$. At M3 $K_v^{eff} \approx 1 \times 10^{-3} \text{ m}^2 \text{ s}^{-1}$. These diffusivities are larger than open ocean conditions but they are smaller than many of the depth averaged diffusivities I derived for transect 1 (Fig. 5.26). These boundaries are also much thinner and affect a smaller cross-sectional area of the ocean than the enhanced mixing layers generated by internal waves. Therefore, it is not surprising that intermittent boundary layer mixing does the equivalent of 10–500 km² of open ocean mixing over the flat top of the seamount, and 400–1000 km² over the flank, or about three orders of magnitude less than the area of open ocean mixed by internal waves (Fig. 5.27).

There are a few important limitations to this derivation of effective boundary mixing. The intermittent mixing model I have applied was for no net upslope or downslope flow. To apply Garrett's (1991) extension of this model to cross-isobath flow is not trivial. The general result is that isopycnals bend with net across isobath flow, biasing the bml thicknesses. Any error in h creates a large error in K_v^{eff} . The limited data sets make estimating maximum bml thickness difficult. The current meter moorings poorly resolve h with only 3 thermometers and the number of microstructure profiles into the bml are not sufficient to estimate maximum h over the scale of hours to days. There is also the possibility that much of the bbl mixing may be the result of internal wave breaking and shear near the bottom as was seen for the examples of bbl types 2 and 3; therefore considering the bbl mixing as separate from interior mixing may be incorrect.

7.6 Bottom Mixed Layer Thickness Models

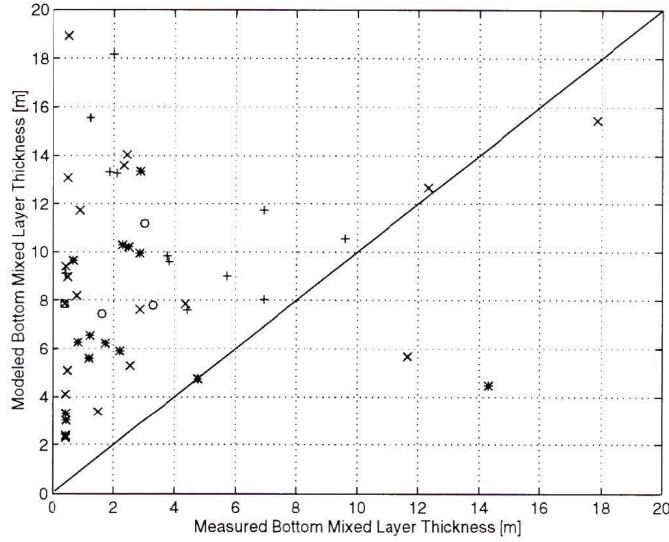


Figure 7.45: Modeled versus measured bottom mixed layer thicknesses. The model thickness is $h_{tl} = 2^{1/4}u_* / (fN)^{1/2}$. The points are plotted by series; + for the 19 hour time series, o for the CTD time series, * for transect 1, and x for transect 2.

Various one dimensional bottom boundary layer models have been used to predict mixed layer thicknesses. Weatherly and Martin's (1978) model used a Mellor and Yamada Level II closure scheme and determined the boundary layer thickness to be

$$h_{wm} = 1.3 \frac{u_*}{f[1 + (N/f)^2]^{1/4}}, \quad (7.80)$$

over a flat bottom, where u_* is the friction velocity, f is the planetary vorticity and N is the buoyancy frequency. Trowbridge and Lentz (1991) used a Pollard-Rhines-Thompson model to determine

$$h_{tl} = \frac{2^{1/4}u_*}{\sqrt{fN}}. \quad (7.81)$$

For the profiles from transect 1 h_{wm} is 8.5% larger than h_{tl} . The difference between the largest and smallest percentage is only 0.01%. Both models give nearly identical results, with only a small fractional difference, allowing me to use the simpler h_{tl} . Weatherly and Martin (1978) find that over a sloping boundary where upslope flow occurs the bbl thickness is approximately given by (7.80) but where downslope flow occurs the bbl thickness may be appreciably larger than h_{wm} . The Trowbridge and

Lentz model is similarly limited.

Using the average u_* (7.78) within the bml and N as determined from the far-field of transect 1, I have estimated h_{bl} for all of the bbl profiles. Most of the profiles were taken above the flat top of the seamount, where the slope ranges from 0.01–0.06. The ratio of f/N over the flat top (0.008–0.02) is slightly smaller than the slope, which implies that the top of the seamount cannot be considered flat. Very few of the measured bml thicknesses match the model predictions (Fig. 7.45). The three profiles with thicker bmls than predicted were taken over the flat portion of the seamount, near the rim. These may have been the result of a downslope flow but internal wave breaking and shear within and just above the bml are likely causes. The vast majority of the bottom boundary layers were thinner than the predictions. The medians of model and measured thicknesses are 8.6 and 3.2 m. This is expected for a bbl over a slope but the severe overestimation of the model for many of the profiles implies the bml at Cobb is rarely fully developed, which is probably a result of high frequency cross-isobath flows.

7.7 Discussion

The bottom boundary layer is periodically dominated by the strong diurnal tidal signal plus internal waves. The diurnal tide signal along isobaths produces a slowly varying bml thickness that may get as large as 20 m over the flat top of the seamount. Internal waves appear to create thin turbulent flows that drive bottom water up and down slope. These flows can be on the order of 1 m thick, as seen with the example for the bbl type 2, but other profiles of the bbl that are not shown imply these bottom flows may be 5–10 m thick.

The bbl follows a log layer structure for the bottom 4 m for almost 45% of our profiles. Approximately 55% of profiles are not log layers and may have been generated by internal wave breaking and shear. These may have been affected by stratification

less than 4 m from the bottom or may be the result of turbulence generated by form drag. Some bbls form a log layer structure near the bottom but the dissipation rates above the log layer rise (bbl types 2 and 3 are examples). In over 45% of the profiles bottom turbulence was either capped by stratification or dropped off well below the top of the bml. For some of these cases bottom turbulence contributes nothing to mixing water, due to diminished stratification, while for others the turbulence penetrates part of stratified layer. For over 35% of the profiles the turbulence is unaffected by the stratification at the top of the bml. For these profiles the strong turbulence near the bottom is producing effective mixing that is thickening the bml. Approximately 20% of the profiles were difficult to classify as either bbl type 2, 3 or 4. Modeling of the bottom boundary at Cobb must consider both mixing by bottom generated shear of periodic currents and internal wave breaking.

Mixing in the bottom boundary may be 10–100 times more effective than equivalent open ocean mixing for an equal volume of water; however, given the small volume of water in the bbl, the near boundary process of internal wave breaking does 10–100 times more mixing than bbl processes.

Chapter 8

Counting Spikes

Airfoil shear probes used in oceanic research are prone to anomalous signals that are unrelated to turbulence. The usual source of these anomalous signals is believed to be particle hits on the probes. The particles may be biological in origin, such as phytoplankton, zooplankton or detritus; or they may be inorganic particles, such as sediments near the bottom. By identifying spatial and temporal trends in the anomalous signals I will attempt to identify their source.

Most anomalous shear signals have a large amplitude and short duration. The spikes occur over 10–20 samples, equivalent to a length of 2–4 cm. These signals are usually two sided and are easily identified (Fig. 8.46). Their contribution to the variance and thereby the estimated ϵ is quite significant. For example, the variance of the upper, spikey curve is about 175 counts² while the variance of the lower, despiked curve is about 39 counts². In order to determine an unbiased ϵ , these spikes must be removed; however in identifying the number and positions of the spikes may allow us to determine the relative concentration of particles in the water.

Spike identification was done manually. The number of spikes with an amplitude greater than 12 counts in 10 m bins was determined. The manual identification was biased in determining the smallest spikes. This bias has been removed because only spikes whose amplitude was greater than 2 standard deviations of a quiescent signal, such as the bottom curve in Fig. 8.46, have been counted.

8.1 Measurements

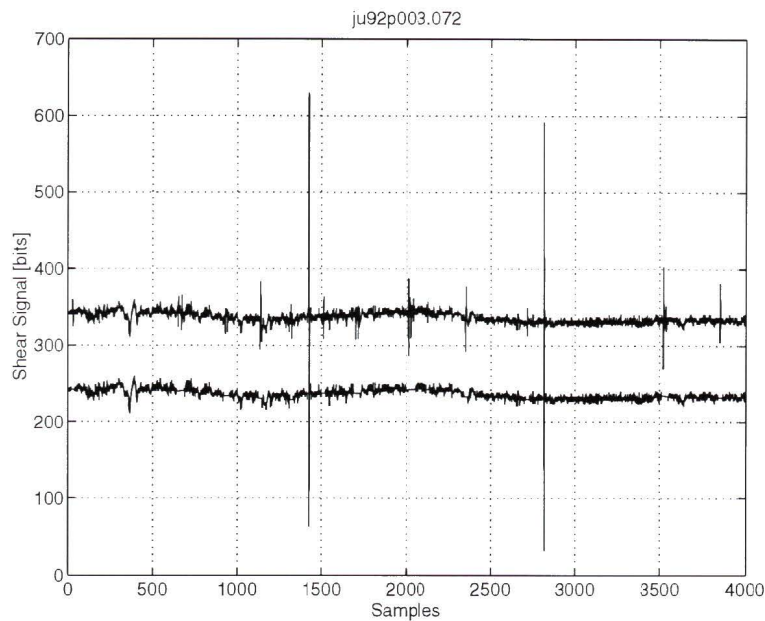


Figure 8.46: A section of shear signal from a single profile in the 19 hour time series. The upper curve is the original shear signal before the spikes are removed. The bottom curve is a plot of the signal after despiking, intentionally staggered down 100 counts.

The resulting profiles have been ensemble averaged over each of the four distinct series (Fig. 8.47). All four of the series have a strong gradient in the number of spikes, with the maximum number of spikes near the surface.

During the CTD time series 11 profiles of the CTD operated by Freeland and Dower coincided with the 9 profiles by FLY II. I have converted the percent light transmission, measured by a transmissometer on the CTD, into suspended particulate matter (SPM) concentrations by Bishop's (1986) method. The ensemble average of SPM from the 11 profiles was smoothed with an 11 m running average and plotted with the ensemble average of number of spikes from the CTD time series (Fig. 8.48). Both profiles follow the same general trend that the maximum concentration of particles is near the surface; however the relative gradient of number of spikes is larger above 50 m than the relative gradient in SPM, indicating that one of the instruments detected different particles.

The light transmission profiles from the cruise in 1990 (Dower 1994) show similar

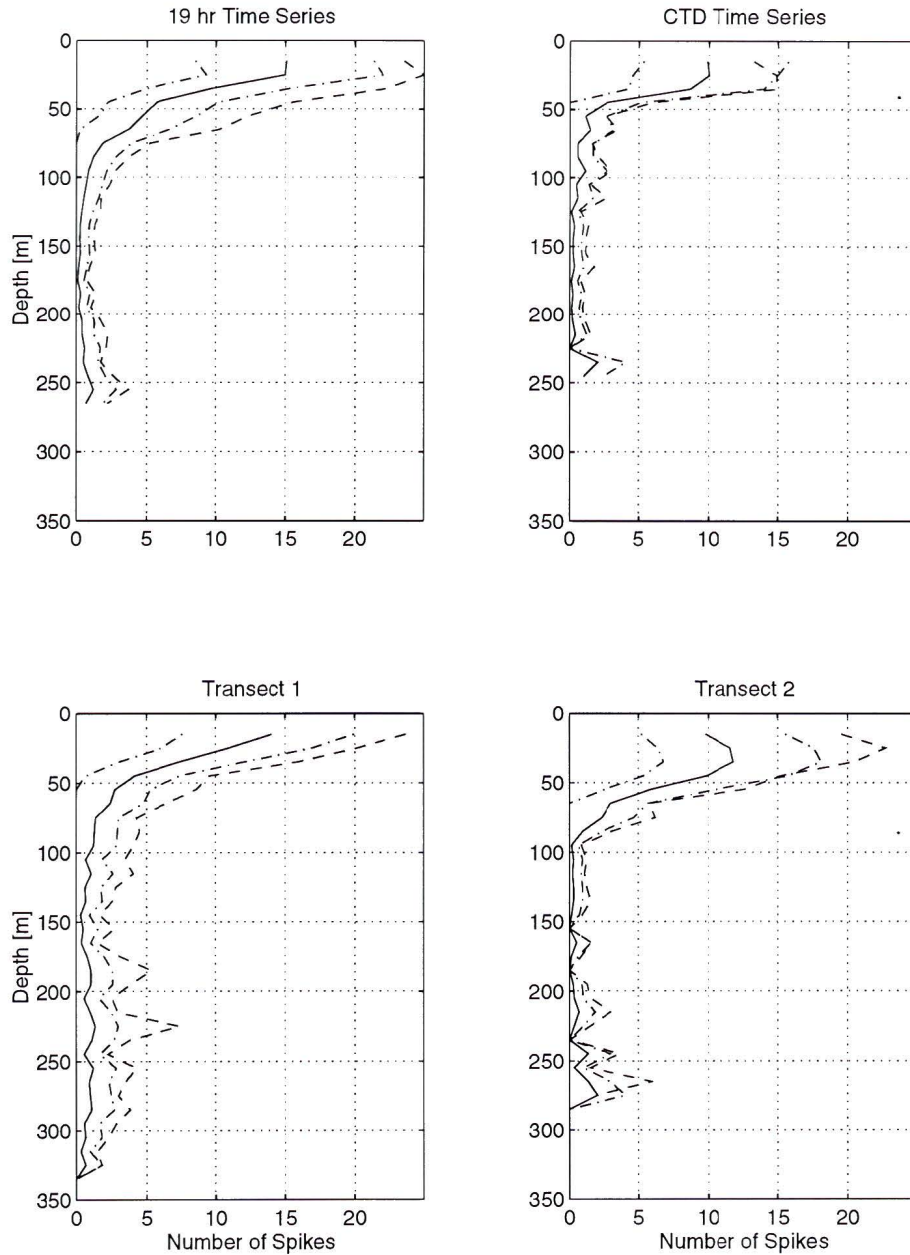


Figure 8.47: Ensemble averages of spikes for each series. The solid lines are the averages while the dashed lines are the averages plus 2 sample standard deviations. The dashed-dotted lines are 95% confidence limits assuming the spikes follow a Poisson distribution.

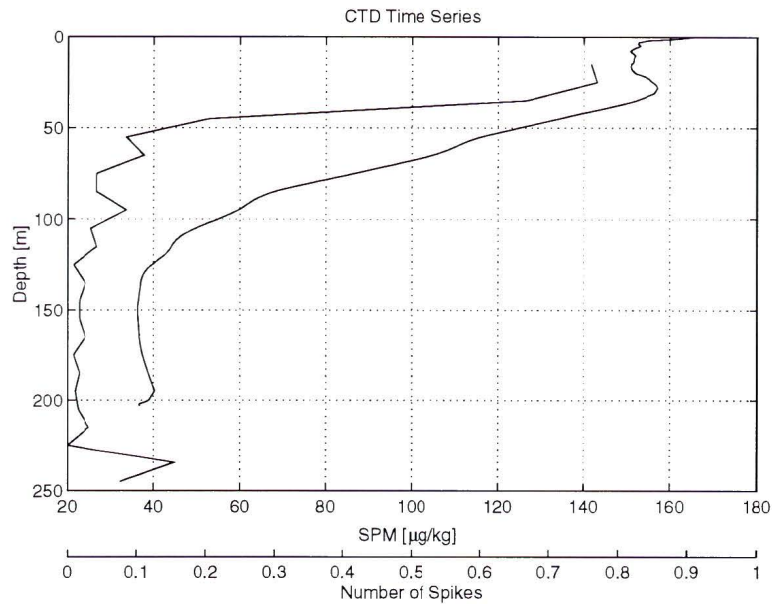


Figure 8.48: Suspended particulate matter (right curve) and the ensemble average of number of spikes (left curve) for the CTD time series.

spatial trends as profiles of the number of spikes taken by FLY II during the 1992 cruise. In a 55 km east-west transect of the seamount the minima in light transmission (the equivalent of a maximum in spm) were not over the pinnacle of the seamount but was 5–10 km away from the pinnacle. Spikes show corresponding maxima away from the pinnacle of the seamount (figures 8.49 and 8.50). Near the pinnacle there are less than 10 spikes in each 10 m bin while 10 m bins at the same depths away from the pinnacle have typically more than 10 spikes and sometimes more than 15 spikes. Both transects appear to have two local maxima in spikes off the pinnacle. The first transect has local maxima at about 3 and 9 km away from the pinnacle while the second transect has maxima at about 1 and 2.5 km away from the pinnacle.

The longest time series shows that the spiking of the shear signal has no distinct time dependence (Fig. 8.51). The lack of a daily fluctuation of the spiking, especially the lack of a daily signal that would show a local spike maxima rising in the evening and dropping in the morning may indicate that species of zooplankton that are diel

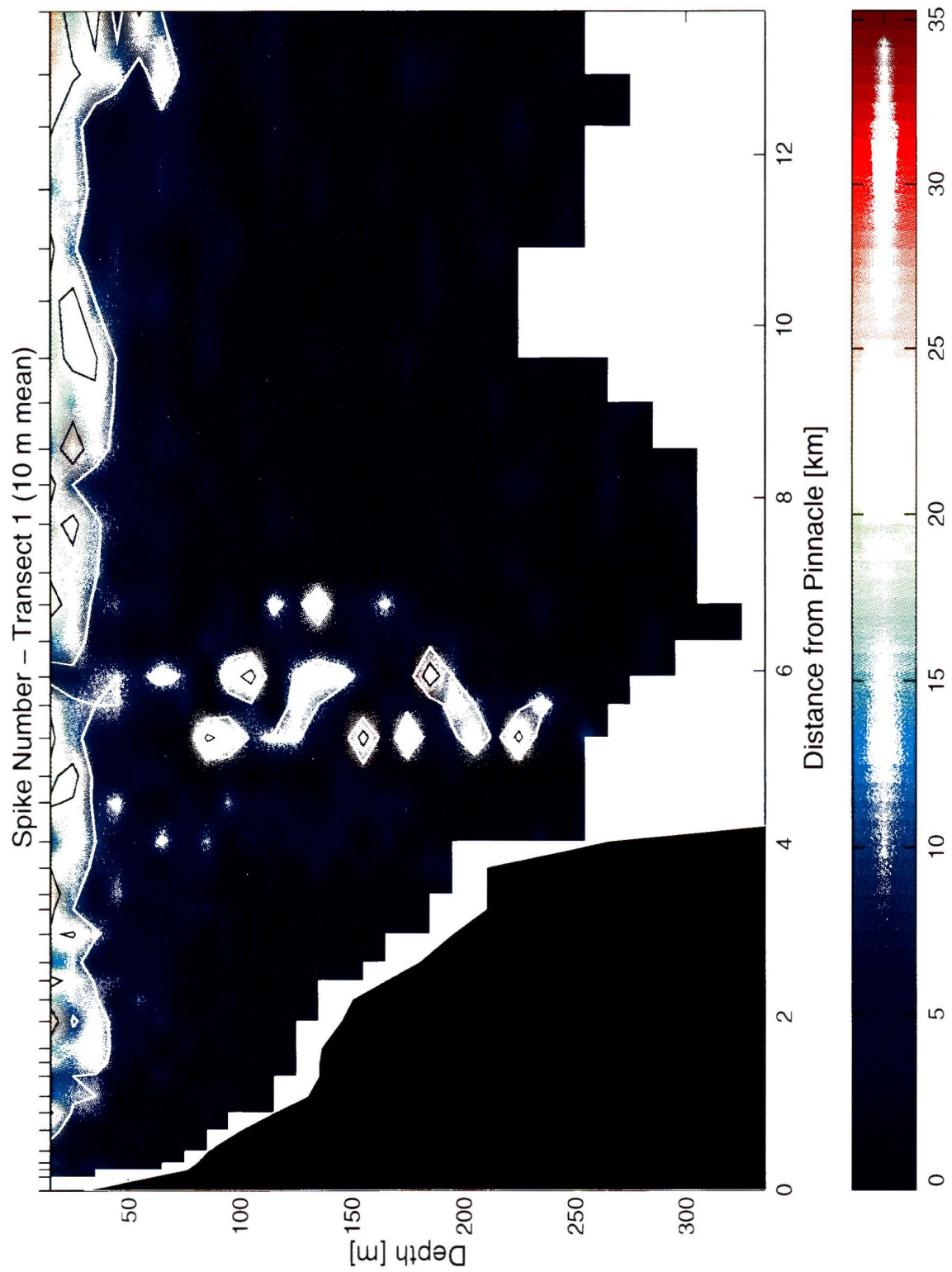


Figure 8.49: Spike profiles for the first transect. Contours from 5 to 20 spikes, at intervals of 5 spikes have been plotted.

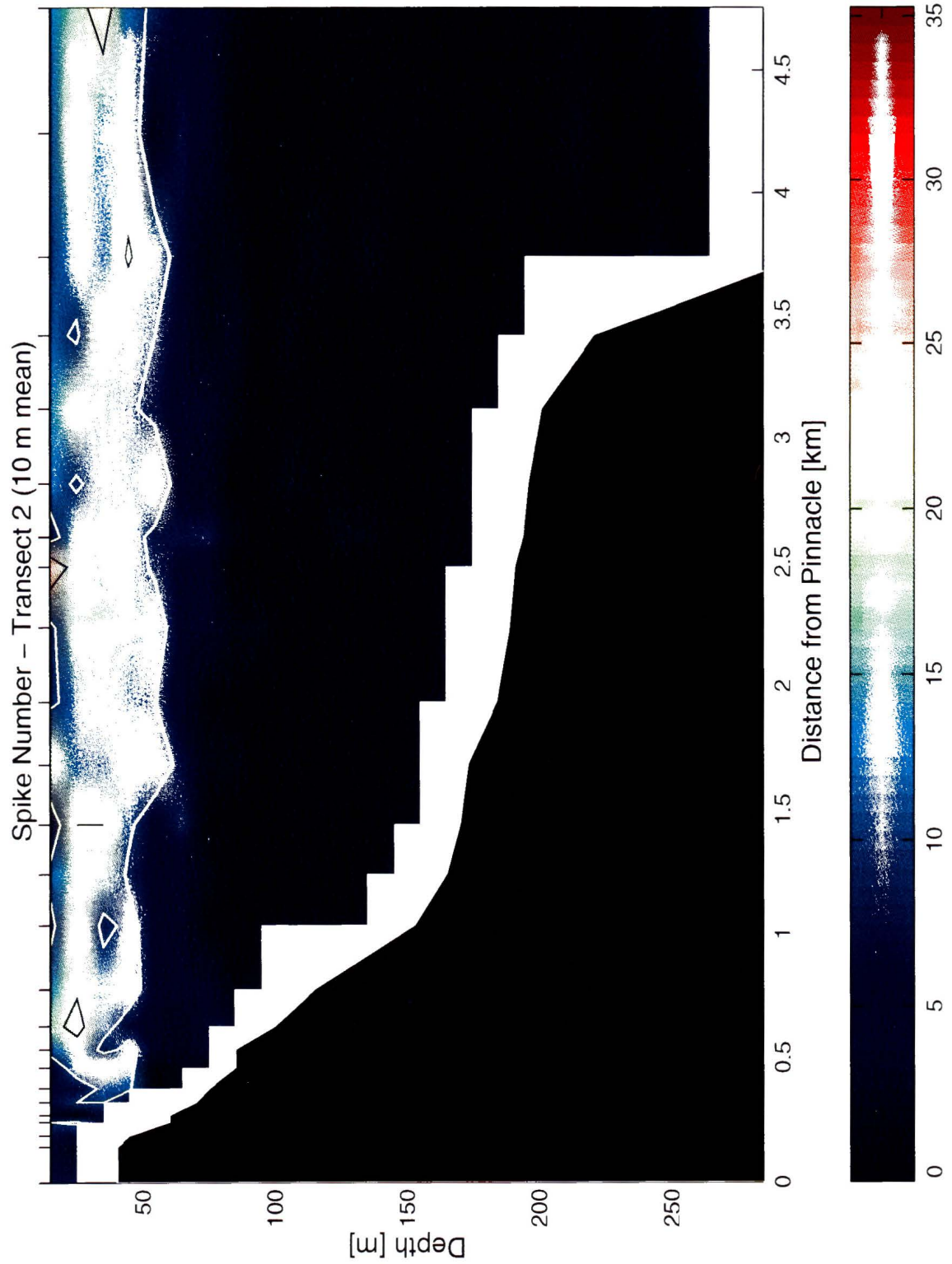


Figure 8.50: Spike profiles for the second transect. Contours from 5 to 25 spikes, at intervals of 5 spikes have been plotted.

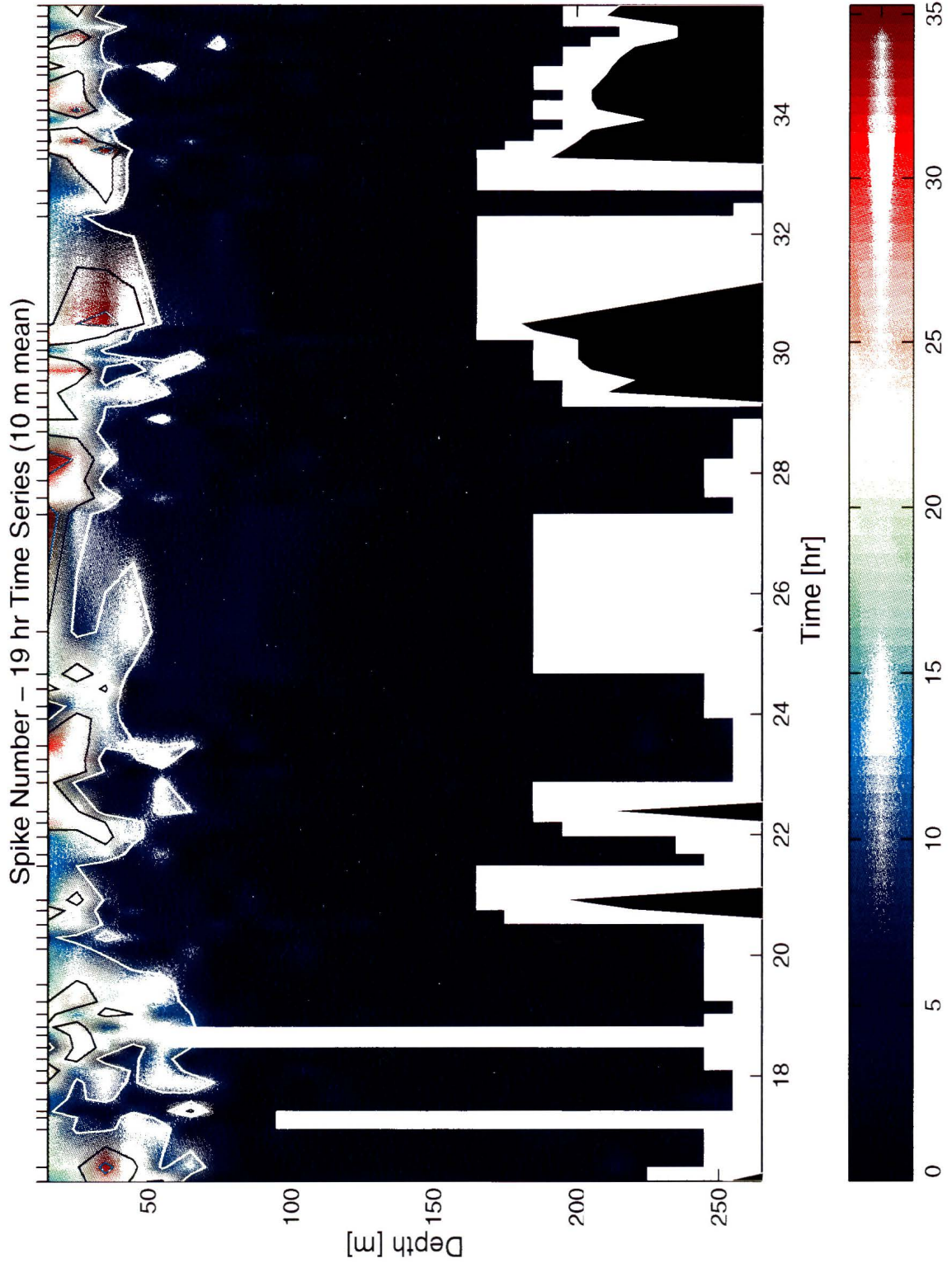


Figure 8.51: Spike profiles for the 19 hour time series. Contours from 5 to 30 spikes, at intervals of 5 spikes have been plotted.

migrators can not be the source of the spikes. An organism, such as a zooplankton, may be able to sense the probe's approach and swim out of the way; however Dower (*pers. comm.*) indicates that most of the larger zooplankton in the subarctic Pacific are not diel migrators. Most of the zooplankton are confined to the upper 80–100 m of the water column, which leaves them as candidates for some of the probe hits.

8.2 Source of Spikes

I have made an order of magnitude estimate for the force detected by the shear probe during the production of a spike in order to determine the minimum size of a particle. The total cross force applied to the shear probe by a turbulent velocity field (Osborn and Crawford 1980) is

$$F_u = \rho_0 A W u, \quad (8.82)$$

where ρ_0 is the water density, A is the cross sectional area of the probe, W is the fall speed and u is the fluctuating component of the cross stream flow. This force can be compared to the force of the probe hitting a particle

$$F_p = \rho_0 V_o \partial u_p / \partial t, \quad (8.83)$$

where V_o is the volume of a particle, which is assumed to have the same density as the water ρ_0 surrounding it, u_p is the cross stream particle velocity and t is time. The approximate acceleration of a particle because of a hit is W over the time T that the particle is in contact with the probe. The time can be estimated either by the observed time for each spike, $T \approx 10$ samples ≈ 0.036 s, or by the amount of time the particle takes to advect past the probe. $T \approx 1$ cm / 50 cm s⁻¹ ≈ 0.020 s. Hence, we can rewrite (8.83) as $F_p = \rho_0 V_o W / T$. and if we equate the particle force and the turbulent flow force then

$$A u = V_o / T. \quad (8.84)$$

The highest resolution attained for u with the FLY II during the cruise was $\approx 0.1 \text{ mm s}^{-1}$, which is similar to the results of Fleury and Lueck (1994). The diameter of the shear probe is 5 mm and a cross sectional area of 20 mm^2 . For the impact time I take the lower value of 0.02 s. Therefore, the smallest particle resolvable by the shear probe has a volume $V_o = 0.04 \text{ mm}^3$ and a length scale of $L = V_o^{1/3} = 0.3 \text{ mm}$. Hence, the sensor may just barely detect hits of the largest microplankton (20–200 μm) but should be able to easily resolve hits with macro- (200–2000 μm) and megaplankton ($> 2000 \mu\text{m}$) (Parsons and Takahashi 1973). The shear signal that would be attained by collisions with the particles that are $L = 2000 \mu\text{m}$ is

$$\frac{\partial u}{\partial z} \approx \frac{V_o}{T^2 AW} \approx 2 \text{ s}^{-1}. \quad (8.85)$$

The maximum shear resolvable as set by the A/D converter is about 20 s^{-1} . This value could be attained for any particles larger than 5 mm, the diameter of the shear probe.

The fall speed of FLY II allows us to make the frozen-turbulence approximation ($u \ll W$); therefore the fact that the particles are in a turbulent velocity field should have no effect on the encounter rate of particles with the probe. In every 10 m of the water column the probe will profile through $20 \times 10^{-6} \text{ m}^2 \cdot 10 \text{ m} = 2 \times 10^{-4} \text{ m}^3$ of water. The diameter of the particle increases the volume of water within which particles can be detected. If the particles that are hit are small ($L \ll 5 \text{ mm}$) then the volume of water within which they are detected is $2 \times 10^{-4} \text{ m}^3$. If the particles are large ($L \geq 5 \text{ mm}$) then the volume becomes significantly larger, four times for particles with $L = 5 \text{ mm}$. This implies that for each particle hit in every 10 m bin the particle density is 1000–5000 particles m^{-3} . The maximum number of particle hits we observed was > 30 which implies a particle concentration $> 30\text{--}150 \times 10^3$ particles m^{-3} . The average particle numbers near the surface was ≈ 15 which implies a particle concentration $15\text{--}75 \times 10^3$ particles m^{-3} . Below 100 m the particle concentration detected was only $1\text{--}5 \times 10^3$ particles m^{-3} .

8.3 Discussion

The actual source of these particles is still uncertain. The probe does not exclusively hit marine snow (marine aggregate), which has concentrations of $1-4 \times 10^3$ particles m^{-3} , but does not have a large enough concentration gradient to explain the large gradient in spikes near the surface (Vernon *et al.* 1992). It is Bishop's (*pers. comm.*) opinion that the particles are biological in origin but may be either live zooplankton or dead material. Certain poor-swimming zooplankton concentrations and fecal material concentrations have large gradients (Bishop *et al.* 1987) that may explain the gradient in numbers of spikes.

Though the results are interesting there are still some points of concern. In Fig. 8.47 there are two different error estimates plotted on the diagrams; the sample standard deviation and the standard deviation due to counting, assuming the spikes follow a Poisson distribution. The average number of spikes identified in each bin is small (< 15), causing the counting errors to be quite large. This can obscure spatial and temporal trends. This is especially true for the CTD time series where all of the variance in the measurements can be explained by counting errors. For the other three series, the variance in measurements near the surface is larger than what can be explained by counting errors alone; therefore the horizontal and temporal trends I identified above 100 m are believable but below 100 m it may be impossible to distinguish any trends, such as those of diel migrators. In some profiles off the rim in transect 1 the spiking is contaminated by other anomalous signals, probably caused by something attaching to the instrument. My estimates of particles sizes are biased by the approximation that the change in cross stream particle velocity is W . Many particles may only make glancing blows on the probe, especially the smallest particles which will move with the potential flow field around the probe. This may reduce the cross stream particle velocity to a small fraction of W . If this technique of measuring particle concentrations is to become practical it must still be calibrated with other

accepted techniques.

Chapter 9

Thorpe Scales

The high resolution temperature was initially designed to produce Thorpe scaling from the data taken at Cobb. The results have not proven to be completely satisfying. The Thorpe scaling indicates that temperature inversions coincide with the turbulent mixing we observed. However, acquiring equivalent values of vertical diffusivity proved difficult. Some of the profiles, especially in the far field of transect 1, went through intrusions. The assumption that there is a monotonic correspondence between temperature and density is therefore invalid and Thorpe scaling cannot be completed with a temperature record.

Much of the difficulty in comparing the Thorpe (l_T) and Ozmidov (l_0) scales derives from the averaging that is done. This is especially important when dealing with the Ozmidov scale, where the value derived from averaging the dissipation rate ϵ and buoyancy frequency N separately or averaging ϵ/N^3 can be very different. Various averaging lengths can produce dramatic differences in the results. This is especially important in determining N because l_0 is more sensitive to changes in N than ϵ . Garrett (*pers. comm.*) has suggested that it may be best to average ϵ , N and the Thorpe displacement separately over most of the water column. Another approach has been to use the maximum Thorpe displacement (Gibson *et al.* 1993) but Dillon (1982) argues that the three dimensional nature of oceanic turbulence makes the rms l_T the more statistically stable value. I believe the best approach (to taking averages) is Dillon's, which is long enough to include all of a distinct disturbance yet short enough that the conditions do not change greatly. As I indicated earlier, the rms of the Thorpe displacement determined over a complete disturbance is invariant

of the reference frame in which the Thorpe displacement is determined. This is not true where the rms is taken over only part of a disturbance. Ideally, for each distinct disturbance an average ϵ , an average N and an rms l_T should be determined. A fixed length running average will be generally inappropriate.

To determine the buoyancy frequency over a disturbance, N must be calculated with the sorted profile, as was done by Crawford (1986). Unfortunately, this requires that density and salinity are simple functions of temperature. This approach is mandatory where the sorted N differs greatly from within to outside of the disturbance. If instead N varies little then an N determined from the unsorted profile by a running average that is larger than the maximum Thorpe displacement may be adequate. Given the insensitivity of l_0 to ϵ , a running average of fixed length can produce reasonable results for a slowly varying ϵ .

My calculations of the Ozmidov and Thorpe scales are heavily averaged and all of the averages are over a fixed length. In determining the buoyancy frequency, the temperature T and salinity S signals are smoothed to remove all fluctuations that occurred on scales less than 15 m. The buoyancy frequency can not be determined from the sorted profile because density and salinity are not simple functions of temperature. Instead, N^2 is calculated using the unsorted profile. The Ozmidov scale is then

$$l_0 = \left(\frac{\bar{\epsilon}}{N^2^{3/2}} \right)^{1/2}, \quad (9.86)$$

where the overbar implies a 15 m running average and ϵ is determined by the spectral method. The values of l_0 and l_T that are presented are rms's taken with a 15 m running averages.

The first example is a profile with no intrusions (Fig. 9.52). The maximum Thorpe displacements are less than 10 m; hence the 15 m running averages are probably appropriate, assuming the properties vary slowly. For the bottom diagram the regression curve was taken for $l_0 = al_T^n$. For this profile $n = 1.049$ and $a = 0.895$ and thus

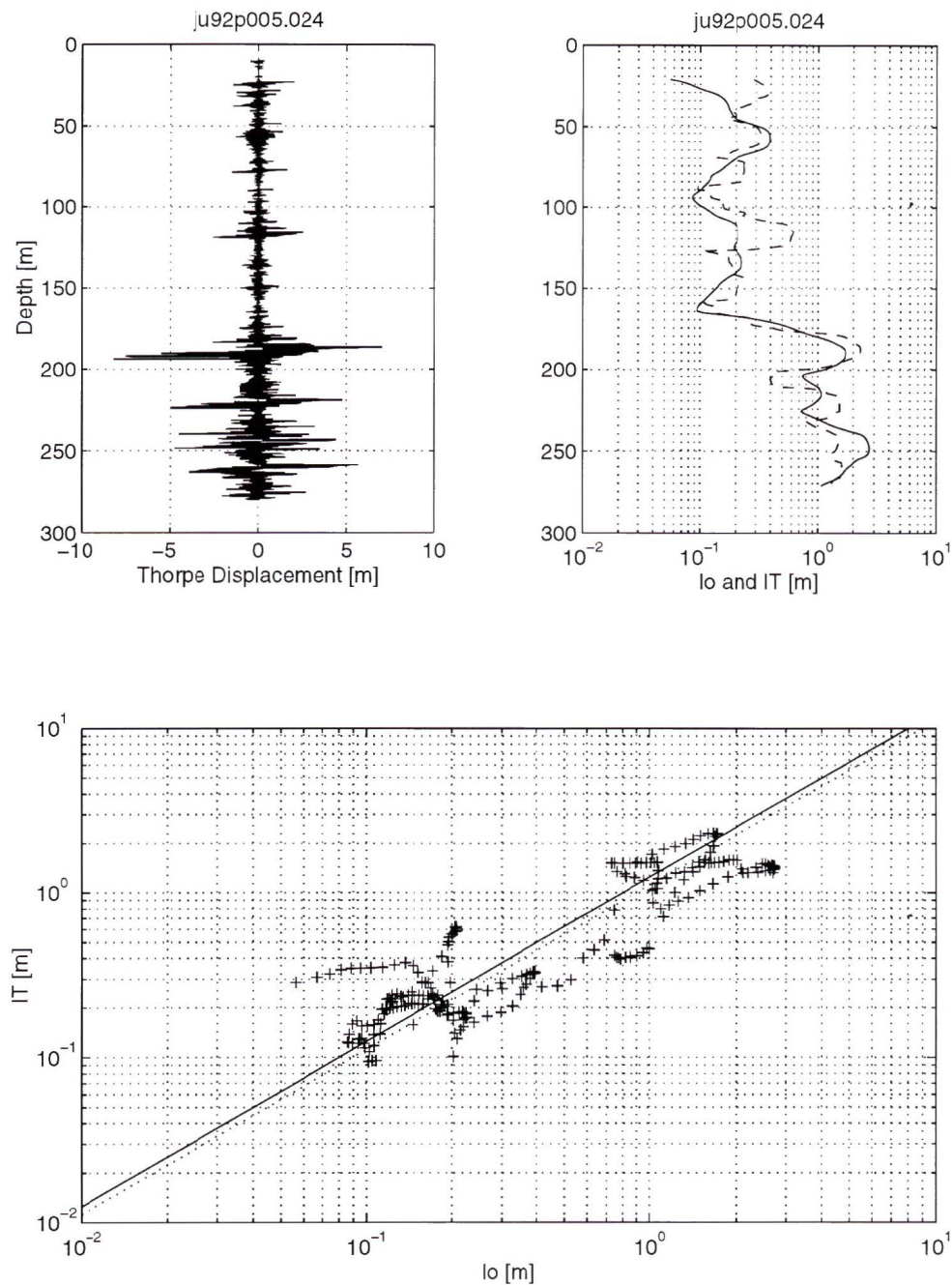


Figure 9.52: A profile near the rim of the seamount during the first transect. The top-left diagram is a profile of the Thorpe displacement. The top-right diagram contains profiles of the Ozmidov scale (solid line) and Thorpe scale (dashed line). The bottom diagram is the Thorpe scale against the Ozmidov scale. There are two diagonal lines, the solid line is for $l_0 = 0.8l_T$ and the dotted line is for $l_0 = 0.89l_T$.

a good approximation is $l_0 = 0.90l_T$. The results match closely with those of Dillon (1982), who determined $a = 0.8$. The good relationship between l_0 and l_T shows that the turbulent kinetic energy of the water column is related to the available potential energy in an averaged sense. This implies that the Thorpe scale can be used to estimate heavily averaged values of ϵ and K_v for this profile. This also implies that N and ϵ are slowly varying, making averages over distinct disturbances unnecessary. Unfortunately, this is not representative of all profiles, many show badly underestimated l_0 for small (< 5 m) disturbances. This is probably the result of overestimated values of N within the disturbances.

In the second example of Thorpe scaling there is no monotonic correspondence between temperature and density (Fig. 9.53). Below 200 m there are a series of intrusions, regions unstable in temperature yet stable in density. The result is anomalously large Thorpe displacements and scales, resulting in a meaningless fit between l_0 and l_T . Most of the far field profiles of the first transect and some profiles near and over the seamount were biased by the presence of intrusions.

The Thorpe scales calculated for profiles around Cobb indicate that regions of high dissipation rates are related to changes in the density structure, a clear indication of mixing. Some of the Thorpe displacement profiles contain distinct disturbances with the classic z -type overturn. These large disturbances (> 10 m) were probably billows generated by internal wave breaking. However, the presence of intrusions requires great care be taken in relating Thorpe scales to turbulent mixing. Even the removal of the intrusions from the data sets would produce biased results because some of the intrusions were present in turbulent water near the seamount. Due to the significant effort required to evaluate unbiased Thorpe scales, to apply flexible averaging as discussed by Dillon (1982) and the marginal benefit of doing so, I have not explored Thorpe scaling further.

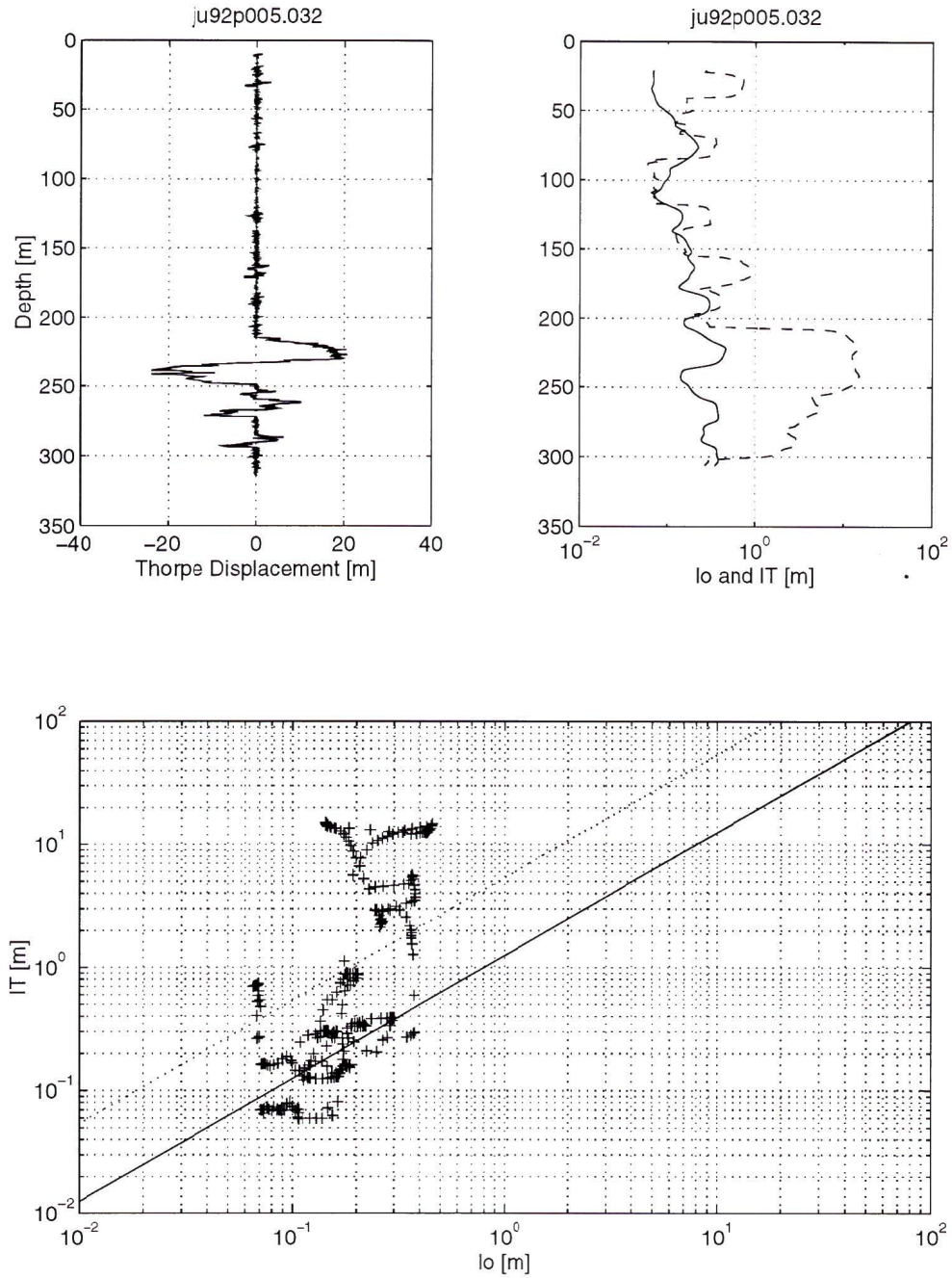


Figure 9.53: A profile in the far-field during the first transect. The top-left diagram is a profile of the Thorpe displacement. The top-right diagram contains profiles of the Ozmidov scale (solid line) and Thorpe scale (dashed line). The bottom diagram is the Thorpe scale against the Ozmidov scale. There are two diagonal lines, the solid line is for $l_0 = 0.8l_T$ and the dotted line is for $l_0 = 0.19l_T$.

Chapter 10

Conclusions

In this thesis I set out to study the interactions of physical processes in the ocean around Cobb Seamount. Some of the observations may be characteristic only of Cobb but I believe many are applicable to all seamounts and perhaps other topographical features.

Chapter 5: Transects

- No doming of isopycnals was found over the seamount because of internal waves. Ensemble averages of profiles taken over a period greater than 12.5 hours would be necessary to resolve any doming. I am unaware of any any data sets that satisfactorily address this problem, which leaves doming unvarified.
- Internal waves are the primary source of turbulence and turbulent mixing around the seamount. Eriksen (1985) cited observational evidence that internal waves generate turbulence 100's of meters from their source. My observations show enhanced turbulence generated by internal waves at least 4000 m and maybe as much as 8000 m away from the source of the waves.
- The largest turbulent mixing around Cobb was the result of internal waves originating from the rim. These are most likely semi-diurnal, internal tides generated and/or reflected at the seamount.
- Mixing around the seamount is equivalent to mixing in 10,000–100,000 km² of the open ocean over the depths 150–350 m. If all seamounts were as efficient as Cobb then they would perform 1–10 times more mixing than the open

ocean's interior. Most of this mixing would occur in the deep ocean because few seamounts are as shallow as Cobb.

Chapter 6: Time Series

- Isopycnal motions show the presence of energetic internal waves of various frequencies around the seamount.
- Most of the enhanced dissipation is separated from the bottom and is driven by internal waves.
- An enhanced dissipation and diffusivity layer was found off the east rim. Hence, mixing by internal tides originating from the rim is not unique to transect 1.
- Enhancement of turbulence is persistent, with only an order of magnitude variation in dissipation rates and vertical diffusivities over 19 hours.

Chapter 7: Bottom Boundary Layer Observations

- The bottom boundary layer structure is periodically dominated by both tidal currents and internal waves. The mean flow is insignificant in determining the bbl conditions.
- The bbl has many different structures which can vary rapidly in time (< 1 hour) and space (< 1 km). Non-log layer like structures are common and may be the result of strong stratification, internal waves and form-drag with large (> 1 m) bottom objects (boulders and basalt columns).
- Not all turbulence in the bbl is driven by shear at the bottom. Some is the result of internal wave breaking or shear within or just above the bottom mixed layer.
- Intermittent mixing at the bottom is more efficient than open ocean mixing but the volume of water in the bbl is small. The bbl mixing may only be equivalent

to what occurs in 1000 km² of the open ocean. This is considerably less than the mixing generated around the seamount by internal waves.

Chapter 8: Counting Spikes

- Shear probe signals are contaminated by hits from particles that are on the order of 0.3 mm or greater in diameter. The largest particles commonly hit are probably greater than 5 mm wide.
- The particles are primarily biological in origin but whether they are mostly living or dead is uncertain.
- Mean relative and absolute particulate densities can be approximated with the spikes in shear probe signals. The absolute particulate densities have yet to be calibrated properly.

Chapter 9: Thorpe Scales

- There are large Thorpe scales within regions of high dissipation near the seamount. This clearly indicates that enhanced dissipation is related to changes in the density structure and mixing.
- Though fixed length averages were adequate for some profiles, averaging over distinct disturbances would have probably produced better results. Unfortunately, determining N^2 for the sorted profile proved impossible.

There are a few very significant conclusions as a result of observations made at Cobb Seamount. The existence of isopycnal doming over Cobb has yet to be convincingly proved. This brings into question many of the conclusions on flow field and biological production that depend on the existence of a Taylor cap. The role of internal waves and rough bottom topography may have to be considered in bottom boundary layer models, which have generally dealt only with mean currents and

smooth bottoms, in order to simulate the bbl features we observed. While bottom mixing appear more efficient than predicted, it is insignificant on a large scale. The near boundary mixing by internal waves, primarily internal tides, dominates all other mixing at the seamount, including bottom mixing, which is ten times smaller. Even though my estimate for mixing in the world's oceans by seamounts has a large degree of statistical uncertainty for many reasons, it does indicate that mixing near boundaries, in particular seamounts, is not insignificant. Further observations and process studies of internal wave generation and reflection from boundaries are still needed.

Bibliography

- [1] Armi, L., 1978: Some evidence of boundary mixing in the deep ocean. *J. Geophys. Res.*, **83**, 1971–1979.
- [2] Baines, P. G., 1974: The generation of internal tides over steep continental slopes. *Phil. Trans. Royal Soc. Lond.*, **a277**, 27–58.
- [3] Baines, P. G., 1982: On internal tide generation models. *Deep-Sea Res.*, **29**, 307–338.
- [4] Bishop, J. K. B., 1986: The correction and suspended particulate matter calibration of Sea Tech transmissometer data. *Deep-Sea Res.*, **33**, 121–134.
- [5] Bishop, J. K. B., J. C. Stepien, and P. H. Wiebe, 1987: Particulate matter distributions, chemistry and flux in the Panama basin: Response to Environmental Forcing. *Prog. Oceanogr.*, **17**, 1–59.
- [6] Boyer, D. L., and X. Zhang, 1990: Motion of oscillatory currents past isolated topography. *J. Phys. Oceanogr.*, **20**, 1425–1448.
- [7] Chapman, D. C., and D. B. Haidvogel, 1992: Formation of Taylor caps over a tall isolated seamount in a stratified ocean. *Geophys. Astrophys. Fluid Dynamics*, **64**, 31–65.
- [8] Chriss, T. M., and D. R. Caldwell. 1982: Evidence for the influence of form drag on bottom boundary layer flow. *J. Geophys. Res.*, **87**, 4148–4154.
- [9] Crawford, W. R., 1986: A comparison of length scales and decay times of turbulence in stably stratified flows. *J. Phys. Oceanogr.*, **16**, 1847–1854.

- [10] Davies, P. A., 1972: Experiments on Taylor columns in rotating stratified fluids. *J. Fluid Mech.*, **54**, 691–717.
- [11] Davies, P. A., R. G. Davis, and M. R. Foster, 1990: Flow past a circular cylinder in a rotating stratified fluid. *Phil. Trans. Royal Soc. Lond.*, **a331**, 245–286.
- [12] Dewey, R. K., 1987: Turbulent energy dissipation over the continental shelf. *Ph. D. Thesis*, University of British Columbia, 206 pp.
- [13] Dewey, R. K., W. R. Crawford, A. E. Gargett, and N. S. Oakey, 1987: A microstructure instrument for profiling oceanic turbulence in coastal bottom boundary layers. *J. Atmos. Oceanic. Technol.*, **4**, 288–297.
- [14] Dower, J. K., 1994: Biological consequences of current-topographical interactions at Cobb Seamount. *Ph. D. Thesis*, University of Victoria, 229 pp.
- [15] Dower, J., H. Freeland, and K. Juniper, 1992: A strong biological response to oceanic flow past Cobb Seamount. *Deep-Sea Res.*, **39**, 1139–1146.
- [16] Dillon, T. R., 1982: Vertical overturns: a comparison of Thorpe and Ozmidov length scales. *J. Geophys. Res.*, **87**, 9601–9613.
- [17] Eriksen, C. C., 1985: Implications of ocean bottom reflection for internal wave spectra and mixing. *J. Phys. Oceanogr.*, **15**, 1145–1156.
- [18] Fleury, M., and R. G. Lueck, 1994: Direct heat flux estimates using a towed vehicle. *J. Phys. Oceanogr.*, **24**, 801–818.
- [19] Freeland, H. J., (1994): Ocean circulation at and near Cobb Seamount. *Deep-Sea Res.*, *submitted*.
- [20] Garrett, C., 1979: Comment on 'some evidence for boundary mixing in the deep ocean' by Laurence Armi. *J. Geophys. Res.*, **84**, 5095–5098.

- [21] Garrett, C., 1991: Marginal mixing theories. *Atmos.-Ocean*, **29**, 313–339.
- [22] Garrett, C., P. MacCready, and P. Rhines, 1993: Boundary mixing and arrested Ekman layers: rotating stratified flow near a sloping boundary. *Annu. Rev. Fluid. Mech.*, **25**, 291–323.
- [23] Gargett, A. E., 1988: A large eddy approach to acoustic remote sensing of turbulent kinetic energy dissipation. *Atmos.-Ocean*, **26**, 483–508.
- [24] Gibson, C. H., V. Nabatov, and R. Ozmidov, 1993: Measurements of turbulence and fossil turbulence near Ampere Seamount. *Dyn. Atmos. Oceans*, **19**, 175–204.
- [25] Gilbert, D., and C. Garrett, 1989: Implications for ocean mixing of internal wave scattering off irregular topography. *J. Phys. Oceanogr.*, **19**, 1716–1729.
- [26] Grant, H. L., R. W. Stewart, and A. Moilliet, 1962: Turbulence spectra from a tidal channel. *J. Fluid Mech.*, **12**, 241–268.
- [27] Grant, H. L., A. Moilliet, and V. M. Vogel, 1968: Some observations of turbulence in and above the thermocline. *J. Fluid Mech.*, **34**, 443–448.
- [28] Gregg, M. C., 1987: Diapycnal mixing in the thermocline. *J. Geophys. Res.*, **93**, 5249–5286.
- [29] Gregg, M. C., C. S. Cox, and P. W. Hacker, 1973: Vertical microstructure measurements in the central north Pacific. *J. Phys. Oceanogr.*, **3**, 458–469.
- [30] Kundu, P. K., 1990: *Fluid Mechanics*, Academic Press, Inc., 638 pp.
- [31] Ledwell, J. R., A. J. Watson, and C. S. Law, 1993: Evidence for slow mixing across an open-ocean tracer-release experiment. *Nature*, **364**, 701–703.
- [32] Lewis, E. L., and R. G. Perkin, 1981: The practical salinity scale 1978: conversion of existing data. *Deep-Sea Res.*, **28A**, 307–328.

- [33] Lueck, R. G., 1990: Thermal inertia of conductivity cells: theory. *J. Atmos. Oceanic. Technol.*, **7**, 741–755.
- [34] Lueck, R. G., W. R. Crawford, and T. R. Osborn, 1983: Turbulent dissipation over the continental slope off Vancouver Island. *J. Phys. Oceanogr.*, **13**, 1809–1818.
- [35] Lueck, R. G., J. J. Picklo, 1990: Thermal inertia of conductivity cells: observations with a Sea-Bird cell. *J. Atmos. Oceanic. Technol.*, **7**, 756–768.
- [36] Lueck, R., and R. Reid, 1984: On the production and dissipation of mechanical energy in the ocean. *J. Geophys. Res.*, **89**, 3439–3445.
- [37] McDougall, T. J., 1989: Dineutral advection. *Proc. 'Aha Huliko'a Hawaiian Winter Workshop, 5th*, pp. 289–315. Honolulu: Hawaii Inst. Geophys.
- [38] Morison, J., R. Andersen, N. Larson, E. D'Asaro, and T. Boyd, 1994: The correction for thermal-lag effects in Sea-Bird CTD data. *J. Atmos. Oceanic. Technol.*, **11**, 1151–1164.
- [39] Mudge, T. D., and R. G. Lueck, 1994: Digital signal processing to enhance oceanographic observations. *J. Atmos. Oceanic. Technol.*, **11**, 827–836.
- [40] Munk, W. H., 1966: Abyssal recipes. *Deep-Sea Res.*, **13**, 707–730.
- [41] Munk, W. H., 1981: Internal waves and small scale processes. *Evolution of Physical Oceanography Scientific Surveys in Honor of Henry Stommel*, B. A. Warren and C. Wunsch, Eds., MIT Press, 264–291.
- [42] Nabatov, V. N., and R. V. Ozmidov. 1988: Study of turbulence above seamounts in the Atlantic Ocean. *Oceanology*, **28**, 161–166.
- [43] Nasmyth, P. W., 1970: Oceanic turbulence. *Ph. D. Thesis*, University of British Columbia, 69 pp.

- [44] Ninnis, R., 1984: The effects of spatial averaging on airfoil probe measurements of oceanic velocity microstructure. *Ph. D. Thesis*, University of British Columbia, 109 pp.
- [45] Oakey, N. S., 1982: Determination of the rate of dissipation of turbulence energy from simultaneous temperature and velocity shear microstructure. *J. Phys. Oceanogr.*, **12**, 256–271.
- [46] Oakey, N. S., and J. A. Elliott, 1982: Dissipation within the surface mixed layer. *J. Phys. Oceanogr.*, **12**, 171–185.
- [47] Osborn, T. R., 1974: Vertical profiling of velocity microstructure. *J. Phys. Oceanogr.*, **4**, 109–115.
- [48] Osborn, T. R., 1978: Measurements of energy dissipation adjacent to an island. *J. Geophys. Res.*, **83**, 2939–2957.
- [49] Osborn, T. R., 1980: Estimates of the local rate of vertical diffusion from dissipation measurements. *J. Phys. Oceanogr.*, **10**, 83–89.
- [50] Osborn, T. R., and C. S. Cox, 1972: Oceanic fine-structure. *Geophys. Fluid Dyn.*, **3**, 321–345.
- [51] Osborn, T. R., and W. R. Crawford, 1980: An airfoil probe for measuring turbulent velocity fluctuation in water. *Air-Sea Interaction: Instruments and Methods*, F. Dobson, L. Hase, and R. Davis, Eds., Plenum.
- [52] Osborn, T. R., and R. G. Lueck, 1985a: Turbulence measurements from a towed body. *J. Atmos. Oceanic. Technol.* **2**, 517–527.
- [53] Osborn, T. R., and R. G. Lueck, 1985b: Turbulence measurements with a submarine. *J. Phys. Oceanogr.*, **15**, 1503–1520.

- [54] Owens, W. B., and N. G. Hogg, 1980: Oceanic observations of stratified Taylor columns near a bump. *Deep-Sea Res.*, **27**, 1029–1045.
- [55] Parsons, T., and M. Takahashi, 1973: *Biological Oceanographic Processes*, Peragon Press Ltd., 186 pp.
- [56] Phillips, O. M., J. H. Shyu, and H. Salmun, 1986: An experiment on boundary mixing: mean circulation and transport rates. *J. Fluid Mech.*, **173**, 473–499.
- [57] Polzin K., J. Toole, and R. Schmitt, 1994: Finescale parameterizations of turbulent dissipation. *J. Phys. Oceanogr.*, *submitted*.
- [58] Price J. F., M. O’Neil Baringer, R. G. Lueck, G. C. Johnson, I. Ambar, G. Parrilla, A. Cantos, M. A. Kennelly, and T. B. Sanford, 1993: Mediterranean outflow mixing dynamics. *Science*, **259**, 1277–1282.
- [59] Roden, G. I., 1984: Mesoscale sound speed fronts in the central and western north Pacific and in the Emperor Seamounts region. *J. Phys. Oceanogr.*, **14**, 1659–1669.
- [60] Roden, G. I., and B. A. Taft, 1985: Effect of the Emperor Seamounts on the mesoscale thermohaline structure during the summer of 1982. *J. Geophys. Res.*, **90**, 839–855.
- [61] Schmitt, R. W., K. L. Polzin, and J. M. Toole, 1994: A comparison of direct turbulence measurements with tracer dispersion in the north Atlantic tracer release experiment. *1994 Ocean Sciences Meeting*, AGU.
- [62] Sjöberg, B., and A. Stigebrandt, 1992. Computations of the geographical distribution of the energy flux to mixing processes via internal tides and associated vertical circulation in the ocean. *Deep-Sea Res.*, **39**, 269–291.
- [63] Smith, W. O., and T. H. Jordan, 1988: Seamount statistics in the Pacific Ocean. *J. Geophys. Res.*, **93**, 2899–2919.

- [64] Stommel, H., and A. B. Arons, 1960: On the abyssal circulation of the world ocean. I. Stationary planetary flow patterns on a sphere. *Deep-Sea Res.*, **6**, 140–154.
- [65] Tennekes, H., and J. L. Lumley, 1972: *A First Course in Turbulence*, MIT Press, 300 pp.
- [66] Thorpe, S. A., 1977: Turbulence and mixing in a Scottish Loch. *Phil. Trans. Royal Soc. Lond.*, **a286**, 125–181.
- [67] Trowbridge, J. H., and S. J. Lentz, 1991: Asymmetric behavior of an oceanic boundary layer above a sloping bottom. *J. Phys. Oceanogr.*, **21**, 1171–1185.
- [68] Vernon, L. A., S. Honjo, and T. H. Orsi, 1992: Distribution and transport of marine snow aggregates in the Panama Basin. *Deep-Sea Res.*, **39**, 939–952.
- [69] Weatherly, G. L., and P. J. Martin, 1978: On the structure and dynamics of the oceanic bottom boundary layer. *J. Phys. Oceanogr.*, **8**, 557–570.
- [70] Yamazaki, H., 1990: Stratified turbulence near a critical dissipation rate. *J. Phys. Oceanogr.*, **20**, 1583–1598.
- [71] Yamazaki, H., and R. Lueck, 1990: Why oceanic dissipation rates are not log-normal. *J. Phys. Oceanogr.*, **20**, 1907–1918.
- [72] Zhang, X., and D. L. Boyer, 1993: Laboratory study of rotating, stratified oscillatory flow over a seamount. *J. Phys. Oceanogr.*, **23**, 1122–1141.

VITA

Surname: Mudge
Place of Birth: Labrador City, Nfld.

Given Names: Todd Douglas
Date of Birth: September 25, 1968

Educational Institutes Attended:

B.Sc. (Honours) Memorial University of Newfoundland 1991

Honours and Awards:

Graduate Teaching Fellowship	UVic	1991–94
Atlantic Accord Career Development Award (Graduate Fellowship)	UVic	1992
Bronze Convocation Medal for Physics	MUN	1991
Undergraduate Natural Sciences and Engineering Research Council Fellowship	UVic	1990–91
Atlantic Accord Career Development Award (Undergraduate Fellowship)	MUN	1989
SW Breckon Scholarship	MUN	1989–91
Robert G. Reid Scholarship	MUN	1990
Centenary of Responsible Government Award	MUN	1987 & 1989
Principal's Scholarship	MUN	1988
Corner Brook Pulp and Paper Limited Prize for Excellence in Physics	MUN	1986–87
Provincial Electoral Scholarship	MUN	1986

Publications:

Mudge, T. D., and R. G. Lueck, 1994: Digital Signal Processing to Enhance Oceanographic Observations. *J. Atmos. Oceanic. Technol.*, **11**, 827–836.

Gemmerich, J. R., T. D. Mudge, and V. D. Polonichko, 1994: On the Energy Input from Wind to Surface Waves. *J. Phys. Oceanogr.*, **24**, 2413–2417.

PARTIAL COPYRIGHT LICENSE

I hereby grant the right to lend my thesis to users of the University of Victoria Library, and to make single copies only for such users in response to a request from the Library of any other university, or similar institution, on its behalf or for one of its users. I further agree that permission for extensive copying of this thesis for scholarly purposes may be granted by me or a member of the University designated by me. It is understood that copying or publication of this thesis for financial gain shall not be allowed without my permission.

Title of Thesis: MIXING AROUND A SHALLOW SEAMOUNT.

Author:



Todd Douglas Mudge

January 11, 1995